

REPORT DOCUMENTATION PAGE			Form Approved OMB NO. 0704-0188		
<p>The public reporting burden for this collection of information is estimated to average 1 hour per response, including the time for reviewing instructions, searching existing data sources, gathering and maintaining the data needed, and completing and reviewing the collection of information. Send comments regarding this burden estimate or any other aspect of this collection of information, including suggestions for reducing this burden, to Washington Headquarters Services, Directorate for Information Operations and Reports, 1215 Jefferson Davis Highway, Suite 1204, Arlington VA, 22202-4302. Respondents should be aware that notwithstanding any other provision of law, no person shall be subject to any penalty for failing to comply with a collection of information if it does not display a currently valid OMB control number.</p> <p>PLEASE DO NOT RETURN YOUR FORM TO THE ABOVE ADDRESS.</p>					
1. REPORT DATE (DD-MM-YYYY) 21-11-2013		2. REPORT TYPE Final Report		3. DATES COVERED (From - To) 1-Aug-2010 - 31-Jul-2013	
4. TITLE AND SUBTITLE Bio-Inspired Flexible Cellular Actuating Systems			5a. CONTRACT NUMBER W911NF-10-1-0296		
			5b. GRANT NUMBER		
			5c. PROGRAM ELEMENT NUMBER 611102		
6. AUTHORS Soon-Jo Chung, Ashraf Bastawros			5d. PROJECT NUMBER		
			5e. TASK NUMBER		
			5f. WORK UNIT NUMBER		
7. PERFORMING ORGANIZATION NAMES AND ADDRESSES University of Illinois - Urbana c/o OSPRA 1901 S. First Street, Suite A Champaign, IL 61820 -7406			8. PERFORMING ORGANIZATION REPORT NUMBER		
9. SPONSORING/MONITORING AGENCY NAME(S) AND ADDRESS (ES) U.S. Army Research Office P.O. Box 12211 Research Triangle Park, NC 27709-2211			10. SPONSOR/MONITOR'S ACRONYM(S) ARO		
			11. SPONSOR/MONITOR'S REPORT NUMBER(S) 58068-EG.17		
12. DISTRIBUTION AVAILABILITY STATEMENT Approved for Public Release; Distribution Unlimited					
13. SUPPLEMENTARY NOTES The views, opinions and/or findings contained in this report are those of the author(s) and should not be construed as an official Department of the Army position, policy or decision, unless so designated by other documentation.					
14. ABSTRACT The objective of this ARO project is to lay the control-theoretic foundation of controlling a hyper-redundant robotic arm or flexible robotic actuators, often represented by a distributed parameter system or a partial differential equation. We establish a model-guided approach for fabrication and control of flexible 3-D cellular actuator structures based on Electro-Active Polymers (EAPs) or other flexible materials. A model-guided approach for control of flexible structures is epitomized by the PI's PDE boundary control framework applied to articulated structures. The combined theoretical and experimental modeling framework would enable the evaluation and					
15. SUBJECT TERMS control, robotics, flexible structures, control of complex systems, muscle actuators					
16. SECURITY CLASSIFICATION OF:			17. LIMITATION OF ABSTRACT UU	15. NUMBER OF PAGES	19a. NAME OF RESPONSIBLE PERSON Soon-Jo Chung
a. REPORT UU	b. ABSTRACT UU	c. THIS PAGE UU			19b. TELEPHONE NUMBER 217-244-2737

Report Title

Bio-Inspired Flexible Cellular Actuating Systems

ABSTRACT

The objective of this ARO project is to lay the control-theoretic foundation of controlling a hyper-redundant robotic arm or flexible robotic actuators, often represented by a distributed parameter system or a partial differential equation. We establish a model-guided approach for fabrication and control of flexible 3-D cellular actuator structures based on Electro-Active Polymers (EAPs) or other flexible materials. A model-guided approach for control of flexible structures is epitomized by the PI's PDE boundary control framework applied to articulated structures. The combined theoretical and experimental modeling framework would enable the exploitation and optimization of different actuator designs to achieve desirable dynamic and material characteristics. As far as material characterization is concerned, we focused on: (i) multi-physics modeling of EAP under combined electric and mechanical loading and (ii) the role of geometric reinforcement and stiffeners on macroscopic response and force-stroke characteristics of an EAP-based actuator.

Enter List of papers submitted or published that acknowledge ARO support from the start of the project to the date of this printing. List the papers, including journal references, in the following categories:

(a) Papers published in peer-reviewed journals (N/A for none)

Received

Paper

08/31/2012 9.00 A. Paranjape, J. Guan, S.-J. Chung, and M. Krstic. Closed-Loop Perching of Aerial Robots with Articulated Flapping Wings, IEEE Transaction on robotics, (01 2013): 0. doi:

11/21/2013 10.00 Aditya A. Paranjape, Jinyu Guan, Soon-Jo Chung, Miroslav Krstic. PDE Boundary Control for Flexible Articulated Wings on a Robotic Aircraft, IEEE Transactions on Robotics, (06 2013): 625. doi:

TOTAL: 2

Number of Papers published in peer-reviewed journals:

(b) Papers published in non-peer-reviewed journals (N/A for none)

Received

Paper

TOTAL:

Number of Papers published in non peer-reviewed journals:

(c) Presentations

Number of Presentations: 0.00

Non Peer-Reviewed Conference Proceeding publications (other than abstracts):

Received Paper

TOTAL:

Number of Non Peer-Reviewed Conference Proceeding publications (other than abstracts):

Peer-Reviewed Conference Proceeding publications (other than abstracts):

Received Paper

08/30/2011	2.00	Aditya A. Paranjape, Soon-Jo Chung, Miroslav Krstic. PDE Boundary Control for Flexible Articulated Aircraft Wings, Proc. AIAA Guidance, Navigation, and Control Conference. 09-AUG-11, . . . ,
08/31/2012	5.00	William Lai, Ashraf F. Bastawros, Wei Hong, Soon-Jo Chung. Fabrication and Analysis of Planar Dielectric Elastomer Actuators Capable of Complex 3-D Deformation, IEEE International Conference on Robotics and Automation (ICRA). 14-MAY-12, . . . ,
08/31/2012	8.00	A. Paranjape, J. Guan, S.-J. Chung, M. Krstic. PDE Boundary Control for Euler-Bernoulli Beam Using a Two Stage Perturbation Observer, IEEE Conference on Decision and Control . 10-DEC-12, . . . ,
08/31/2012	6.00	William Lai, Ashraf F. Bastawros, Wei Hong. Out-of-Plane Motion of a Planar Dielectric Elastomer Actuator with Distributed Stiffeners, Electroactive Polymer Actuators and Devices (EAPAD) 2012. 12-MAR-12, . . . ,
11/21/2013	14.00	Aditya A. Paranjape, Jinyu Guan, Soon-Jo Chung, Miroslav Krstic. PDE Boundary Control for Euler-Bernoulli Beam Using a Two Stage Perturbation Observer, IEEE Conference on Decision and Control (CDC). 10-DEC-12, . . . ,

TOTAL: 5

Number of Peer-Reviewed Conference Proceeding publications (other than abstracts):

(d) Manuscripts

Received

Paper

08/30/2011 3.00 Soon-Jo Chung, Jean-Jacques Slotine. On Synchronization of Coupled Hopf-Kuramoto Oscillators with Phase Delays,
IEEE Transactions on Automatic Control (to be submitted) (08 2011)

11/21/2013 11.00 Aditya A. Paranjape, Soon-Jo Chung. Dyadic Perturbation Observer Framework for Control of a Class of Nonlinear ODE/PDE Systems,
IEEE Transactions on Automatic Control (08 2013)

11/21/2013 12.00 William Lai, Ashraf Bastawros, Wei Hong, Soon Jo Chung. Planar dielectric elastomer actuator capable of out-of-plane deformation without prestretch,
Soft Matter (01 2014)

11/21/2013 13.00 William Lai, Ashraf Bastawros, Wei Hong, Soon-Jo Chung. Control of force-stroke characteristics of planar dielectric elastomer actuator,
Soft Matter (01 2014)

TOTAL: 4

Number of Manuscripts:

Books

Received

Paper

TOTAL:

Patents Submitted

Patents Awarded

Awards

Soon-Jo Chung: Beckman Fellow of the Center for Advanced Study (CAS), University of Illinois

Soon-Jo Chung: NSF Faculty Early Career Development Award (CAREER), 2013

Soon-Jo Chung: NASA Jet Propulsion Laboratory Summer Faculty Fellow, 2010, 2011, 2013

Soon-Jo Chung: Innovator by Crain's Chicago Business (May 28, 2012)

Soon-Jo Chung: Author of one of the top 1% most highly cited papers in the field worldwide (based on Elsevier Scopus), Council of Canadian Academies (2011)

Soon-Jo Chung: 1st Place in the 2010/2011 AIAA Undergraduate Team Space Design Competition (Faculty Advisor/ Senior Design Instructor) (2011)

Ashraf Bastawros, T.A. Wilson Professor of Aerospace Engineering, Iowa State, 2013

Ashraf Bastawros, International Program Professor 2011/2012, College of Engineering, Iowa State University.

Graduate Students

<u>NAME</u>	<u>PERCENT SUPPORTED</u>	Discipline
Jinyu Guan	1.00	
Nitish Sanghi	0.50	
Michael Dorothy	0.25	
William Lai	1.00	
Aditya Paranjape	0.25	
FTE Equivalent:	3.00	
Total Number:	5	

Names of Post Doctorates

<u>NAME</u>	<u>PERCENT SUPPORTED</u>
Dr. Aditya Paranjape	0.50
FTE Equivalent:	0.50
Total Number:	1

Names of Faculty Supported

<u>NAME</u>	<u>PERCENT SUPPORTED</u>	National Academy Member
Soon-Jo Chung	0.08	
Ashraf Bastawros	0.08	
FTE Equivalent:	0.16	
Total Number:	2	

Names of Under Graduate students supported

<u>NAME</u>	<u>PERCENT SUPPORTED</u>	Discipline
Daniel Park	0.25	Aerospace Engineering
Sarah Weems	0.25	Aerospace Engineering
Drew Warnock	0.13	Aerospace Engineering
FTE Equivalent:	0.63	
Total Number:	3	

Student Metrics

This section only applies to graduating undergraduates supported by this agreement in this reporting period

The number of undergraduates funded by this agreement who graduated during this period: 3.00

The number of undergraduates funded by this agreement who graduated during this period with a degree in science, mathematics, engineering, or technology fields:..... 3.00

The number of undergraduates funded by your agreement who graduated during this period and will continue to pursue a graduate or Ph.D. degree in science, mathematics, engineering, or technology fields:..... 2.00

Number of graduating undergraduates who achieved a 3.5 GPA to 4.0 (4.0 max scale):..... 2.00

Number of graduating undergraduates funded by a DoD funded Center of Excellence grant for Education, Research and Engineering:..... 0.00

The number of undergraduates funded by your agreement who graduated during this period and intend to work for the Department of Defense 0.00

The number of undergraduates funded by your agreement who graduated during this period and will receive scholarships or fellowships for further studies in science, mathematics, engineering or technology fields: 0.00

Names of Personnel receiving masters degrees

NAME

Jinyu Guan

Nitish Sanghi

William Lai

Total Number: 3

Names of personnel receiving PHDs

NAME

Aditya Paranjape

Total Number: 1

Names of other research staff

NAME

Michael McFarland

PERCENT SUPPORTED

0.00

FTE Equivalent: 0.00

Total Number: 1

Sub Contractors (DD882)

Inventions (DD882)

Scientific Progress

See Attachment

Technology Transfer

Final Report - W911NF-10-1-0296
(Reporting Period: 08/01/2010– 07/31/2013)

Bio-Inspired Flexible Cellular Actuating Systems

PI: Prof. Soon-Jo Chung
Department of Aerospace Engineering
University of Illinois, Urbana-Champaign, Urban, IL, 61822
Co-PI: Prof. Ashraf Bastawros
Department of Aerospace Engineering
Iowa State University, Ames, IA, 50010

Table of Contents

1. Statement of the problem studied
2. Summary of the most important results
3. Bibliography
4. Appendixes (4 Journal Papers published, in review, or to be submitted)
 - A. A. Paranjape, J. Guan, S.-J. Chung, and M. Krstic, “PDE Boundary Control for Flexible Articulated Wings on a Robotic Aircraft,” *IEEE Transactions on Robotics*, vol. 29, no. 3, June 2013, pp. 625-640.
 - A. A. Paranjape and S.-J. Chung, “Dyadic Perturbation Observer Framework for Control of a Class of Nonlinear ODE/PDE Systems,” *IEEE Transactions on Automatic Control*, under review, 2013.
 - Lai, W.; Bastawros, A.; Hong, W., Chung, S. 2013, Planar dielectric elastomer actuator capable of out-of-plane deformation without prestretch, (In preparation)
 - Lai, W.; Bastawros, A.; Hong, W., Chung, S. 2013, Control of force-stroke characteristics of planar dielectric elastomer actuator (In preparation)

1. Statement of the problem studied

Objective

The objective of this ARO project is to lay the control-theoretic foundation of controlling a hyper-redundant robotic arm or flexible robotic actuators, often represented by a distributed parameter system or a partial differential equation. We establish a model-guided approach for fabrication and control of flexible 3-D cellular actuator structures based on Electro-Active Polymers (EAPs) or other flexible materials. A model-guided approach for control of flexible structures is epitomized by the PI's PDE boundary control framework applied to articulated structures. The combined theoretical and experimental modeling framework would enable the exploitation and optimization of different actuator designs to achieve desirable dynamic and material characteristics. As far as material characterization is concerned, we focused on: (i) multi-physics modeling of EAP under combined electric and mechanical loading and (ii) the role of geometric reinforcement and stiffeners on macroscopic response and force-stroke characteristics of an EAP-based actuator.

Approach

- Derive a control-theoretic framework of controlling a distributed parameter system (DPS) or partial differential equation (PDE) using the newly proposed PDE boundary control framework of Dyadic Perturbation Observer (DPO) developed by the PI and his research team.
- Apply DPO and compare with the existing PDE control approaches
- Develop a simple, effective experimental validation of the otherwise highly control theoretic approach.
- Devise a numerical framework that enables the optimization and characterization of different actuator configurations
- Verify the material model prediction through different combination of loading.
Examine the role of geometric constraints on the macroscopic response of the proposed actuators, to control the force-stroke characteristics
- Devise a simplified analytical framework to describe the actuator response that can be used with the control algorithms.

Relevance to Army

Compliant robotic actuators provide the ability to interact with dynamically varying external conditions. The realization of the proposed actuation and sensory framework will assist in exploration of forbidden terrains, monitoring of critical assets, as well as mitigation of environmental hazards. The Army's future combat robots equipped with flexible continuum actuators can respond to combat needs in hostile environments, especially when integrated with intelligence, surveillance, reconnaissance (ISR) sensors. Moreover, the proposed work can be further extended to computer-controlled minimally-invasive surgical tools for the Army's field hospitals. Additionally actively-controlled planar actuators are identified as enabling technologies for the broader problem of developing a flexible-winged micro aerial vehicle (MAV) capable of agile flight in constrained environments. At the commercial and civilian application level, we envision a range of system-level applications, including (a) a generalized

3D morphing structure for robotic grippers, (b) flexible robot manipulators without articulated joints for greater maneuverability in highly constrained spaces for endoscopic surgical procedures, (c) artificial muscles for biomimetic locomotion, swimming, and flying, and (d) next-generation robotic manipulators and tethers for autonomous docking in space and tethered spacecraft operations.

2. Summary of the most important results

Detailed, bulleted accomplishments for the period should be traceable back to approach and objectives please be specific and quantitative where possible.

- We have obtained important results on how to synthesize, analyze, and design control of complex flexible structures by PDE boundary control formulations (IEEE Transactions on Robotics full-length paper published in 2013). This result is particularly useful when the PDE model (combined hyperbolic PDEs of torsion and fourth-order bending PDEs) is cross-coupled with the rigid body motion of a platform represented by a highly uncertain nonlinear ODE model.
- We also derived and further developed the newly proposed PDE control framework of Dyadic Perturbation Observer (DPO) and submitted a manuscript to the IEEE Transactions on Automatic Control.
- At the same time, we are making good progress in applying a Central Pattern Generator-based control approach to control and motion planning of a flexible robotic actuator that might not engage in oscillatory motions. Hence, this work is different from PI's prior work that has successfully applied CPG-based control approaches to oscillatory motions like flapping.
- We developed mathematical framework for the electro-mechanical behavior of EAP, combining the Maxwell-stress arising from applied electric field with the non-linear hyper-elastic material response
- We implemented the mathematical framework into a user-material subroutine for ABAQUS commercial finite element software.
- We performed multi-axial tensile testing with different biaxial loading ratio to calibrate the material model
- We performed controlled actuation of pre-stretched actuators to calibrate the electro-mechanical coupling and the FEM model prediction.
- We designed and optimized different actuator configuration capable of multiple-force stroke characteristics
- We utilized segmented electrodes to build free standing planar actuators capable of 3D deformation with prescribed force-stroke characteristics.
- We developed performance map for different geometric stiffeners layout to control the force-stroke characteristics at constant overall actuator stiffness and applied electric field.
- A tenfold increase in the force-stroke characteristics is achieved from changing the stiffeners pitch and periodicity.

- We developed and verified simplified analytical models based on Timoshenko biomaterial-thermostat theory. An experimentally calibrated geometric factor is used to correct for local inhomogeneous deformation.

Collaborations and Technology Transfer

- Invited talk at the Army Research Lab (Host: Dr. Sam Stanton & Harris Edge) on 11/1/2012.
- Discussion with the ARL researchers on the Army MAST program.
- Data sharing with Pratt & Whitney for possible implementation of long slender internal or external gripper
- Data sharing with Boeing St. Lewis for possible utilization of soft actuators

3. Bibliography

Resulting Journal Publications (attached in this report)

- A. A. Paranjape, J. Guan, S.-J. Chung, and M. Krstic, "PDE Boundary Control for Flexible Articulated Wings on a Robotic Aircraft," *IEEE Transactions on Robotics*, vol. 29, no. 3, June 2013, pp. 625-640.
- A. A. Paranjape and S.-J. Chung, "Dyadic Perturbation Observer Framework for Control of a Class of Nonlinear ODE/PDE Systems," *IEEE Transactions on Automatic Control*, under review (submitted 8/2013), 2013.
- Lai, W.; Bastawros, A.; Hong, W., Chung, S. 2013, Planar dielectric elastomer actuator capable of out-of-plane deformation without prestretch, (In preparation)
- Lai, W.; Bastawros, A.; Hong, W., Chung, S. 2013, Control of force-stroke characteristics of planar dielectric elastomer actuator (In preparation)

Resulting Conference Publications

- Paranjape, J. Guan, S.-J. Chung, M. Krstic, "PDE Boundary Control for Euler-Bernoulli Beam Using a Two Stage Perturbation Observer," *IEEE Conference on Decision and Control (CDC)*, Maui, HI, December 2012, pp. 4442-4448.
- A. Paranjape, S.-J. Chung, and M. Krstic, "PDE Boundary Control for Flexible Articulated Aircraft Wings," *AIAA Guidance, Navigation, and Control Conference*, Portland OR, August 2011, AIAA 2011-6486.
- Lai, W.; Bastawros, A.; Hong, W., "Out-of-Plane Motion of a Planar Dielectric Elastomer Actuator with Distributed Stiffeners," *Conference on Electroactive Polymer Actuators and Devices (EAPAD)*, San Diego, CA, MAR 12-15, 2012; *Proceedings of SPIE*, Vol. 8340, Article Number: 834011.
- W. Lai, A. Bastawros, W. Hong, and S.-J. Chung, "Fabrication and Analysis of Planar Dielectric Elastomer Actuators Capable of Complex 3-D Deformation," *IEEE International Conference on Robotics and Automation (ICRA)*, St Paul, MN May 14-18, 2012.

Graduate Students and Thesis Titles

- Jinyu Guan (M.S., graduated in May 2012), Aerospace Engineering, UIUC
M.S. Thesis: Design and Control Strategy of a Flexible, Hyper-Redundant Robotic Arm using Electroactive Dielectric Polymers
- Nitish Sanghi (M.S., graduated in May 2013), Mechanical Engineering, UIUC
M.S. Thesis: Design of Flexible Actuators using Electro-Active Polymers And CPG-based Control Strategies
- Michael Dorothy (Ph.D., Expected December 2014) Aerospace Engineering, UIUC
Ph.D. thesis in progress: Nonlinear Stability of Coupled Oscillators
- Dr. Aditya Paranjape (PhD., graduated in 12/2011 and currently postdoc at UIUC)
Ph.D. Thesis: Dynamics and Control of Robotic Aircraft With Articulated Wings

Dr. Aditya Paranjape, who was partially supported by this ARO grant will become a tenure-track assistant professor of Mechanical Engineering at McGill University, Montreal, Canada, starting in 2014.

- William Lai (M.S., graduated in May 2011), Aerospace Engineering (Major: Engineering Mechanics), Iowa State University.
M.S. Thesis: Characteristics of dielectric elastomers and fabrication of dielectric elastomer actuators for artificial muscle applications.
- William Lai (PhD, Expected June 2014), Analysis and Fabrications of Planar Dielectric Elastomer Actuators Capable of Complex 3D Deformation, Aerospace Engineering, Iowa State University

4. Appendixes

PDE Boundary Control for Flexible Articulated Wings on a Robotic Aircraft

Aditya A. Paranjape, *Member, IEEE*, Jinyu Guan, Soon-Jo Chung, *Senior Member, IEEE*,
and Miroslav Krstic, *Fellow, IEEE*

Abstract—This paper presents a boundary control formulation for distributed parameter systems described by partial differential equations (PDEs) and whose output is given by a spatial integral of weighted functions of the state. This formulation is directly applicable to the control of small robotic aircraft with articulated flexible wings, where the output of interest is the net aerodynamic force or moment. The deformation of flexible wings can be controlled by actuators that are located at the root or the tip of the wing. The problem of designing a tracking controller for wing twist is addressed using a combination of PDE backstepping for feedback stabilization and feed-forward trajectory planning. We also design an adaptive tracking controller for wing tip actuators. For wing bending, we present a novel control scheme that is based on a two-stage perturbation observer. A trajectory planning-based feed-forward tracker is designed using only one component of the observer whose dynamics are homogeneous and amenable to trajectory planning. The two components, put together, estimate the external forces and unmodeled system dynamics. The effectiveness of the proposed controllers for twist and bending is demonstrated by simulations. This paper also reports experimental validation of the perturbation-observer-based controller for beam bending.

Index Terms—Distributed parameter systems, nonlinear control systems, robot control, robot motion, unmanned aerial vehicles.

I. INTRODUCTION

THERE is a considerable interest in developing robotic aircraft, which is inspired by birds and bats [10], [16], [20], [43] and insects [13]–[15], [60]. While insect wings can be modeled as simple rigid wings, both wing flexibility and wing articulation are believed to play a key role in flight performance and agility for bird and bat flight [43], [54]. A new concept to control microaerial vehicles (MAVs), which uses wing articulation and is inspired by bird and bat flight, was introduced by Paranjape and coauthors [39], [40]. The concept lends itself readily to aeroelastic tailoring, which is seen as an asset in the development of agile MAVs [26], [39], [50], [55]. Wing flexibility not

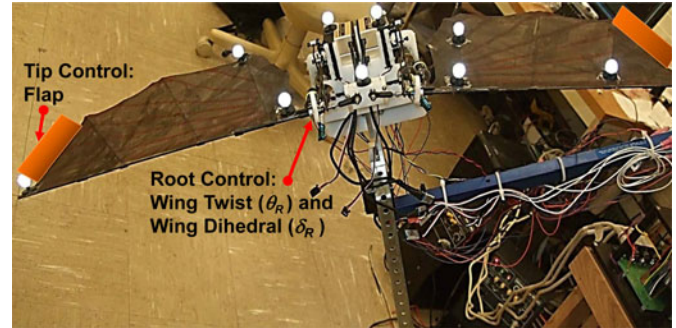


Fig. 1. Robotic bat testbed, where the control laws proposed in this paper can be tested [10], [16].

only improves aircraft performance and stability passively, but can also be actuated actively for control [1], [39], [55]. Fig. 1 shows a robotic bat testbed, which was developed at the University of Illinois at Urbana-Champaign (UIUC) by the authors of [10] and [16]. Each wing is actuated at the root, and during experiments, the motion of each wing as well as the body can be measured in real time for feedback control. It provides a suitable platform to test the controllers that are developed in this paper.

Broadly speaking, continuum distributed parameter systems (DPS) such as flexible wings can be controlled in two ways: distributed control and boundary control. The former approach relies on a series or a network of actuators and sensors that are distributed over the system. The latter approach relies on actuators that are deployed only on the boundary of the system under consideration. For practical engineering applications, the most important benefit of boundary control is the reduction in the number of actuators. Despite a number of bio-inspired examples of distributed actuation, it is evident in robotic applications that implementing a distributed actuation scheme would incur substantial penalties in weight as well as costs. A distributed array of sensors is considerably cheaper and less cumbersome to implement than an array of distributed actuators. The benefits of distributed actuation can be made up, in part, by a combination of good mechanical design and effective boundary control.

A. Literature Review

Structural stability of the wing is governed by its geometry and speed. Moreover, a typical flexible wing has at least two elastic degrees of freedom for deformation—bending and twisting—in addition to the rigid rotations at the root. The structural dynamics of the wing are coupled to the rigid body dynamics of the aircraft [39]. It has been demonstrated in the literature that aeroelastic instabilities such as wing divergence and flutter

Manuscript received May 20, 2012; revised September 30, 2012; accepted January 12, 2013. Date of publication February 11, 2013; date of current version June 3, 2013. This paper was recommended for publication by Associate Editor M. Vendittelli and Editor B. J. Nelson upon evaluation of the reviewers' comments. This work was supported in part by the Air Force Office of Scientific Research under the Young Investigator Award Program (FA95500910089) and in part by the U.S. Army Research Office under Award W911NF-10-1-0296.

A. A. Paranjape and S.-J. Chung are with the Department of Aerospace Engineering, University of Illinois at Urbana-Champaign, Urbana, IL 61801 USA (e-mail: paranja2@illinois.edu; sjchung@illinois.edu).

J. Guan is with Lockheed Martin Corporation, Orlando, FL 32819 USA (e-mail: guan23@illinois.edu).

M. Krstic is with the Center for Control Systems and Dynamics, University of California, San Diego, La Jolla, CA 92093 USA (e-mail: krstic@ucsd.edu).

Color versions of one or more of the figures in this paper are available online at <http://ieeexplore.ieee.org>.

Digital Object Identifier 10.1109/TRO.2013.2240711

can be mitigated using flap-based effectors [3], [46] or passive energy sinks for flutter [25].

There is a substantial amount of literature on boundary control theory of partial differential equations (PDEs) (see [8], [9], [12], [30]–[32], [47] for material pertinent to this paper and references cited therein). There are two sets of methods for boundary control of PDEs. The first set consists of methods that convert the PDEs into ordinary differential equations using approximation methods such as those of Galerkin or Rayleigh-Ritz [9], [22], or using operator theoretic tools [4], [5], [11], [27], [33], [34]. The second set of methods leaves the PDEs intact, and uses a “model-following” approach as described in a recent book by Krstic and Smyshlyaev [30].

A finite-state approximation to a PDE may wrongly render fundamental system theoretic properties like controllability and observability into functions of the approximation [8]. Stability analysis that is based on a finite-state approximation is vulnerable to spillover instabilities which arise due to inadequate accounting of the residual modes [2], [37]. On the other hand, keeping PDEs intact makes the control law design more intuitive. A PDE-based approach has been used for maneuvering robotic arms [30], [44], controlling the Navier–Stokes model [58], and suppressing vibrations in a flexible beam [21]. A gain-scheduling-based approach for nonlinear PDEs has been presented in [52], while Krstic and Smyshlyaev [31] derived an adaptive controller for parabolic PDEs.

There are several PDE and ODE controller designs in the literature to stabilize and control beam bending [17], [21], [28], [33], [34], [52], [56], although the literature mostly concerns bending that is encountered in loaded cables, structural beams, or robotic arms. Flexible wings of robotic aircraft are unique because they experience a closed-loop interaction with the flow field around them. The loop closure happens due to the flow field itself being dependent on the wing deformation, which creates a highly nonlinear system whose modeling is susceptible to significant structural and parametric uncertainties. This necessitates a control design approach, where the control parameters can be tuned with very limited information about the system, and traditionally successful and applied methods for DPS, such as [5], [33], [34], need to be replaced by a more “adaptive” approach, which can tune the control parameters to appropriate functions of the system parameters.

B. Main Contributions

This paper presents a boundary control problem for wing twist (second-order hyperbolic PDE) as well as bending (fourth-order Euler–Bernoulli beam PDE), which could be applied to a wider class of PDEs, including flexible aircraft wings and robotic arms. One highlight of our approach is that it requires minimal information about the system dynamics, and the control laws are themselves in quite a tractable form, which makes them easy to apply to a real physical system. The stability of the controlled system is analyzed rigorously.

The main contributions of this paper are as follows.

- 1) The PDE control objective that is considered in this paper is unique since the controller minimizes a tracking error of

a time-varying net aerodynamic force or moment, rather than following a deformed wing shape. An abstraction of this control objective is to ensure that some weighted integral of the twisting angle equals the prescribed value. A similar idea for a more general class of PDEs has been explored in [8] and [9] in the context of spatially distributed control.

- 2) We design a tracking controller for wing twist based on trajectory-planning and a PDE backstepping-based stabilizer. The procedure is called backstepping because it involves a Volterra operator with a lower triangular structure similar to backstepping transformation for ordinary differential equations [29], [30], and allows the controller acting at the boundary to compensate for the undesired (unmatched) dynamics.
- 3) With the integral of wing twist as the output, and shear force at the wing tip as the input, we show that the twist dynamics have a finite relative degree, thereby permitting a traditional ODE-based approach to control design. The tracking controller increases the stability margin of the twist dynamics by a factor of 16. An adaptive controller for a limited class of parametric uncertainties is also derived for tip-based actuators in general, and root-based actuators, when the output is the rolling moment.
- 4) We present a novel perturbation-observer-based controller to facilitate a trajectory-planning-based tracking controller for bending. The output of interest is the displacement of the wing tip. The perturbation observer, which is designed here uses adaptation to estimate the external forces acting on the system. The observer is split into a “particular” component and a “homogeneous” component (the notions are made more precise later). Since the homogeneous component is stable and not driven directly by external feedback, it is simpler to design a control law for it. The same control signal is sent to the actual system, whose states then converge exponentially to a region around the observer states.
- 5) We experimentally validate the perturbation-observer-based controller for a beam, which is controlled at the wing boundary.

This paper is organized as follows. The problem formulation is explained in Section II. A backstepping-based tracking controller for wing twist, which is inspired by [30], is derived in Section III. A controller for wing twist with actuation at the wing tip and its adaptive version are presented in Section IV. A controller to track tip displacement commands is derived for the bending dynamics in Section V, where an observer-based approach is introduced. Numerical simulations are presented in Section VI. Finally, experimental validation of the perturbation-observer-based control of beam bending is presented in Section VII.

II. MOTIVATION AND PROBLEM FORMULATION

The motivation to consider the problem of boundary control of beams stems from the problem of controlling flexible wings for agile aircraft maneuvers. Suppose that the wing has length

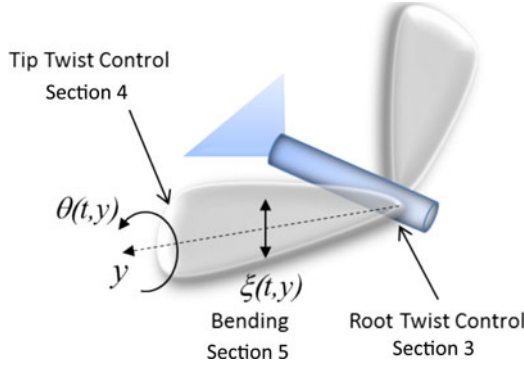


Fig. 2. Figure showing the problems addressed in this paper.

L , a mass per unit span of \tilde{m} , and let y denote the spanwise coordinate. Furthermore, let $\xi \triangleq \xi(t, y)$ and $\theta \triangleq \theta(t, y)$ denote the bending and twist displacements, respectively, as shown in Fig. 2. Let EI_b and $G\tilde{J}$ denote the bending and torsion stiffness, respectively, where I_b is the second moment of area of the cross section about the local bending axis, and \tilde{J} is the torsional constant. Let I_p denote the polar moment of inertia of the wing cross section.

The resultant wind velocity at a given point on the wing \mathbf{u} is a sum of the aircraft flight speed \mathbf{u}_B (measured in the body axis) and the wing vibration rate $\mathbf{u}_f = [0 \ 0 \ \dot{\xi}]^T$ so that $\mathbf{u} = \mathbf{T}_{WB}\mathbf{u}_B + \mathbf{u}_f(y)$, where \mathbf{T}_{WB} is the rotation matrix from the body frame to the local wing frame. Let c denote the wing chord length. Let $x_e c$ denote the distance between the center of mass and the shear center of the wing, and $x_a c$ the distance between the aerodynamic center and shear center. The wing is loaded transversely with a load F_b , which depends on the wind velocity, inertial effects that arise from aircraft acceleration and added mass effect, and gravity. An aerodynamic model to calculate F_b , which is based on an ODE approximation for the time-varying flow dynamics on the wing, can be found in [18].

Then, the PDE model of the structural dynamics of the right wing is given by

$$\begin{bmatrix} \tilde{m} & -\tilde{m}x_e c \\ -\tilde{m}x_e c & I_p \end{bmatrix} \begin{bmatrix} \xi_{tt} \\ \theta_{tt} \end{bmatrix} + \begin{bmatrix} \eta EI_b \xi_{tyyyy} + EI_b \xi_{yyyy} \\ -\eta G\tilde{J} \theta_{tyy} - G\tilde{J} \theta_{yy} \end{bmatrix} = \begin{bmatrix} F_b(\xi_y, \theta, \mathbf{u}, \dot{\mathbf{u}}_B) \\ -x_a c F_b(\xi_y, \theta, \mathbf{u}, \dot{\mathbf{u}}_B) \end{bmatrix} \quad (1)$$

where the subscripts t and y denote partial derivatives, i.e., $\xi_{tt} = \frac{\partial^2 \xi}{\partial t^2}$, $\xi_{tyyyy} = \frac{\partial^4 \xi}{\partial t \partial y^4}$, and so on. A similar equation can be derived for the left wing as well. The boundary conditions for tip-based actuation are given by

$$\begin{aligned} \xi(t, 0) = \xi_y(t, 0) = \xi_y(t, L) = 0 \\ \xi_{yyy}(t, L) = \frac{F_{\text{tip}}(t)}{EI_b}, \quad \theta(t, 0) = 0, \quad \theta_y(t, L) = \frac{M_{\text{tip}}(t)}{G\tilde{J}} \end{aligned} \quad (2)$$

while those for root-based actuation (also shown in Fig. 1) are

$$\begin{aligned} \xi(t, 0) = \xi_{yy}(t, L) = 0 = \xi_{yyy}(t, L) = 0 \\ \xi_y(t, 0) = \delta_R(t), \quad \theta(t, 0) = \theta_R(t), \quad \theta_y(t, L) = 0. \end{aligned} \quad (3)$$

Note that both root and tip control configurations have one Neumann and one Dirichlet boundary condition. In (2) and (3), F_{tip} and M_{tip} are the applied tip shear force and twisting moment, respectively. The root actuation variables, δ_R and θ_R , are the rigid dihedral (up and down motion) and wing incidence angles. The term η denotes the Kelvin–Voigt damping coefficient. It need not be the same for bending and twisting in general.

The right-hand side (RHS) of (1) depends on $\dot{\mathbf{u}}_B$, which is given by

$$\begin{aligned} m(\dot{\mathbf{u}}_B + S(\boldsymbol{\omega}_B)\mathbf{u}_B) + \tilde{m} \int_w (\dot{\mathbf{u}}_f + S(\boldsymbol{\omega}_B)\mathbf{u}_f) dy = \mathbf{F}_{\text{net}} \\ \mathbf{J}\dot{\boldsymbol{\omega}}_B + S(\boldsymbol{\omega}_B)\mathbf{J}\boldsymbol{\omega}_B + \int_w (I_p(y)\dot{\boldsymbol{\omega}}_f + S(\boldsymbol{\omega}_B)I_p(y)\boldsymbol{\omega}_f) dy = \mathbf{M}_{\text{net}} \end{aligned} \quad (4)$$

where m is the total mass of the aircraft, \mathbf{J} is the moment of inertia tensor for the aircraft, \int_w denotes integration over the wing, $S(\cdot)$ denotes the cross product, and \mathbf{F}_{net} and \mathbf{M}_{net} represent the net external (aerodynamic + gravitational) force and moment on the aircraft. Furthermore, $\boldsymbol{\omega}_B$ and $\boldsymbol{\omega}_f = [0 \ \dot{\theta} \ 0]^T$ are vector representations of the aircraft angular velocity and the twist rate of the wing, with components in the aircraft body axes. The dynamics of the motion of the center of gravity of the aircraft, arising from the movement of the wings, have been ignored. See [39] for a detailed and more general derivation of the equations of motion. The important point, though, is that the structural dynamics of the wing are coupled to the flight dynamics of the complete aircraft, which are nonlinear in their own right, which makes control design a challenging assignment.

Physically, F_{tip} and M_{tip} can be realized by using wing tip flaps, not unlike the outboard feathers on the wings of a bird. Indeed, trailing-edge effectors have been demonstrated to be effective at wing flutter suppression as well [3]. On the other hand, δ_R and θ_R are easier to control, and the capability for root actuation is present naturally in flapping wing aircraft.

Problem Formulation

The control objective is to ensure that

$$\lim_{t \rightarrow \infty} \left(\int_0^L \theta(t, y) dy - H(t) \right) = 0 \quad (\text{net lift}) \quad (5)$$

$$\lim_{t \rightarrow \infty} \left(\int_0^L y \theta(t, y) dy - H_l(t) \right) = 0 \quad (\text{rolling moment}) \quad (6)$$

$$\lim_{t \rightarrow \infty} \left(\int_0^L \xi_y(t, y) dy - R(t) \right) = \lim_{t \rightarrow \infty} (\xi(t, L) - R(t)) = 0 \quad (\text{bending displacement of the tip}) \quad (7)$$

where $H(t)$, $H_l(t)$, and $R(t)$ are sufficiently smooth time-varying signals. Although we state asymptotic convergence as the objective, we will prove exponential convergence to a uniform ultimate bound. The net lift produced by the wing is $\int_0^L 0.5\rho\|\mathbf{u}\|^2 c C_L(y, \alpha, \theta) dy$, where ρ is the air density, $\|\mathbf{u}\|$ is the local wind speed, and C_L is the coefficient of lift, which depends on the angle of attack of the aircraft α , and the local wing twist angle θ . Depending on the aerodynamic theory, C_L may be a nonlinear function of α and θ , and it is almost always a function

of y for a finite-span wing [36]. The term $\int_0^L \xi_y(t, y) dy = \xi(L)$ is a measure of the effective wing dihedral, which is a key yaw control parameter [39]. It is approximately the ratio of two components of F_b . The first points are along the y direction in Fig. 2, and the second points upward. Hence, it is a measure of the amount of side (y -) force produced by the wing which, in turn, produces a yawing moment on the aircraft.

Remark 1: The well-posedness of the closed-loop systems considered here can be shown by proving that the input–output map of the system exists and is bounded [7], [48]. For the twisting dynamics actuated by root control, this is achieved by designing the control to map the system onto well-posed and exponentially stable dynamics. For twisting dynamics actuated at the wing tip, the input–output map is actually a finite-order ODE, and its well-posedness follows from the standard existence and uniqueness theorems for ODEs. The well-posedness of the closed-loop bending dynamics can be shown using a transfer function approach [7], [12].

Remark 2: It was shown in [12] that the boundary condition $EI_b \xi_{yyy} = F_{\text{tip}}$ in (2) needs to be replaced with $EI_b (\xi_{yyy} + \eta \xi_{tyyy}) = F_{\text{tip}}$ when the Kelvin–Voigt damping coefficient $\eta \neq 0$ in order to ensure the well-posedness of the PDE. Note, however, that this replacement essentially creates a low-pass filter for the control input F_{tip} . As long as the dominant frequencies in F_{tip} are smaller than the cutoff frequency $1/\eta$, the boundary condition in (2) is sufficiently accurate for control design. Moreover, the Kelvin–Voigt damping term is physically akin to distributed load [F_b in (1)] on the wing, which does not affect the boundary conditions.

III. ROOT-BASED TRACKING CONTROLLER FOR LIFT

In this section, we consider a twist PDE with constant coefficients. The PDE backstepping method is used to design a controller, which ensures $\lim_{t \rightarrow \infty} (\int_0^L \theta dy - H(t)) = 0$ [see (5)]. The twisting dynamics, with the angle of incidence at the wing root as the control input and the wing tip free, are given by

$$\begin{aligned} \theta_{tt}(t, y) - b\theta_{tyy}(t, y) - a\theta_{yy}(t, y) &= M\theta(t, y) \\ \theta(t, 0) &= U(t), \quad \theta_y(t, L) = 0. \end{aligned} \quad (8)$$

We first make a coordinate transformation and define

$$w(t, y) = \int_L^y \theta(t, x) dx. \quad (9)$$

Physically, $w(t, y)$ measures the lift, which is generated by the outboard section of the wing starting at y and terminating at the tip. Note that $\theta_y(t, L) = 0$ at the free end $y = L$. Hence, it follows that

$$\begin{aligned} w_{tt}(t, y) &= \int_L^y \theta_{tt}(t, x) dx \\ &= \int_L^y (b\theta_{txx}(t, x) + a\theta_{xx}(t, x) + M\theta(t, x)) dx \\ &= b\theta_{ty}(t, y) + a\theta_y(t, y) + Mw(t, y) \\ &= bw_{tyy}(t, y) + aw_{yy}(t, y) + Mw(t, y). \end{aligned} \quad (10)$$

Thus, the dynamics of w are described by the PDE

$$w_{tt} - bw_{tyy} - aw_{yy} = Mw, \quad w(t, L) = 0, \quad w_y(t, 0) = U(t) \quad (11)$$

where $U(t)$ is the control signal [θ_R in (3)], and recall that $a = G\tilde{J}/I_p$ and $b = \eta a$. Furthermore, we defined M so that $M\theta = -x_a cF_b/I_p$, where F_b is a linear function of θ . Note that $w_y(t, y) = \theta(t, y)$. The control objective is now recast to ensure that $\lim_{t \rightarrow \infty} w(t, 0) = -H(t)$.

The method presented in this section rests on the following steps:

- 1) obtain a backstepping transformation $w \mapsto v$, which maps the dynamics in (11) into desired stable dynamics;
- 2) compute the boundary condition $v(t, 0)$; and
- 3) derive a trajectory planning-based design with the boundary conditions of the v dynamics.

Step 1 (Volterra transform): Define the Volterra transform

$$v(t, y) = w(t, y) - \int_L^y k(y, x)w(t, x) dx \quad (12)$$

and the v -dynamics

$$v_{tt} - bv_{tyy} - av_{yy} = Mv - bpv_t - apv, \quad v(t, L) = 0, \quad p > 0. \quad (13)$$

Note that we have prescribed only one boundary condition for v , which follows from the fact that $w(t, L) = 0$. The second boundary condition $v_y(t, 0)$ has to be calculated to ensure that the $\lim_{t \rightarrow \infty} w(t, 0) \approx -H(t)$ (this is what we can guarantee in practice, in place of asymptotic convergence). The target dynamics in (13) are very similar to those designed for the regulation problem in [30, ch. 7, pp. 79–89]. However, the boundary conditions are chosen to match the control objective in (5). For the regulation problem ($H = 0$), we can prescribe $v_y(t, 0) = v(t, L) = 0$ [30]. In contrast, in order to track a nonzero, time-varying $H(t)$, we choose $v_y(t, 0)$ by using trajectory planning.

We first establish the stability of (13) with homogeneous boundary conditions, i.e., $v_y(t, 0) = v(t, L) = 0$.

Proposition 1: The target dynamics (13) with $v_y(t, 0) = v(t, L) = 0$ are stable if and only if

$$p > \max \left(\frac{M}{a} - \frac{\pi^2}{4L^2}, -\frac{\pi^2}{4L^2} \right). \quad (14)$$

Proof: Using the method of separation of variables, it is easy to check that the eigenvalues of the resulting system are the solutions of

$$\begin{aligned} \lambda^2 + b(\nu^2 + p)\lambda + (a(\nu^2 + p) - M) &= 0 \\ \text{where } \nu &= \frac{2n+1}{2} \frac{\pi}{L}, \quad n = 0, 1, 2, \dots \end{aligned} \quad (15)$$

The target dynamics are stable if and only if the control design parameter p satisfies (14). ■

Next, we solve for $k(y, x)$ in the Volterra transform (12).

Proposition 2: The gain kernel $k(y, x)$ in (12) is the solution of the Klein–Gordon PDE

$$\begin{aligned} k_{xx}(y, x) - k_{yy}(y, x) &= -pk(y, x), \quad k(y, L) = 0 \\ k(y, y) &= \frac{p}{2}(L - y) \end{aligned} \quad (16)$$

and given in terms of the modified Bessel function, $I_1(\cdot)$ ¹

$$k(y, x) = p(L - x) \frac{I_1(\sqrt{p((L - y)^2 - (L - x)^2)})}{\sqrt{p((L - y)^2 - (L - x)^2)}}. \quad (17)$$

Proof: We can derive expressions for v_{tt} and v_{yy} from (12)

$$\begin{aligned} v_{tt} &= w_{tt} - \int_L^y k(y, x)w_{tt}(x)dx \\ &= bw_{yy} + aw_{yy} + Mw \\ &\quad - \int_L^y k(y, x)(bw_{tx}(x) + aw_{xx}(x) + Mw(x))dx \\ &= bw_{yy} + aw_{yy} + Mw - \int_L^y k(y, x)Mw(x)dx \\ &\quad - \int_L^y k_{xx}(y, x)(bw_t(x) + aw(x))dx \\ &\quad - k(y, y)(bw_{ty}(y) + aw_y(y)) + k_x(y, y)(bw_t(y) + aw(y)) \\ &\quad + k(y, L)(bw_{ty}(L) + aw_y(L)). \end{aligned} \quad (18)$$

The expression for v_{yy} can be derived as follows:

$$\begin{aligned} v_y(y) &= w_y(y) - k(y, y)w(y) - \int_L^y k_y(y, x)w(t, x)dx \\ v_{yy}(y) &= w_{yy}(y) - 2k_y(y, y)w(y) \\ &\quad - k_{xx}(y, y)w(y) - k(y, y)w_y(y) - \int_L^y k_{yy}(y, x)w(t, x)dx. \end{aligned} \quad (19)$$

The expression for $v_{t yy}$ is similar to that for v_{yy} . We substitute (18) and (19) into (13) and isolate the coefficients of w and w_y in the integrand as well as outside the integral. This yields (16). ■

Step 2 (Boundary condition, $v(t, 0)$, for tracking): We have already ascertained that $v(t, L) = 0$. From (12), it follows that

$$v(t, 0) = w(t, 0) + \int_0^L k(0, x)w(t, x)dx \quad (20)$$

which does not yield an exact relationship between $H(t)$ defined in (5) and $v(t, 0)$. Instead, we need to determine an appropriate reference value for $v(t, 0)$, denoted by $H_r(t)$, which ensures that $w(t, 0)$ approximately tracks $-H(t)$. For example, we could approximate $w(t, x) \approx f_1(x)w(t, 0)$, $f_1(0) = 1$, where $f_1(x)$ denotes the shape of the first twisting mode. Thus, we set $H_r(t) = -H(t)(1 + \int_0^L k(0, x)f_1(x)dx)$. It is important to appreciate that ignoring the higher modes has no repercussions for stability since it is guaranteed separately. At the same time, it may be necessary to include more than one mode if there

are tight bounds on the tracking error. A similar approach, which is based on backstepping, but for constant reference signals, has been derived in [49].

Step 3 (Trajectory planning for wing twist): We design a trajectory planning-based algorithm (see [30], Ch. 12). We define a new state v^r , where the superscript “ r ” denotes the reference value. The dynamics of v^r are given by a PDE that is identical to (13):

$$v_{tt}^r - bv_{t yy}^r - av_{yy}^r = Mv^r - bpv_t^r - apv^r, \quad v^r(t, L) = 0 \quad (21)$$

where $v_y^r(t, 0)$ is the control input to be designed using trajectory planning to ensure that $v^r(t, 0)$ tracks $H_r(t)$.

Since $v^r(t, L) = 0$, we expand $v^r(t, y)$ as a polynomial

$$v^r(t, y) = \sum_{j=1}^N \eta_j(t) \frac{(L - y)^j}{j!}. \quad (22)$$

Substituting for v^r into (21), we get

$$\ddot{\eta}_j(t) + bp\dot{\eta}_j(t) + (ap - M)\eta_j(t) = b\eta_{j+2}(t) + a\eta_{j+2}(t). \quad (23)$$

The requirement that $v^r(t, 0) = H_r(t)$ gives

$$\sum_{j=1}^N \eta_j(t) \frac{L^j}{j!} = H_r(t). \quad (24)$$

The value of N can be chosen on a case-by-case basis. As an illustration, if we truncate the series at $N = 3$, we get

$$\ddot{\eta}_1(t) + bp\dot{\eta}_1(t) + (ap - M)\eta_1(t) = b\dot{\eta}_3(t) + a\eta_3(t). \quad (25)$$

A similar equation can be obtained for $\eta_2(t)$, with the RHS equal to zero. Therefore, η_2 converges to zero exponentially fast and can be ignored. The requirement that $v^r(t, 0) = H_r(t)$ gives

$$\eta_1(t)L + \eta_3(t)\frac{L^3}{6} = H_r(t). \quad (26)$$

Substituting $\eta_3(t) = \frac{6}{L^3}(H_r(t) - \eta_1(t)L)$ into (25) gives

$$\begin{aligned} \ddot{\eta}_1(t) + b\left(p + \frac{6}{L^2}\right)\eta_1(t) + \left(ap - M + \frac{6a}{L^2}\right)\eta_1(t) \\ = \frac{6}{L^3}\left(b\dot{H}_r(t) + aH_r(t)\right). \end{aligned} \quad (27)$$

Then, $v_y^r(t, 0)$ is calculated by differentiating both sides of (22)

$$v_y^r(t, 0) = -\eta_1(t) - \eta_3(t)\frac{L^2}{2} = 2\eta_1(t) - \frac{3H_r(t)}{L} \quad (28)$$

where $v_y^r(t, y) = \partial v^r(t, y)/\partial y$.

Proposition 3: Based on Steps 1–3, we now define $U(t) = \theta(t, 0) = w_y(t, 0)$ as illustrated in the block diagram in Fig. 3. First, we set the boundary condition $v_y(t, 0) = v_y^r(t, 0)$. Let $\tilde{v}(t, y) = v(t, y) - v^r(t, y)$. It is straightforward to check that the dynamics of \tilde{v} are given by the exponentially stable PDE

$$\begin{aligned} \tilde{v}_{tt} - b\tilde{v}_{t yy} - a\tilde{v}_{yy} &= M\tilde{v} - bp\tilde{v}_t - ap\tilde{v} \\ \tilde{v}(t, L) &= \tilde{v}_y(t, 0) = 0. \end{aligned} \quad (29)$$

Thus, in particular, it follows that $v(t, 0) \rightarrow v^r(t, 0)$ exponentially fast and $v(t, 0)$ tracks $H_r(t)$.

¹A modified Bessel function $I_n(y)$ satisfies $y^2 I_n''(y) + y I_n'(y) - (y^2 + n^2) I_n(y) = 0$.

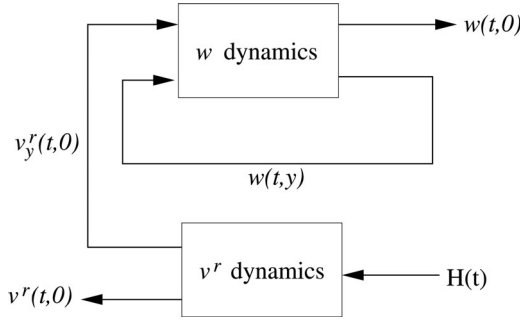


Fig. 3. Block diagram showing the tracking controller for twist (θ) dynamics. This structure is identical to the classic strict feedback structure for systems described by ODEs [29].

An expression for $v_y(t, y)$ can be found by differentiating both sides of the Volterra transform in (12)

$$v_y(t, y) = w_y(t, y) - k(y, y)w(t, y) - \int_L^y k_y(y, x)w(t, x)dx. \quad (30)$$

Finally, the control input $U(t)$ is calculated

$$U(t) = \theta(t, 0) = w_y(t, 0) = v_y^r(t, 0) + \underbrace{k(0, 0)w(t, 0) - \int_0^L k_y(0, x)w(t, x)dx}_{\text{feedback}} \quad (31)$$

where $v_y^r(t, 0) \rightarrow v_y(t, 0)$ exponentially fast. The term $v_y^r(t, 0)$ is a feed-forward tracking term in the control signal, while the remaining two terms act as feedback stabilizers.

We now assert that the closed-loop system is stable in the sense of \mathcal{L}_2 . Given a quantity $\Omega(t, y) \in \mathbb{R}$, define

$$\|\Omega(t)\|_{\mathcal{L}_2} = \sqrt{\int_0^L \Omega(t, y)^2 dy}.$$

Theorem 1: The closed-loop w -dynamics (11) and (31) are stable in the sense of \mathcal{L}_2 , i.e., $\|w(t)\|_{\mathcal{L}_2}$ is bounded.

Proof: Using a Lyapunov stability argument, it can be shown that $\|v(t)\|_{\mathcal{L}_2}$ is bounded at all times. Since (12) is a diffeomorphism, we can find another function $l(y, x)$ (which is expressed in terms of the Bessel function J_1 [30]) such that $w(t, y) = v(t, y) - \int_L^y l(y, x)v(t, x)dx$, and $l(y, x)$ is bounded for all $0 \leq y \leq x \leq L$. Since the $\|v(t)\|_{\mathcal{L}_2}$ is bounded, it follows that $\|w(t)\|_{\mathcal{L}_2}$ is bounded. ■

Remark 3: The approach that is detailed in this section also works when the RHS is nonlinear, i.e., $M \equiv M(y)$. Linearization can be used in the general case, where the RHS is of the form $M(y, \theta_1, \theta_2)$. It has been shown in [38] that a regulator based on (31) can stabilize the twisting dynamics in the presence of these nonlinearities. The analysis is not repeated here.

Remark 4: A few observations are worth noting here.

- 1) For stability, it is essential that $b > 0$, i.e., the Kelvin–Voigt damping coefficient is always positive. The aerodynamics could introduce negative damping, but it can be compensated by the term $b p v_t$, and wing flutter can be prevented.

The need to compensate for negative damping imposes an additional constraint on p .

- 2) Damping and stiffness cannot be added independently. They are added in the ratio b/a .
- 3) The controller in (31) requires that the twist angle at all points on the wing be known. This difficulty can be circumvented by designing a PDE-based observer [30] or, practically, using a series of distributed sensors and fitting their output with an a priori designed spline.
- 4) Finally, the control law does not require that a , b , or M be known for the purpose of regulation. We only need to know bounds on a and M to choose the gain p .

IV. BOUNDARY CONTROL OF TWISTING MOTION: WING TIP CONTROL

Although backstepping can be employed when the twisting moment at the wing tip is used as the control input, it turns out that there is a simpler alternative, as described in this section. It relies on the fact that the system has a finite relative degree for the input–output combination of the tip moment and $\int_0^L \theta(t, y)dy$, respectively.

A. Tip Boundary Control When All Parameters Are Known

As in the previous section, one can design a backstepping controller for the case where a control moment is applied to the free end ($y = L$) of the wing, while the other end ($y = 0$) is clamped. In fact, the procedure in both cases is identical, although the final expressions for the control law differ slightly. Alternately, in the case of MAVs, one may do without a stabilizing controller. The “tracking half” of the controller may be designed by using the output measurements. This method is useful for adaptive designs as well. We consider the wing model

$$\theta_{tt} - b\theta_{tyy} - a\theta_{yy} = M\theta, \quad \theta(t, 0) = 0, \quad \theta_y(t, L) = u(t) \quad (32)$$

where the control input is a moment that is applied at the wing tip, ($u(t) = \theta_y(L, t) = M_{\text{tip}}$ in (2), and $b = \eta a = \eta G \tilde{J} / I_p$. Furthermore, we defined M so that $M\theta = -x_a c F_b / I_p$, where F_b is a linear function of θ .

Theorem 2: A dynamic controller of the form

$$b\dot{u}(t) + au(t) = \ddot{H}(t) - MH(t) - (M + k)e(t) - k_c \dot{e}(t) + a\theta_y(t, 0) + b\theta_{ty}(t, 0) \quad (33)$$

ensures the following control objective:

$$\lim_{t \rightarrow \infty} \left(\int_0^L \theta(t, y)dy - H(t) \right) = 0. \quad (34)$$

Proof: Let $e(t) = \int_0^L \theta(t, y)dy - H(t)$ denote the error, which needs to be regulated. Then,

$$\begin{aligned} \ddot{e} &= \int_0^L \theta_{tt}(t, y)dy - \ddot{H}(t) \\ &= \int_0^L (a\theta_{yy} + b\theta_{tyy} + M\theta)dy - \ddot{H}(t) \\ &= a\theta_y(t, L) - a\theta_y(t, 0) + b\theta_{ty}(t, L) - b\theta_{ty}(t, 0) \end{aligned}$$

$$\begin{aligned}
 & + Me(t) - \ddot{H}(t) + MH(t) \\
 & = b\dot{u}(t) + au(t) - a\theta_y(t, 0) - b\theta_{ty}(t, 0) \\
 & + Me(t) - \ddot{H}(t) + MH(t). \tag{35}
 \end{aligned}$$

The controller (33) renders the system into a globally exponentially stable linear system with $k_c > 0$, $k > 0$

$$\ddot{e}(t) + k_c \dot{e}(t) + ke(t) = 0. \tag{36}$$

Hence proved. \blacksquare

Remark 5: The control law in (33) suggests that θ need not be monitored or measured at all locations on the wing. Instead, only $\theta_y(t, 0)$ needs to be measured or estimated. The reference signal $H(t)$ is known. It may be difficult to inject damping because $\dot{e}(t)$ is the rate of change of the lift and, in practice, would require differentiating noisy acceleration signals. Another interesting observation is that although the PDE system had an infinite relative degree when the root twist was chosen as the control input, the relative degree is 2 when twisting moment at the wing tip is considered as the input. Finally, the control law design that is described in this section lends itself readily to adaptation if a and/or M are unknown.

B. Tracking and Stability

The problems of tracking and stabilization are distinct because the PDE system (32) is infinite dimensional. Nevertheless, a tracking controller improves stability as described presently. One way to measure the influence of a tracking controller on the stability of the closed-loop system is to set $H = 0$. Make a coordinate transformation $w(t, y) = \int_L^y \theta(t, z) dz$, similar to (9), so that achieving $H = 0$ is equivalent to achieving $w(t, 0) = 0$. It follows that the transformed dynamics, with $H = 0$ obtained by the tracking control algorithm, are given by

$$\begin{aligned}
 & w_{tt}(t, y) - bw_{tyy}(t, y) - aw_{yy}(t, y) \\
 & = Mw(t, y) - bw_{tyy}(t, 0) - aw_{tyy}(t, 0) \\
 & w(t, L) = w(t, 0) = 0, \quad w'(t, 0) = 0. \tag{37}
 \end{aligned}$$

The third boundary condition is not entirely independent. Let $w(t, y) = \eta(t)\phi(y)$. Then, we get

$$\frac{\ddot{\eta}(t) - M\eta(t)}{b\dot{\eta}(t) + a\eta(t)} = \frac{\phi_{yy}(y) - \phi_{yy}(0)}{\phi(y)} = -\lambda^2 \tag{38}$$

where λ is a constant. It follows that the condition for stability (exponential stability to be precise, since the present system is linear) is $M/a < \lambda^2$. The differential equation for $\phi(y)$ in (38) can be solved to get

$$\phi(y) = A \sin(\lambda y) + B \cos(\lambda y) + \phi_{yy}(0)/\lambda^2. \tag{39}$$

The boundary conditions $\phi(0) = \phi_y(0) = 0$ lead to $\phi(y) = B(\cos(\lambda y) - 1)$. Finally,

$$\phi(L) = 0 \implies \lambda = 2n\pi/L, \quad \because \phi(L) = 0, \quad n = 1, 2, \dots \tag{40}$$

Had we not imposed the condition $H(0) = 0$, we would have obtained $M/a < \pi^2/(4L^2)$ as the condition for (exponential) stability. Since the condition for closed-loop stability is given

by $M/a < \lambda^2 = 4\pi^2/L^2$, it follows that the stability margin improves by a factor of 16 by using only the tracking controller, although it does not stabilize the wing for all values of M and a as backstepping does. In principle, the tracking controller converts the wing from a cantilever beam to a clamped-clamped beam. In practice, this translates to the ability to increase the wing flexibility by an order of magnitude, or increase the wing divergence speed fourfold.

C. Adaptive Control for a Wing Tip Actuator

Consider the dynamics in (32) with the objective in (34), and suppose that M is unknown. The control law in (33) is modified so that

$$\begin{aligned}
 b\dot{u}(t) + au(t) & = \ddot{H}(t) - \hat{M}(t)(H(t) + e(t)) - ke(t) \\
 & - k_c \dot{e}(t) + a\theta_y(t, 0) + b\theta_{ty}(t, 0) \tag{41}
 \end{aligned}$$

where $\hat{M}(t)$ is the estimated value of M , and $e(t) = \int_0^L \theta(t, y) dy - H(t)$ denotes the tracking error. The closed-loop tracking error error dynamics are described by the ODE

$$\ddot{e}(t) + k_c \dot{e}(t) + ke(t) = -\tilde{M}(t)(H(t) + e(t)) \tag{42}$$

where $\tilde{M}(t) = \hat{M}(t) - M(t)$. We design a projection-based adaptive law for $\hat{M}(t)$ to ensure that the error $e(t)$ remains bounded with as small a bound as possible. The projection operator, which is denoted by $\text{Proj}(\cdot, \cdot)$, is used commonly in the adaptive control literature [6], [35] for parameter estimation.

Theorem 3: Let $x(t) = [e(t), \dot{e}(t)]^T$. Suppose that there exist positive constants B_1 and B_2 such that $|M| < B_1$ and $|\dot{M}| < B_2$. Then, the following adaptive law

$$\dot{\hat{M}}(t) = \gamma \text{Proj} \left(\hat{M}(t), x^T P \begin{bmatrix} 0 \\ 1 \end{bmatrix} (e(t) + H) \right) \tag{43}$$

with $|\hat{M}(t)| < B_1$ ensures that there exists a positive constant $K(B_1, B_2)$ and a time $T > 0$ such that

$$\|x(t)\|_\infty \leq \|x(t)\|_2 \leq \frac{K(B_1, B_2)}{\sqrt{\gamma}} \forall t \geq T. \tag{44}$$

Proof: see [38].

Remark 6: The bound on $\|x(t)\|_\infty$ can be made arbitrarily small by choosing a large γ . The steady-state beam shape of the wing depends on the steady-state value of the error $\hat{M}(t)$. Finally, it is worth noting that although a and b were assumed to be known, the aforementioned analysis can be repeated to accommodate an unknown a and b as well.

D. Control of Rolling Moment

An abstract measure of the rolling moment is $\int_0^L y\theta(t, y) dy$, which is defined in (6). Let $e_l(t, y) = \int_0^L y\theta(t, y) dy - H_l(t)$, where $H_l(t)$ denotes the reference value of the rolling moment to be tracked, and $e_l(t)$ is the tracking error. Differentiate $e_l(t)$

twice with respect to time

$$\begin{aligned}
\ddot{e}_l(t) &= \int_0^L y \theta_{tt}(t, y) dy - \ddot{H}_l(t) \\
&= \int_0^L y (b \theta_{tyy}(t, y) + a \theta_{yy}(t, y)) dy \\
&\quad + M \int_0^L y \theta(t, y) dy - \ddot{H}_l(t) \\
&= L(b \theta_{ty}(t, L) + a \theta_y(t, L)) - b(\theta_t(t, L) - \theta_t(t, 0)) \\
&\quad - a(\theta(t, L) - \theta(t, 0)) + M e_l(t) + M H_l(t) - \ddot{H}_l(t).
\end{aligned} \tag{45}$$

An interesting observation is that $e_l(t)$ has a relative degree of 2 with respect to $\theta_y(t, L)$ (tip control) as well as $\theta(0)$ (root control). Therefore, a considerably simpler controller than the backstepping controller, on the lines of the adaptive controller in the previous section, can be implemented for a root-based actuator as well. Indeed, in aircraft, the lift is controlled using the horizontal tail, while wing-based flaps (ailerons and spoilers) are used primarily for roll control.

V. ROOT BOUNDARY CONTROL OF WING BENDING

In this section, we first determine the conditions under which there is a significant time-scale separation between the bending and twisting dynamics. When the time-scale separation is sufficient, the control laws for bending and twist can be designed separately, which simplifies the design process considerably in practice. Time-scale separation is used quite routinely to design flight control laws [24], [45], [53], [59]. We introduce one of the main results of this paper—the new perturbation-observer-based method to design a bending controller. In particular, we design a root-based bending controller [δ_R in (3)] using a combination of the perturbation-observer-based approach and trajectory planning. The design of a tip controller [F_{tip} in (2)] is straightforward using the approach that is established in this section, and we demonstrate it experimentally.

The bending PDE in (1) can be written as

$$\begin{aligned}
\tilde{m} \xi_{tt} + \eta E I_b \xi_{tyyy} + E I_b \xi_{yyy} &= F_n(t, y, \xi_t, \theta, \theta_{tt}) \\
\xi(t, 0) = \xi_y(t, L) = \xi_{yyy}(t, L) &= 0, \quad \xi_y(t, 0) = u(t)
\end{aligned} \tag{46}$$

where the control input $u(t) = \delta_R(t)$ in (3) is designed to ensure that $\xi(t, L) = R(t)$ in (7). The acceleration term corresponding $\tilde{m} x_e c \ddot{\theta}$ in (1) has been moved to the RHS and merged into F_b so that $F_n = F_b + \tilde{m} x_e c \ddot{\theta}$. The RHS (46) is independent of ξ , and θ is an average value that is obtained from the faster twist dynamics. Therefore, unlike the twisting dynamics, the onset of instability in the bending dynamics will correspond to the damping becoming negative.

A. Time-Scale Separation in Microaerial Vehicles With Flexible Wings

In [39], it was shown that the time-scale separation between the twisting and bending dynamics is given by the following

approximate relation, when the speed is less than the torsional divergence speed

$$\frac{\omega_\theta}{\omega_\xi} \approx \frac{1.5}{1 + \nu} \frac{L}{c} \tag{47}$$

where ω_θ and ω_ξ denote the angular frequencies of torsion and bending, respectively, ν denotes the Poisson ratio (typically in the range 0.1–0.4), and the ratio L/c is called the aspect ratio of the wing (of the half wing, to be precise). Therefore, the twisting dynamics are faster than the bending dynamics, and moreover, the time-scale separation increases with the aspect ratio, and reduces with increasing flight speed [39]. In most practical situations, a time-scale separation of 3–5 is considered sufficient to design and implement decoupled control laws, i.e., decoupled controllers for bending and twist can be safely designed for wings with aspect ratio $L/c \geq 3$.

Remark 7: Wings with smaller aspect ratios would have to be modeled as plates rather than beams. Although several MAV wings do have aspect ratios smaller than 3 (such as the one built by the authors [40]), their structure consists of a skin wrapped around or on a more traditional beam-like structure. The control design explained in this paper can still be employed for such wings. The two-time-scale approach is rigorously applicable to coupled infinite-dimensional systems, as illustrated for thermal-fluid dynamics in [57], and for flexible structure dynamics in [51]. Moreover, although the coupled dynamics overlap over an infinitely wide frequency range, the slower subsystem has only a tiny fraction of its energy in the (semi-infinite) frequency range, where it overlaps with the faster dynamics (whose entire energy is in that range).

B. Open-Loop Stability of Bending

Assume that the boundary conditions are homogeneous, i.e., $\xi(t, 0) = \xi_y(t, 0) = \xi_{yyy}(t, L) = \xi_{yyy}(t, L) = 0$ for all t . Let $a_b = E I_b / \tilde{m}$ and $b_b = \eta a_b$. Let $F(t, y) = F_n(t, y) / \tilde{m}$, where $F_n(t, y)$ succinctly denotes the RHS of (46). Assume that the flight speed $\|\mathbf{u}_B\|$ is constant.

Proposition 4: Subject to the aforementioned assumptions, the bending dynamics (46) with $u \equiv 0$ are stable if

$$\int_0^L (F(t, y))^2 dy < \left(\frac{\eta E I_b \pi^4}{16 m L^4} \right)^2 \int_0^L (\xi_t(t, y))^2 dy.$$

Proof: Consider the Lyapunov function (in this case, the total \mathcal{L}_2 energy of the beam)

$$V(t) \triangleq V(t, y) = \frac{1}{2} \int_0^L (\xi_t^2 + a_b \xi_{yy}^2) dy. \tag{48}$$

It is quite straightforward to derive the following expressions for $\dot{V}(t)$:

$$\dot{V}(t) = -b_b \int_0^L \xi_{tyy}^2 dy + \int_0^L \xi_t F(t, y) dy. \tag{49}$$

A repeated application of Poincaré's inequality² yields

$$\dot{V}(t) \leq -\frac{b_b \pi^4}{16L^4} \int_0^L \xi_t^2 dy + \int_0^L \xi_t F(t, y) dy.$$

Using the Cauchy–Schwarz inequality, we get

$$\dot{V}(t) \leq -\frac{b_b \pi^4}{16L^4} \int_0^L \xi_t^2 dy + \sqrt{\left(\int_0^L \xi_t^2 dy \right) \left(\int_0^L (F(t, y))^2 dy \right)}.$$

Clearly, if

$$\begin{aligned} \int_0^L (F(t, y))^2 dy &< \left(\frac{b_b \pi^4}{16L^4} \right)^2 \int_0^L \xi_t^2 dy \\ &= \left(\frac{\eta E I_b \pi^4}{16mL^4} \right)^2 \int_0^L \xi_t^2 dy \end{aligned} \quad (50)$$

then the bending dynamics are stable. \blacksquare

The expression for $F(t, y)$ in the simplest case is of the form $F(t, y) = -(\kappa_1 \xi_t + \kappa_2 \xi_t^2) C_L(\theta)$, where $\kappa_1, \kappa_2 > 0$ are essentially constant. If $C_L > 0$ (a reasonable assumption), it follows that $\kappa_1 C_L \xi_t$ injects damping into the system and counters the potentially destabilizing contribution from $\kappa_2 \xi_t^2 \theta$ for sufficiently small values of ξ_t . However, if $C_L(\theta)$ is not uniformly positive, and if it is out-of-phase with ξ_t , $F(t, y)$ could potentially cause the damping to become negative, leading to oscillatory instability in the bending dynamics and trigger wing flutter.

Furthermore, since $\kappa_1 \propto \|\mathbf{u}_B\|$, the flight speed, it follows that (50) can be used to derive a stable envelope for the flight speed and Young's modulus. However, unlike the analysis for wing twist in Section V-A and [39], the analysis is considerably more complicated because of the potentially strong nonlinear contribution from ξ_t^2 at low flight speeds.

C. Perturbation Observer for Root Control of Bending

In this section, we design a high-gain observer-based controller to facilitate a trajectory-planning-based tracking controller for bending. The perturbation observer does not predict the system states. It uses projection-based adaptation to estimate $F(t, y)$ which would be unknown in practical situations, although one may estimate its spatial profile from the wing geometry [36]. The perturbation observer is split into a “particular” component and a “homogeneous” component (the notions will be made more precise in this section). In particular, the homogeneous component is stable and not driven directly by external feedback. Thus, it is simpler to design a “tracking” control law for it. The same control signal is sent to the actual system, whose states then converge exponentially to a bounded envelope around the observer states. Fig. 4 shows a block diagram of the perturbation observer-based controller. It is the PDE analog of feed-forward and feedback control for systems that are described by ODEs. Notice that the reference input, $R(t)$ from (7), enters only the homogeneous component of the perturbation observer, while the feedback from the actual system only enters the particular component.

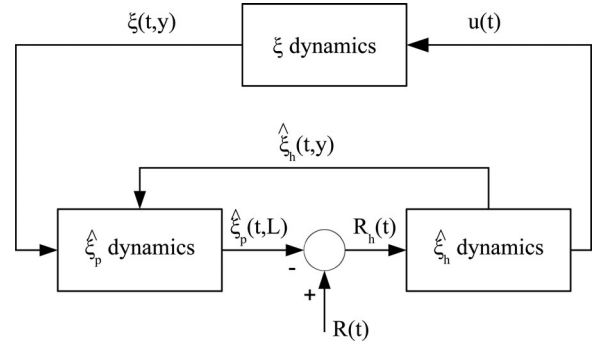


Fig. 4. Block diagram for the perturbation observer coupled to the system dynamics. The control signal $u(t)$ is generated from trajectory planning, while $R(t)$ is the desired reference signal from (7).

Let $F(t, y) = W(t)^T \phi_b(y) + \sigma(t)$, where $W(t)$ and $\sigma(t)$ are unknown and bounded with known bounds. We assume that \dot{W} and $\dot{\sigma}$ are also bounded with known bounds. The set of functions $\phi_b(y)$ can be chosen to get a satisfactory bound on σ , and using a knowledge of the wing geometry [36] (e.g., the force distribution on an elliptical wing is rectangular, and vice versa).

The perturbation observer for the bending dynamics in (46) is designed as a combination of two components, which are called the “particular” component and the “homogeneous” component, for reasons that will become apparent presently. Let $\hat{\xi}_p$ and $\hat{\xi}_h$ denote the states of the particular and homogeneous components, respectively. The dynamics of $\hat{\xi}_p$ and $\hat{\xi}_h$ are described by the following PDEs:

$$\begin{aligned} \hat{\xi}_{p,tt}(t, y) + b_b \hat{\xi}_{p,tyyyy}(t, y) + a_b \hat{\xi}_{p,yyyy}(t, y) \\ = -b_b p \tilde{\xi}_{p,t}(t, y) - a_b p \tilde{\xi}_p(t, y) + \hat{W}(t)^T \phi_b(y) + \hat{\sigma}(t) \\ \hat{\xi}_{p,yy}(t, L) = \hat{\xi}_{p,yyy}(t, L) = \hat{\xi}_p(t, 0) = \hat{\xi}_{p,y}(t, 0) = 0 \end{aligned} \quad (51)$$

for the particular component, where $\tilde{\xi}_p = \hat{\xi}_p - \xi$, and

$$\begin{aligned} \hat{\xi}_{h,tt} + b_b \hat{\xi}_{h,tyyyy} + a_b \hat{\xi}_{h,yyyy} = -b_b p \hat{\xi}_{h,t} - a_b p \hat{\xi}_h \\ \hat{\xi}_{h,yy}(t, L) = \hat{\xi}_{h,yyy}(t, L) = \hat{\xi}_h(t, 0) = 0, \quad \hat{\xi}_{h,y}(t, 0) = u(t) \end{aligned} \quad (52)$$

for the homogeneous component. Note that the homogeneous half is a stable system, and its dynamical equation does not depend on ξ or $\hat{\xi}_p$ (which is why it is called the “homogeneous” component). Moreover, the reference signal $R(t)$ is sent only to the homogeneous component.

We now put together the two components. Define $\hat{\xi} = \hat{\xi}_p + \hat{\xi}_h$. Then, the dynamics of $\hat{\xi}$ are given by

$$\begin{aligned} \hat{\xi}_{tt}(t, y) + b_b \hat{\xi}_{tyyyy}(t, y) + a_b \hat{\xi}_{yyyy}(t, y) \\ = \hat{W}(t)^T \phi_b(y) + \hat{\sigma}(t) - b_b p \tilde{\xi}_t(t, y) - a_b p \tilde{\xi}(t, y) \\ \hat{\xi}_{yy}(t, L) = \hat{\xi}_{yyy}(t, L) = \hat{\xi}(t, 0) = 0, \quad \hat{\xi}_y(t, 0) = u(t) \end{aligned} \quad (53)$$

where $\tilde{\xi} = \hat{\xi} - \xi$, and $p > 0$ is chosen to ensure desirable convergence properties. Recall that $a_b = EI_b/m$ and $b_b = \eta EI_b/m$. Choose projection-based adaptive laws for $\hat{W}(t)$ and

²Poincaré's inequality $\int_0^L w^2 dx \leq L w^2(0) + \frac{4L^2}{\pi^2} \int_0^L w_x^2 dx$.

$\hat{\sigma}(t)$

$$\begin{aligned}\dot{\hat{W}}(t) &= \gamma_a \text{Proj} \left(\hat{W}(t), - \int_0^L (\tilde{\xi}_t + \delta \tilde{\xi}) \phi_b(y) dy \right) \\ \dot{\hat{\sigma}}(t) &= \gamma_a \text{Proj} \left(\hat{\sigma}(t), - \int_0^L (\tilde{\xi}_t + \delta \tilde{\xi}) dy \right)\end{aligned}\quad (54)$$

where $\gamma_a > 0$ is the adaptation rate, and the bounds on \hat{W} and $\hat{\sigma}$ are chosen to be equal to the known bounds on W and σ , respectively.

We are now ready to state our main result, which asserts that $\hat{\xi}$, which is the sum of the states of the two observer components, tracks ξ , i.e., the system state.

Theorem 4: The error between the system (46) and the perturbation observer (53), in the sense of $\|\tilde{\xi}(t, y)\|_{\mathcal{L}_2}$, is globally uniformly bounded, and the bound can be made arbitrarily small by increasing γ_a .

Proof: To streamline the proof, we introduce some useful notation. We define numbers $s_1, s_2, \delta_1, \delta_2$, which depend on the gain p , as follows:

$$\begin{aligned}s_1 &= \min \{(b_b p - \delta), \delta a_b p, \delta a_b\} \\ s_2 &= \frac{1}{2} \max \{1 + \delta, (a_b + \delta b_b), ((a_b + \delta b_b)p + \delta)\} \\ W^T W + \sigma^2 &\leq \frac{\delta_2}{4}, \quad |W^T \dot{W}| + |\sigma \dot{\sigma}| \leq \frac{\delta_1}{2}\end{aligned}\quad (55)$$

where $\delta > 0$ is an arbitrarily small constant, which is introduced in the proof. Equation (55) reflects the fact that $W(t), \sigma(t)$, their time derivatives, and predicted values are bounded with known bounds.

Consider the Lyapunov function

$$\begin{aligned}V(t) &= \frac{1}{2} \int_0^L \left(\tilde{\xi}_t^2 + (a_b + \delta b_b) \tilde{\xi}_{yy}^2 + (a_b + \delta b_b) p \tilde{\xi}^2 \right) dy \\ &\quad + \frac{1}{\gamma_a} \left(\tilde{W}^T \tilde{W} + \tilde{\sigma}^2 \right) + \delta \int_0^L \tilde{\xi} \tilde{\xi}_t dy\end{aligned}\quad (56)$$

where $\tilde{W} = \hat{W} - W$, and $\tilde{\sigma} = \hat{\sigma} - \sigma$. The constant δ is chosen to be small enough so that the Lyapunov function is positive definite. Differentiating both sides with respect to time and performing integration by parts a few times, we get

$$\begin{aligned}\dot{V}(t) &\leq -(b_b p - \delta) \int_0^L \tilde{\xi}_t^2 dy - \delta a_b p \int_0^L \tilde{\xi}^2 dy \\ &\quad - \delta a_b \int_0^L \tilde{\xi}_{yy}^2 dy - b_b \int_0^L \tilde{\xi}_{tyy}^2 dy \\ &\quad - \frac{1}{\gamma_a} \left(\tilde{W}(t)^T \dot{\tilde{W}}(t) + \tilde{\sigma}(t) \dot{\tilde{\sigma}}(t) \right).\end{aligned}\quad (57)$$

Define a constant $V_0 = \frac{\delta_2}{\gamma_a} + \frac{s_2 \delta_1}{s_1 \gamma_a}$. From (57), we get

$$\dot{V}(t) \leq -\frac{s_1}{s_2} V(t) + \frac{\delta_1}{\gamma_a} + \frac{s_1 \delta_2}{s_2 \gamma_a} = -\frac{s_1}{s_2} (V(t) - V_0). \quad (58)$$

It follows that $V(t)$ converges to V_0 exponentially fast. Thus, the error dynamics between the perturbation observer and the

actual system are globally uniformly bounded, and the bound reduces uniformly with increasing γ_a . ■

The two halves of the observer, put together, thus function as a standard perturbation observer whose job is to estimate the unknown nonlinearities and disturbances using full state feedback. In standard adaptive control methodologies, a control law is first designed assuming a complete knowledge of the system. Thereafter, the unknown system parameters, which appear in the control law, are replaced by estimated values that are supplied by the adaptation law.

In contrast, we decompose the original system into a “particular” and a “homogeneous” half, whose states are predicted by the two components that are described briefly; thereafter, a controller is designed for the homogeneous half *alone* so that its output tracks the difference between the system output and the output of the particular component. The homogeneous half is a linear time-invariant system with desirable convergence properties, and a feed-forward tracking control law can be readily designed for it.

Recall that the output of interest is $\int_0^L \xi_y(t, y) dy = \xi(t, L)$, from (7). It represents the integrated value of the wing dihedral which, in turn, is a measure of the side force produced by the wing. In order to ensure that this output tracks the desired reference signal $R(t)$, the control signal $u(t)$ [also = $\hat{\xi}_{h,y}(t, 0)$] is designed using trajectory planning to ensure that $\hat{\xi}_h(t, L)$ tracks $R(t) - \hat{\xi}_p(t, L)$. In particular, $\hat{\xi}_h$ is approximated via a polynomial expansion that involves powers of y , and the coefficients are solved using the PDE and the boundary conditions.

Remark 8: The observer-based approach that is presented here can be used for a wide class of functions $F(t, y)$ which, as we argued earlier, are usually nonlinear in ξ_y . Therefore, it is difficult to construct a polynomial expansion for $F(t, y)$. Although trajectory planning involves a polynomial expansion, it is only done for the homogeneous half, and consequently, there is no need to obtain a polynomial expansion for $F(t, y)$.

Remark 9: The error between the perturbation observer and the system is uniformly bounded, and the bound can be made arbitrarily small by increasing γ_a . The trajectory planning approach creates a low-pass-filtered control signal, as shown in the next section, and therefore, the stability and the robustness of the system are not affected if a large value is chosen for γ_a .

Remark 10: One limitation of using a perturbation observer in the present form is that it requires a knowledge of $\xi(t)$. However, $\xi(t)$ can be obtained using an array of sensors and spline fitting. Such an array of sensors is light and cheap enough to implement in a practical setting, and more so compared with a distributed actuation scheme.

D. Trajectory Planning for the Homogeneous Component of the Observer ($\hat{\xi}_h$)

For a reference signal $R(t)$ from (7), let $R_h(t) = R(t) - \hat{\xi}_p(t, L)$ denote the reference signal that has to be tracked by $\hat{\xi}_h(t, L)$, as shown in Fig. 4. It may be possible to use more than one method to design a control signal $u(t)$, which ensures that the output of the homogeneous half tracks the reference signal. This freedom results largely from the fact that the homogeneous

component is an exponentially stable linear time-invariant system with desirable convergence properties (by design). In this section, we illustrate a trajectory-planning approach, as we did for wing twist.

The term $\hat{\xi}_h(t, y)$ can be approximated by a polynomial of the form

$$\hat{\xi}_h(t, y) = \sum_{j=1}^N \frac{\eta_j(t) y^j}{j!} \quad (59)$$

where N needs to be chosen to ensure desirable tracking properties. Note that the coefficient of y^0 is zero because $\hat{\xi}(t, 0) = 0$.

Substituting (59) into the $\hat{\xi}_h$ dynamics in (52) yields the set of ODEs

$$\ddot{\eta}_j + b_b p \dot{\eta}_j + a_b p \eta_j = -b_b \dot{\eta}_{j+4} - a_b \eta_{j+4}. \quad (60)$$

The boundary conditions, together with $\hat{\xi}_h(t, L) = R_h(t)$, yield the following algebraic equations:

$$\begin{aligned} \sum_{j=0}^{N-2} \frac{\eta_{j+2}(t) L^j}{j!} &= 0, \quad \sum_{j=0}^{N-3} \frac{\eta_{j+3}(t) L^j}{j!} = 0 \\ \sum_{j=1}^N \frac{\eta_j(t) L^j}{j!} &= R_h(t). \end{aligned} \quad (61)$$

The value of N can be chosen to ensure good tracking. Note that the $\hat{\xi}_h$ dynamics are of fourth order in y . Therefore, we need to choose $N > 5$, and the gain p must be chosen to ensure stability of the resulting set of ODEs. For any choice of N , we have $N - 4$ differential equations (for η_1 to η_{N-4}) and 3 constraints, a total of $N - 1$ equations. The underdetermined problem may be resolved by setting one variable among η_{N-3} , η_{N-2} , and η_{N-1} to zero, or imposing an additional constraint on the system.

Suppose that we set $N = 5$, i.e., $\eta_6 = \eta_7 = \dots = 0$. We also set $\eta_4(t) = 0$.³ This yields the differential equation

$$\ddot{\eta}_1(t) + b_b p \dot{\eta}_1(t) + a_b p \eta_1(t) + b_b \dot{\eta}_5(t) + a_b \eta_5(t) = 0. \quad (62)$$

Constraint (61) can be solved to obtain $\eta_5(t)$ in terms of $\eta_1(t)$ and $R_h(t)$

$$\eta_5(t) = \frac{12}{L^4} \left(-\eta_1(t) + \frac{R_h(t)}{L} \right). \quad (63)$$

From (59), it follows that the main bending control input is given by

$$u(t) = \hat{\xi}_{h,y}(t, 0) = \eta_1(t) \quad (64)$$

where $\eta_1(t)$ is obtained by integrating the following ODE, obtained in turn by substituting (63) into (62):

$$\begin{aligned} \ddot{\eta}_1(t) + b_b \left(p - \frac{12}{L^4} \right) \dot{\eta}_1(t) + a_b \left(p - \frac{12}{L^4} \right) \eta_1(t) \\ = - \left(\frac{12}{L^5} \right) (b_b \dot{R}_h(t) + a_b R_h(t)). \end{aligned} \quad (65)$$

³Motivation: if R_h is a constant, then $\eta_4 = 0$ is in the steady-state solution. Therefore, this approximation works, at least, for a class of slow time-varying signals.

Note that the gain p has to be chosen so that $p > 12/L^4$ for $\eta_5(t)$ to be stable. This completes the design of a trajectory planning-based tracking controller for bending.

VI. SIMULATIONS

Simulations are carried out in MATLAB by using a Galerkin-based approach to convert the PDE system into ODEs. The Galerkin truncation is not used as a basis for control law design; therefore, no danger of “spillover instability” arises. The twist $\theta(t, y)$ is expressed as a weighted sum of basis functions $\phi_i(y)$, $i = 1, 2, \dots, n$ and $\psi(y)$

$$\begin{aligned} \theta(t, y) &= s(t)\psi(y) + \sum_{i=1}^n \eta_i(t)\phi_i(y) \\ \phi_i(0) &= \phi'_i(L) = 0 \end{aligned} \quad (66)$$

where $s(t)$ is the boundary control input. If boundary control is applied at the wing root, then $\psi(y)$ has to be chosen to satisfy $\psi'(L) = 0$ and $\psi(0) = 1$. On the other hand, if the boundary control is applied at the wing tip, we choose ψ to satisfy $\psi(0) = 0$ and $\psi'(L) = 1$.

The PDE in (32) can be rewritten as

$$\begin{aligned} \psi(y)\ddot{s}(t) + \sum_{i=1}^n \ddot{\eta}_i(t)\phi_i(y) - \sum_{i=1}^n \phi''_i(y) (b\dot{\eta}_i(t) + a\eta_i(t)) \\ - \psi''(y)(b\dot{s} + as) \\ = M \left(\psi(y)s + \sum_{i=1}^n \eta_i(t)\phi_i(y) \right). \end{aligned} \quad (67)$$

Using Galerkin’s method, (67) is converted to a set of ODEs

$$\begin{aligned} \mathbf{c}(\ddot{s}(t) - Ms(t)) + \mathbf{d}(b\dot{s} + as(t)) \\ + [A](\ddot{\eta}(t) - M\eta(t)) + [B](b\dot{\eta}(t) + a\eta(t)) = 0 \end{aligned} \quad (68)$$

where

$$\begin{aligned} \mathbf{c} &= \int_0^L \psi(y)\phi(y)dy, \quad \mathbf{d} = - \int_0^L \psi''(y)\phi(y)dy \\ [A] &= \int_0^L \phi\phi^T dy, \quad [B] = - \int_0^L \phi(\phi'')^T dy. \end{aligned} \quad (69)$$

The reader will recall that ψ is a scalar, and $\phi = [\phi_1, \phi_2, \dots, \phi_n]^T$ is a vector. The control $s(t)$ is expressed similarly in terms of ϕ , ψ , and η to obtain a set of ODEs, which are simulated to approximate the response of the system.

A. Root Control of Wing Twist

Fig. 5 demonstrates the regulation of twist dynamics using the backstepping controller that is derived in (31), with the transformation in (12) and (17). The value of M/a was set to 8, where $a = G\tilde{J}/I_p$. A value of $p = 4$ yielded an unstable response, while the response was stable for $p = 8$. Recall the following condition for stability with $L = 1$: $p > M/a - \pi^2/4 \approx 5.5$. The backstepping controller works even when $M(y) = M(1 - y^2)$ is used (to mimic an elliptical lift distribution over the wing) instead of a constant $M(y) \equiv M$.

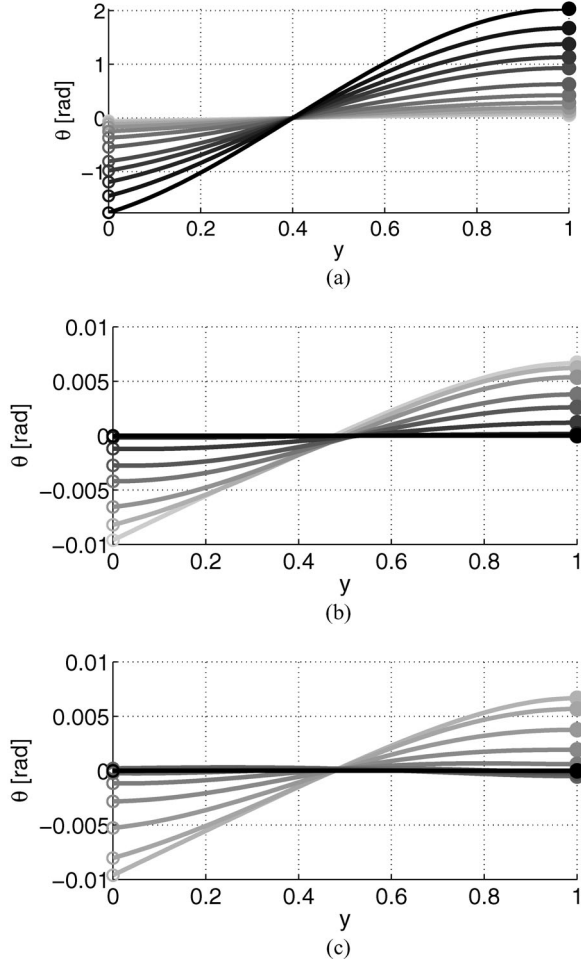


Fig. 5. Regulation of the twist dynamics using the backstepping controller in (31). The plots were obtained for $M/a = 8$, while p was increased to ensure stability. Each plot is a collection of appropriately chosen snapshots in the interval $0 < t < 30$ s, with the lines getting darker with time. In plots (b) and (c), $\theta(t, y)$ converges to zero exponentially. (a) Unstable response with $p = 4$. (b) Stable response with $p = 8$. (c) Stable response with $p = 8$ for spatially varying $M(y)$.

The backstepping controller can be added on top of a tracking controller.

Each plot in Fig. 5 is a collection of snapshots that are appropriately chosen in the interval $0 < t < 30$ s, with the lines getting darker with time. The system state $\theta(t, y)$ converges to zero exponentially when $p = 8$.

B. Tip Control of Wing Twist

Fig. 6 shows simulation results for the twist dynamics, when the actuator is located at the wing tip. The value of M/a was chosen so that stability is assured without the need for a dedicated stabilizing controller. The first plot was obtained for a system, where the aerodynamics were assumed to be linear but unknown. The second plot was assumed linear unknown aerodynamics such that the system was unstable in the open loop, but within the enhanced stability margin that is described in Section IV-B. The third plot (bottom row) was obtained for the case where the aerodynamics were additionally spatially vary-

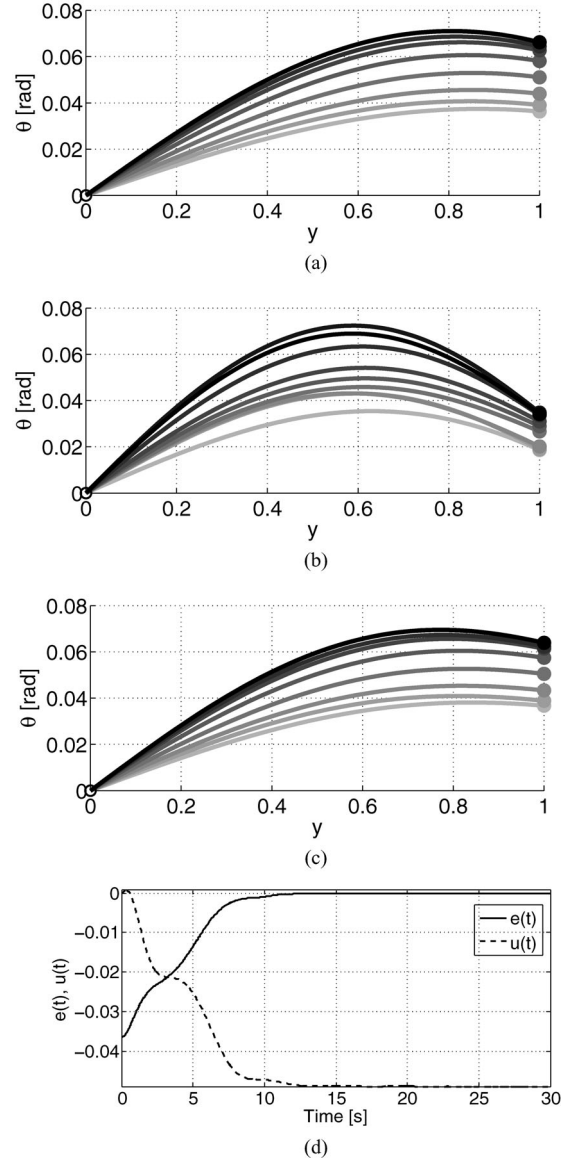


Fig. 6. Twist profile of the wing as a function of time when the adaptive controller in (41) is applied at the wing tip. Three cases have been examined here, with $\int_0^L \theta(t, y) dy = 0.05$ as the desired output. The first three plots are appropriately chosen snapshots in the interval $0 < t < 30$ s, with lines getting darker with time. The error metric $e(t)$ converges to zero exponentially. (a) M unknown, constant, open loop stable. (b) Unknown M , constant, open loop unstable. (c) Spatially varying, unknown $M(y)$, unstable dynamics. (d) Time history of $e(t)$, $u(t)$.

ing. The fourth plot depicts the time histories of the tracking error $e(t)$ and the control signal $u(t)$, respectively. In all cases, the twist amplitude converges to the steady-state value with satisfactory transients. The error metric (5) converges to zero exponentially.

C. Comparison of Finite-State Approximation-Based and Trajectory Planning-Based Controllers for Bending

Using Galerkin's method, the beam bending dynamics (46), with the control input $u(t)$ and its derivative $\dot{u}(t)$ as additional

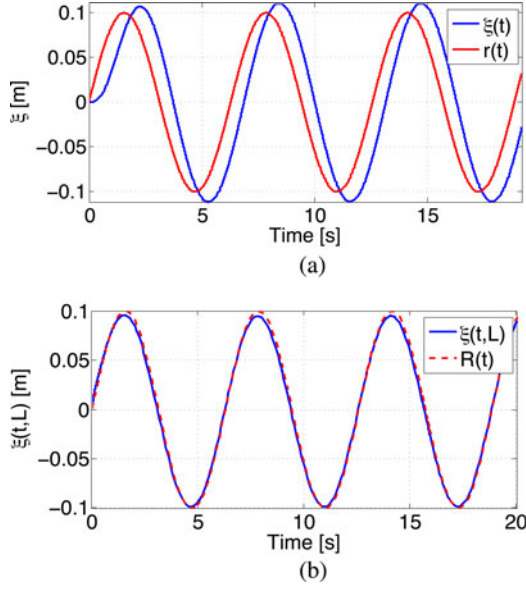


Fig. 7. Comparison of controllers derived from finite-state approximations of the open loop and the homogeneous component, respectively, with a controller obtained using trajectory planning [41]. (a) Traditional ODE control. (b) PDE perturbation observer with trajectory planning.

states, can be recast into the form

$$\dot{x} = Ax + B\bar{u} + f(x), y = Cx \quad (70)$$

where $\bar{u}(t)$ equals the highest derivative of $u(t)$, i.e., $\ddot{u}(t) = \bar{u}(t)$. The system can be stabilized if (A, B) is stabilizable. In particular, vectors B and C depend strongly on the choice of the basis functions. The unmatched nonlinearity $f(x)$ can affect the tracking error as well as the stability of the closed-loop system if not compensated adequately. The unmatched nonlinearity can be tackled using backstepping, or a more direct approach such as in [23, Ch. 3, pp. 140–174].

Fig. 7 compares the performance of two controllers. The first is based on [23] and designed using a finite-state approximation of the beam, and the other is based on the perturbation observer and trajectory planning approach in Section V. The beam is assumed to be loaded uniformly, but for the purpose of control design, this load is treated as an unknown. This simple loading condition is enough to create an unmatched uncertainty in the finite-state approximation.

Fig. 7(a) shows the performance of a controller, which is designed using the finite-state approximation. The tracking error is less than 5% of the signal amplitude, and there is a phase lag in the system output when compared with the reference signal. The tracking error as well as the phase lag arises due to the use of a low-pass filter in the generation of the control signal. On the other hand, Fig. 7(b) [41] shows the tracking performance of the proposed controller which is derived from trajectory planning using a seventh degree polynomial and the perturbation observer in Section V-C. The amplitude of the tracking error is considerably smaller than the previous approach, and the phase lag is almost eliminated. For the system that is considered in this illustration, the proposed controller outperforms the conventional ODE-based controller. Note that the trajectory planning-based

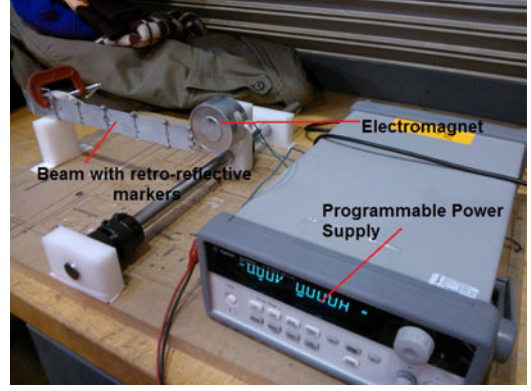


Fig. 8. Experimental setup showing the beam and power supply.

control signal, which is generated using (62) and (64), is itself a low-pass filter, albeit one that ensures, by design, a small tracking error.

VII. EXPERIMENTAL RESULTS

In this section, we describe some successful experiments, which were performed to validate the efficacy of the perturbation observer-based controller in Section V. Fig. 8 shows the experimental setup. A long thin beam with a rectangular cross section is utilized for experiments. It is rigidly clamped at one end, while the other end is free to be controlled. Two small permanent magnets attached to the tip are acted on by an electromagnet whose magnetic field can be controlled by specifying a current and varying the voltage using a programmable power supply (Agilent Technologies E3642A) that interfaces with MATLAB. The interaction between the permanent magnets and the magnetic field of the electromagnet produces a force that acts on the beam tip.

Retroreflective markers are placed at seven specific points along the length of the beam, and the VICON motion capture system is used to track the coordinates of those markers. Bending displacement is determined by calculating the distance between the markers on the beam in the deformed state, and the coordinates of the corresponding markers in the undeformed state. The bending displacement is interpolated from the data that are obtained from the VICON system to obtain the deformation profile. This information is used to calculate the tip force, which is the control variable.

The electromagnet is characterized to determine a relationship between the required voltage and the commanded tip force. The tip deflection ξ_{tip} of a cantilever beam as a function of the applied tip force, $F_{\text{tip}} (= EI_b \xi_{yyy}(t, L))$, is given by

$$\xi_{\text{tip}} \triangleq \xi(t, L) = \frac{F_{\text{tip}} L^3}{3EI_b} \implies u(t) = \xi_{yyy}(t, L) = \frac{3\xi_{\text{tip}}}{L^3}. \quad (71)$$

The electromagnet is calibrated by measuring the steady-state tip deflection as a function of the input voltage so that

$$\xi_{\text{tip}} \approx 1.33 \times 10^{-3} W^{1.5} \quad (72)$$

where W denotes the voltage of the signal, which is sent to the electromagnet. Combining (71) and (72) with the fact that the

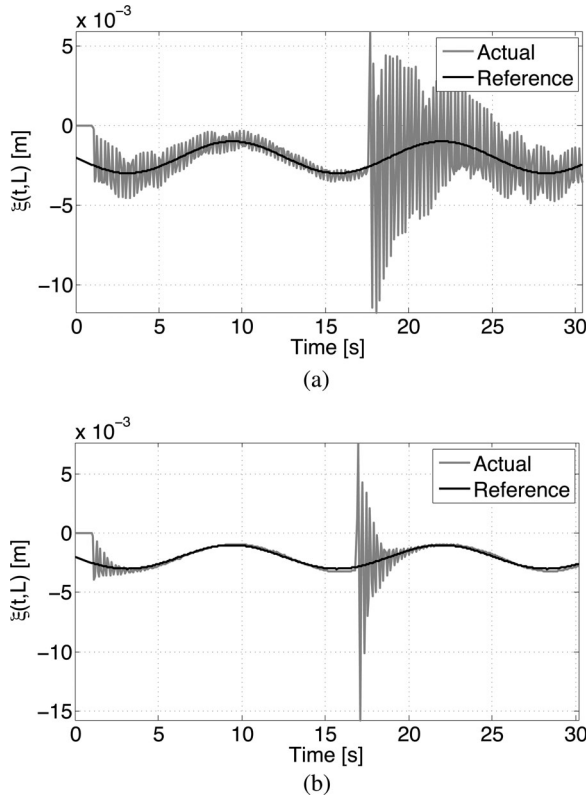


Fig. 9. Time histories of the tip displacement ($\xi(t, L)$), when a sinusoidal reference signal was sent to the system. An impulse-like disturbance was also administered to the beam. The controller was disabled in the first case to provide a comparison between the open- and closed-loop systems. (a) Open loop with an impulse perturbation. (b) PDE boundary control with impulse perturbation.

control input $u(t) = \xi_{yyy}(t, L) = F_{\text{tip}}/EI_b$ results in

$$u(t) = \frac{4 \times 10^{-3}}{L^3} W^{1.5} \implies W = 39.67L(u(t))^{2/3}. \quad (73)$$

The control law $u(t)$ is obtained from an equation, which is analogous to (64) [19]

$$\begin{aligned} u(t) &= \frac{5\eta_2(t)}{L} - \frac{18R_h(t)}{L^3}, \quad R_h(t) = R(t) - \hat{\xi}_p(t, L) \\ \ddot{\eta}_2(t) &+ \left(p + \frac{60}{L^4}\right) (b_b \dot{\eta}_2(t) + a_b \eta_2(t)) \\ &= \frac{180}{L^6} (b_b \dot{R}_h(t) + a_b R_h(t)). \end{aligned} \quad (74)$$

The gain was set to $p = 500$ for the experiments. Fig. 9 shows the time history of the tip displacement for two cases. In both cases, the system was given an impulsive disturbance midway through the experiments at $t = 17$ s, in addition to persistent external disturbances in form of a mild breeze in the experimental area. The open-loop response is noisy due to the persistent external disturbances. The amplitude takes a very long time to converge after the impulsive perturbation at 17 s. In comparison, the closed-loop response shows a negligible tracking error and rapid convergence to the reference signal after the impulsive perturbation. Additional experimental results, including those for root control of beam bending, can be found in [19] and [42].

VIII. CONCLUSION

This paper has introduced a boundary control formulation for a class of PDEs whose output consists of a spatial integral of the state variable. Although the primary focus of this paper was on the control of flexible wings, this boundary control problem is directly relevant to the control of flexible continuum robotic arms described by PDEs.

In order to control wing twist using a root-based actuator, a tracking controller, which was based on PDE backstepping was designed to handle the output that has an infinite relative degree with respect to the root actuation. On the other hand, when twisting moment at the wing tip was the control input, it was shown that the system had a relative degree of 2 with respect to the input–output combination, which facilitated the design of a robust adaptive tracking controller. It was shown that the tracking controller alone could yield a 16-fold improvement in the stability margin of the system.

The force distribution that drives bending is far too complicated to be handled by backstepping alone, which motivated the development of a new perturbation-observer-based approach that is presented in Section V. The two-stage-observer-based tracking controller was designed to ensure that the wing tip tracked the desired reference profile with the bending PDE. The first component of the observer compensated for the nonlinearities and unmodeled dynamics, while the other was used exclusively for deriving the control signal. The proposed perturbation-observer-based controller was implemented in an experimental setup, which allowed us to control the bending displacement of the tip of a beam by applying a force at the wing tip. The controller performed as expected, and demonstrated reference signal tracking as well as disturbance rejection.

ACKNOWLEDGMENT

The authors would like to thank Prof. H. Hilton and Prof. L. Bergman at UIUC for the stimulating discussions from which this paper benefitted. The authors thank the anonymous reviewers for their constructive criticism and helpful comments.

REFERENCES

- [1] M. Abdulrahim, H. Garcia, and R. Lind, "Flight characteristics of shaping the membrane wing of a micro air vehicle," *J. Aircraft*, vol. 42, no. 1, pp. 131–137, 2005.
- [2] M. J. Balas, "Feedback control of flexible systems," *IEEE Trans. Autom. Control*, vol. 23, no. 4, pp. 673–679, Aug. 1978.
- [3] S. Bieniawski and I. M. Kroo, "Flutter suppression using micro-trailing edge effectors," presented at the 44th AIAA/ASME/ASCE/AHS Structures, Structural Dyn., Materials Conf., Norfolk, VA, USA, 2003, AIAA Paper 2003-1941.
- [4] F. Bucci and I. Lasiecka, "Optimal boundary control with critical penalization for a PDE model of fluid–solid interactions," *Calculus Variat.*, vol. 37, pp. 217–235, 2009.
- [5] C. Byrnes, I. Lauko, D. Gilliam, and V. Shubov, "Output regulation for linear distributed parameter systems," *IEEE Trans. Autom. Control*, vol. 45, no. 12, pp. 2236–2252, Dec. 2000.
- [6] Z. Cai, M. S. de Queiroz, and D. M. Dawson, "A sufficiently smooth projection operator," *IEEE Trans. Autom. Control*, vol. 51, no. 1, pp. 135–139, Jan. 2006.
- [7] A. Cheng and K. Morris, "Well-posedness of boundary control systems," *SIAM J. Contr. Optim.*, vol. 42, no. 4, pp. 1244–1265, 2003.
- [8] P. D. Christofides and P. Daoutidis, "Feedback control of hyperbolic PDE systems," *AIChE J.*, vol. 42, no. 11, pp. 3063–3086, 1996.

- [9] P. D. Christofides and P. Daoutidis, "Finite-dimensional control of parabolic PDE systems using approximate inertial manifolds," in *Proc. 36th IEEE Conf. Dec. Control*, San Diego, CA, USA, Dec. 1997, vol. 2, pp. 1068–1073.
- [10] S.-J. Chung and M. Dorothy, "Neurobiologically inspired control of engineered flapping flight," *J. Guidance, Contr. Dynam.*, vol. 33, no. 2, pp. 440–453, 2010.
- [11] R. F. Curtain and H. J. Zwart, *An Introduction to Infinite-Dimensional Linear Systems Theory*, (Texts in Applied Mathematics, vol. 21). New York, NY, USA: Springer-Verlag, 1995.
- [12] R. Curtain and K. Morris, "Transfer functions of distributed parameter systems: A tutorial," *Automatica*, vol. 45, pp. 1101–1116, 2009.
- [13] X. Deng, L. Schenato, and S. S. Sastry, "Flapping flight for biomimetic robotic insects: Part II. Flight control design," *IEEE Trans. Robot.*, vol. 22, no. 4, pp. 789–803, Aug. 2006.
- [14] X. Deng, L. Schenato, W. C. Wu, and S. S. Sastry, "Flapping flight for biomimetic robotic insects: Part I. System modeling," *IEEE Trans. Robot.*, vol. 22, no. 4, pp. 776–788, Aug. 2006.
- [15] D. B. Doman, C. P. Tang, and S. Regisford, "Modeling interactions between flexible flapping-wing spars, mechanisms, and drive motors," *J. Guidance Contr. Dynam.*, vol. 34, no. 5, pp. 1457–1473, 2011.
- [16] M. Dorothy, A. A. Paranjape, P. D. Kuang, and S.-J. Chung, "Towards bio-inspired robotic aircraft: Control experiments on flapping and gliding flight," J. Valasek, Ed., in *Advances in Intelligent and Autonomous Aerospace Systems*, Progress in Astronautics and Aeronautics. Reston, VA, USA: Amer. Inst. Aeronaut. Astronaut., 2012.
- [17] M. P. Fard and S. I. Sagatun, "Exponential stabilization of a transversely vibrating beam by boundary control via Lyapunov's direct method," *J. Dyn. Syst. Meas. Control*, vol. 123, pp. 195–200, 2001.
- [18] M. Goman and A. Khrabrov, "State-space representation of aerodynamic characteristics of an aircraft at high angles of attack," *J. Aircraft*, vol. 31, no. 5, pp. 1109–1115, 1994.
- [19] J. Guan, "Design and control strategy of a flexible, hyper-redundant robotic arm using electroactive dielectric polymers," M.S. thesis, Dept. Aerospace Eng., Univ. Illinois at Urbana-Champaign, Urbana, IL, USA, 2012.
- [20] M. Hamamoto, Y. Ohta, K. Hara, and T. Hisada, "A fundamental study of wing actuation for a 6-in-wingspan flapping microaerial vehicle," *IEEE Trans. Robot.*, vol. 26, no. 2, pp. 244–255, Apr. 2010.
- [21] W. He, S. S. Ge, B. V. E. How, Y. S. Choo, and K. S. Hong, "Robust adaptive boundary control of a flexible marine riser with vessel dynamics," *Automatica*, vol. 47, pp. 722–732, 2011.
- [22] D. H. Hodges and A. G. Pierce, *Introduction to Structural Dynamics and Aeroelasticity* (Cambridge Aerospace Series, vol. 15). Cambridge, U.K.: Cambridge Univ. Press, 2002.
- [23] N. Hovakimyan and C. Cao, *LI Adaptive Control Theory: Guaranteed Robustness with Fast Adaptation* (Advances in Design and Control). Philadelphia, PA, USA: SIAM, 2010.
- [24] N. Hovakimyan, E. Lavretsky, and A. Sasane, "Dynamic inversion for nonaffine-in-control systems via time-scale separation. Part I," *J. Dyn. Control Syst.*, vol. 13, no. 4, pp. 451–465, 2007.
- [25] S. A. Hubbard, D. M. McFarland, L. A. Bergman, and A. F. Vakakis, "Targeted energy transfer between a model flexible wing and nonlinear energy sink," *J. Aircraft*, vol. 47, no. 6, pp. 1918–1931, 2010.
- [26] P. G. Ifju, D. A. Jenkins, S. Ettinger, L. Yongsheng, W. Shyy, and M. R. Waszak, "Flexible-wing-based micro air vehicles," presented at the AIAA Aerospace Sci. Meeting Exhibit., Reno, NV, USA, 2002, AIAA Paper 2002-0705.
- [27] A. Isidori and C. I. Byrnes, "Output regulation of nonlinear systems," *IEEE Trans. Autom. Control*, vol. 35, no. 2, pp. 131–140, Feb. 1990.
- [28] M. Krstic, B.-Z. Guo, A. Balogh, and A. Smyshlyaev, "Control of a tip-force destabilized shear beam by observer-based boundary feedback," *SIAM J. Control Optim.*, vol. 47, no. 2, pp. 553–574, 2008.
- [29] M. Krstic, I. Kanellakopoulos, and P. V. Kokotovic, *Nonlinear and Adaptive Control Design*. New York, NY, USA: Wiley, 1995.
- [30] M. Krstic and A. Smyshlyaev, *Boundary Control of PDEs: A Course on Backstepping Design*, (Advances in Design and Control). Philadelphia, PA, USA: SIAM, 2008.
- [31] M. Krstic and A. Smyshlyaev, *Adaptive Control of PDEs*. Princeton, NJ, USA: Princeton Univ. Press, 2010.
- [32] W. Lohmiller and J. J. E. Slotine, "Contraction analysis of nonlinear distributed systems," *Int. J. Contr.*, vol. 78, no. 9, pp. 678–688, 2005.
- [33] Z. Luo, "Direct strain feedback control of flexible robot arms: New theoretical and experimental results," *IEEE Trans. Autom. Control*, vol. 38, no. 11, pp. 1610–1622, Nov. 1993.
- [34] Z. Luo and B. Guo, "Further theoretical results on direct strain feedback control of flexible robot arms," *IEEE Trans. Autom. Control*, vol. 40, no. 4, pp. 747–751, Apr. 1995.
- [35] R. Marino and P. Tomei, "Robust adaptive state feedback tracking for nonlinear systems," *IEEE Trans. Autom. Control*, vol. 43, no. 1, pp. 84–89, Jan. 1998.
- [36] B. W. McCormick, *Aerodynamics, Aeronautics and Flight Mechanics*, 2nd ed. New York, NY, USA: Wiley, 1994.
- [37] L. Meirovitch and H. Baruh, "On the problem of observation spillover in self-adjoint distributed-parameter systems," *J. Optim. Appl.*, vol. 39, no. 2, pp. 269–291, 1983.
- [38] A. Paranjape, S.-J. Chung, and M. Krstic, "PDE boundary control for flexible articulated aircraft wings," presented at the AIAA Guidance Navigat. Contr. Conf. Portland, OR, USA, 2011, AIAA Paper 2011-6486.
- [39] A. A. Paranjape, S.-J. Chung, H. H. Hilton, and A. Chakravarthy, "Dynamics and performance of tailless micro aerial vehicle with flexible articulated wings," *AIAA J.*, vol. 50, no. 5, pp. 1177–1188, 2012.
- [40] A. A. Paranjape, S.-J. Chung, and M. S. Selig, "Flight mechanics of a tailless articulated wing aircraft," *Bioinspirat. Biomimet.*, vol. 6, no. 2, p. 026005, 2011.
- [41] A. A. Paranjape, "Dynamics and control of robotic aircraft with articulated wings," Ph.D. dissertation, Dept. Aerosp. Eng., Univ. Illinois Urbana-Champaign, Urbana, IL, USA, Dec. 2011.
- [42] A. A. Paranjape, J. Guan, S.-J. Chung, and M. Krstic, "PDE boundary control for Euler–Bernoulli beam using a two stage perturbation observer," presented at the 51st IEEE Conf. Dec. Control, Maui, HI, USA, 2012.
- [43] A. A. Paranjape, J. Kim, and S.-J. Chung, "Novel dihedral-based control of flapping-wing aircraft with application to perching," *IEEE Trans. Robot.*, 2013, submitted.
- [44] M. D. Queiroz, D. M. Dawson, M. Agarwal, and F. Zhang, "Adaptive nonlinear boundary control of a flexible link robotic arm," *IEEE Trans. Robot. Autom.*, vol. 15, no. 4, pp. 779–787, Aug. 1999.
- [45] P. K. Raghavendra, T. Sahai, P. A. Kumar, M. Chauhan, and N. Ananthkrishnan, "Aircraft spin recovery, with and without thrust vectoring, using nonlinear dynamic inversion," *J. Aircraft*, vol. 42, no. 6, pp. 1492–1503, 2005.
- [46] M. Rais-Rohani, R. T. Haftka, B. Grossman, and E. R. Unger, "Integrated aerodynamic-structural-control wing design," *Comput. Syst. Eng.*, vol. 3, no. 6, pp. 639–650, 1992.
- [47] D. L. Russell, "Controllability and stabilizability theory for linear partial differential equations: Recent progress and open questions," *SIAM Rev.*, vol. 20, no. 4, pp. 639–739, 1978.
- [48] D. Salamon, "Realization theory in hilbert space," *Math. Syst. Theor.*, vol. 21, pp. 147–164, 1989.
- [49] H. Sano, "Output tracking control of a parallel-flow heat exchange process," *Syst. Control Lett.*, vol. 60, no. 11, pp. 917–921, 2011.
- [50] W. Shyy, H. Aono, S. K. Chimakurthi, P. Trizila, C.-K. Kang, C. E. S. Cesnik, and H. Liu, "Recent progress in flapping wing aerodynamics and aeroelasticity," *Progr. Aerosp. Sci.*, vol. 46, pp. 284–327, 2010.
- [51] A. A. Siranosian, M. Krstic, A. Smyshlyaev, and M. Bememt, "Motion planning and tracking for tip displacement and deflection angle for flexible beams," *J. Dyn. Syst. Meas. Control*, vol. 131, p. 031009, 2009.
- [52] A. A. Siranosian, M. Krstic, A. Smyshlyaev, and M. Bememt, "Gain scheduling-inspired boundary control for nonlinear partial differential equations," *J. Dyn. Syst. Meas. Control*, vol. 133, p. 051007, 2011.
- [53] S. A. Snell, D. F. Enns, and W. L. Garrard Jr., "Nonlinear inversion flight control for a supermaneuverable aircraft," *J. Guidance Control Dyn.*, vol. 15, no. 4, pp. 976–984, 1992.
- [54] A. Song, X. D. Tian, E. Israeli, R. Galvao, K. Bishop, S. Swartz, and K. Breuer, "Aeromechanics of membrane wings with implications for animal flight," *AIAA J.*, vol. 46, no. 8, pp. 2096–2106, 2008.
- [55] D. T. Tran and R. Lind, "Parameterizing stability derivatives and flight dynamics with wing deformation," presented at the AIAA Atmospheric Flight Mech. Conf. Toronto, ON, Canada, 2010, AIAA Paper 2010-8227.
- [56] M. W. Vandegrift, F. L. Lewis, and S. Q. Zhu, "Flexible-link robot arm control by a feedback linearization/singular perturbation approach," *J. Robot. Syst.*, vol. 11, no. 7, pp. 591–603, 1994.
- [57] R. Vazquez and M. Krstic, "Explicit integral operator feedback for local stabilization of nonlinear thermal convection loop PDEs," *Syst. Contr. Lett.*, vol. 55, pp. 624–632, 2006.
- [58] R. Vazquez and M. Krstic, "A closed-form feedback controller for stabilization of the linearized 2-D Navier–Stokes Poiseuille system," *IEEE Trans. Autom. Control*, vol. 52, no. 12, pp. 2298–2312, Dec. 2007.
- [59] Q. Wang and R. F. Stengel, "Robust nonlinear flight control of a high-performance aircraft," *IEEE Trans. Contr. Syst. Technol.*, vol. 13, no. 1, pp. 15–26, Jan. 2005.
- [60] R. J. Wood, "The first takeoff of a biologically inspired at-scale robotic insect," *IEEE Trans. Robot.*, vol. 24, no. 2, pp. 341–347, Apr. 2008.



Aditya A. Paranjape (M'12) received the B.Tech. and M.Tech. degrees from the Indian Institute of Technology Bombay, Mumbai, India, in 2007 and the Ph.D. degree from the University of Illinois at Urbana-Champaign (UIUC), Urbana, IL, USA, in 2011, all of them in aerospace engineering.

He is currently a Postdoctoral Research Associate with the Department of Aerospace Engineering, UIUC. His research interests include nonlinear dynamics and control and multiagent systems.



Jinyu Guan received the Bachelor's degree in mechanical engineering from the University of Florida, Gainesville, FL, USA, in 2010, and the Master's degree in aerospace engineering from the University of Illinois at Urbana-Champaign, Urbana, IL, USA, in 2012.

He is currently a Guidance, Navigation, and Control Systems Engineer with the Lockheed Martin Corporation, Orlando, FL, USA.



Soon-Jo Chung (M'06–SM'12) received the B.S. degree (*summa cum laude*) from the Korea Advanced Institute of Science and Technology, Daejeon, Korea, in 1998 and the S.M. degree in aeronautics and astronautics and the Sc.D. degree in estimation and control from the Massachusetts Institute of Technology, Cambridge, MA, USA, in 2002 and 2007, respectively.

He is currently an Assistant Professor with the Department of Aerospace Engineering and the Coordinated Science Laboratory, University of Illinois at

Urbana-Champaign, Urbana, IL, USA. His research interests include nonlinear control theory, aerial robotics, bioinspired flight, flight controls, spacecraft formation flying, and estimation theory for vision-based navigation.

Prof. Chung is a senior member of the American Institute of Aeronautics and Astronautics (AIAA). He received an Air Force Office of Scientific Research Young Investigator Award, a National Science Foundation CAREER Award, National Aeronautics and Space Administration Jet Propulsion Laboratory Summer Faculty Fellowships, and two best paper awards from the IEEE and the AIAA.



Miroslav Krstic (S'92–M'95–SM'99–F'02) received the Ph.D. degree from the University of California (UC), Santa Barbara, CA, USA, in 1994.

He was an Assistant Professor with the University of Maryland, College Park, MD, USA, until 1997. He is the Daniel L. Alspach Professor and founding Director of the Cymer Center for Control Systems and Dynamics at UC San Diego, La Jolla, CA, USA. He has held the appointment of Springer Distinguished Visiting Professor of Mechanical Engineering at UC Berkeley. He is a co-author of nine books: *Nonlinear and Adaptive Control Design* (Wiley, 1995), *Stabilization of Nonlinear Uncertain Systems* (Springer, 1998), *Flow Control by Feedback* (Springer, 2002), *Real-Time Optimization by Extremum Seeking Control* (Wiley, 2003), *Control of Turbulent and Magnetohydrodynamic Channel Flows* (Birkhauser, 2007), *Boundary Control of PDEs: A Course on Backstepping Designs* (SIAM, 2008), *Delay Compensation for Nonlinear, Adaptive, and PDE Systems* (Birkhauser, 2009), *Adaptive Control of Parabolic PDEs* (Princeton Univ. Press, 2009), and *Stochastic Averaging and Stochastic Extremum Seeking* (Springer, 2012).

Dr. Krstic is a Fellow of the International Federation of Automatic Control and has received the Axelby and Schuck Paper Prizes, and the National Science Foundation Career, Office of Naval Research Young Investigator, and Presidential Early Career Award for Scientists and Engineers Awards.

Dyadic Perturbation Observer Framework for Control of a Class of Nonlinear PDE/ODE Systems

Aditya A. Paranjape and Soon-Jo Chung

Abstract—This paper presents the general theory of the dyadic perturbation observer (DPO) framework as a generic method for controlling a class of systems described by partial and/or ordinary differential equations. The method is particularly applicable to boundary control problems for systems described by partial differential equations (PDEs). Conditions for closed-loop stability and robustness are derived using the small gain theorem, and the results are further specialised for finite dimensional systems.

I. INTRODUCTION

The Dyadic Perturbation Observer (DPO) framework was first presented, under the title of perturbation observer-based control, in [12] although its closed-loop stability was not explicitly proved. The method was demonstrated successfully in experiments involving control of beam bending in [11], [12]. The objective of this note is to present the general theory of the DPO framework as a generic method for a class of systems described by ordinary and partial differential equations (ODEs and PDEs), including combinations of both, and derive conditions for closed-loop stability and robustness.

Systems described by a combination of ODEs and PDEs arise naturally in engineering applications, such as flexible aircraft wings (flexible wing structure combined with the rigid body aircraft dynamics), robotic surgical systems (a multi-segmented flexible robotic arm), temperature control systems (heat diffusion and mass flow of air), etc. There are several well-established families of methods for designing controllers for finite dimensional systems, such as dynamic inversion, backstepping, gain scheduling, and Lyapunov function-based approaches. The important feature of all these methods is that they apply to any given class of ODEs, although it may not always be convenient to apply one particular method to a given system. In comparison, systems described by nonlinear PDEs are controlled either through their ODE approximations [1], [2] or using methods which leave the PDE intact and yield closed-loop stability and performance guarantees, but tend to require information about the exact structure of the PDE [6], [8], [9], [13].

The DPO framework is designed primarily for the following class of PDE systems, although it applies equally well to ODE systems:

$$w_t(t, x) \triangleq \frac{\partial w(t, x)}{\partial t} = \mathcal{A}w(t, x) + f(t, x, \mathbf{w}(t, x)) \quad (1)$$

The authors are with the Department of Aerospace Engineering and the Coordinated Science Laboratory at the University of Illinois at Urbana-Champaign. Email: {paranja2, sjchung}@illinois.edu. This research was supported by NSF (IIS-1253758) and ARO (W911NF-10-1-0296).

where $w(t, x)$ is the state of the system, x is the spatial coordinate, and \mathbf{w} denotes the vector of w and its partial spatial derivatives. The problem formulation will be made precise later in the paper. Note that the operator \mathcal{A} is a linear, time-invariant operator. The nonlinearities are all captured by the function $f(\cdot)$. We denote by w_x the partial derivative $\partial w / \partial x$, additional subscripts denote higher order partial derivatives with respect to those variables, and $\mathbf{w}_x(t, x)$ is defined likewise.

Example 1. In the most simplified form, the bending dynamics of a wing attached to a moving aircraft are given by [10]

$$\begin{aligned} \xi_{tt} + EI(\eta \xi_{txxxx} + \xi_{xxxx}) &= F(x, \xi, \alpha, V), \\ \xi(t, 0) = \xi_x(t, 0) = \xi_{xx}(t, L) = \xi_{xxx}(t, L) &= 0 \\ \dot{\alpha} &= q - \frac{1}{mV} \left(\int_0^L F(t, x, \xi, \alpha) dx \right) + \frac{g}{V} \\ \dot{q} &= \frac{1}{I_q} \left(x_a \int_0^L F(t, x, \xi, \alpha) dx + M_{\text{tail}} \right) \end{aligned} \quad (2)$$

where $\eta > 0$ is the coefficient of Kelvin-Voigt damping, while $F(t, y, \xi, \alpha)$ denotes the nonlinear aerodynamic force terms on the wing per unit span. The dynamics of the angle of attack α and the pitch rate q capture the rigid body motion of the aircraft at speed V . The term M_{tail} denotes the control moment from the horizontal tail of the aircraft, x_a is a reference length which measures the distance between the wing and the center of mass of the aircraft, and I_q is the principal moment of inertia about the pitching axis.

The left-hand side of (2) captures the elastic behavior of the wing. Moreover, for a wing immersed in an external flow field, the stack ξ is given by $\xi = [\xi, \xi_t, \xi_x]$, although other spatio-temporal derivatives may be included for completeness. Control design for this problem, with $\xi_x(t, 0)$ treated as the control input, has been addressed in [12], while the stability of the closed loop is addressed in this paper.

The DPO framework decomposes the system in (1) into two halves for the purpose of control design: one half (called the *particular half*) only accommodates the nonlinearity ($f(\cdot)$ in (1)), while the other half (called the *homogeneous half*) accommodates only the control input (which could be a boundary condition of a PDE). The DPO architecture has been illustrated in Fig. 1. The control signal is designed to ensure that the output of the homogeneous half tracks the desired reference signal minus the output of the particular half, thereby ensuring that the output of the two halves put together tracks the reference signal. The stability of the closed loop is verified

explicitly using the small gain theorem. Note that the observer is used (in line with the certainty equivalence principle) to identify the particular and homogeneous state variables. By nature of its design, the DPO framework is inherently adaptive in nature so that it can accommodate modeling and parametric uncertainties, as well as external disturbances (e.g., see [12] for the use of projection-based adaptive control along with the DPO).

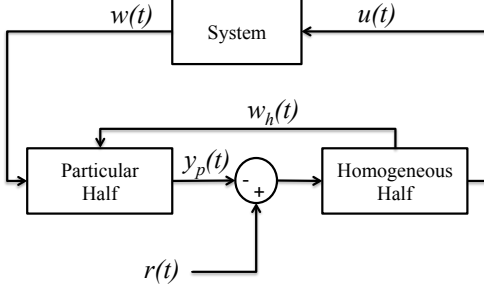


Fig. 1. A block diagram of the DPO framework, with the subscripts p and h denoting the particular and homogeneous components, respectively.

The salient features of the DPO method are:

- 1) The DPO control design is *dimension-independent*; i.e., it can be applied to finite as well as infinite dimensional systems (or a combination thereof).
- 2) The DPO does not prescribe any particular control design for the homogeneous half; any control signal that guarantees tracking is admissible, including nonlinear control signals, as long as the resulting closed-loop system satisfies a small-gain condition.

The paper is organized as follows. Mathematical preliminaries are recapitulated in Sec. II, followed by the problem formulation in Sec. III. The DPO control architecture has been presented in Sec. IV, while a finite dimensional analogue is discussed briefly in Sec. V. Simulation results illustrating the DPO framework are presented in Sec. VI.

II. PRELIMINARIES

Let Z be a Hilbert space with the usual inner product defined by $\langle z_1, z_2 \rangle = \int_0^L z_1^T z_2 dy$ for any $z_1, z_2 \in Z$, where L denotes the total span of the spatial dimension. We are concerned with variables $w(t, x) \in \mathbb{R} \times Z$, with $x \in [0, L]$. We define the space $\mathbb{W} = \mathbb{R}^+ \times Z$, so that $w(t, x) \in \mathbb{W}$. The space \mathbb{W} is a Banach space with the norm defined as follows.

Definition 1. Given $w(t, x) \in \mathbb{W}$, we define the following norms:

$$\begin{aligned} \|w(t)\|_Z &= \sqrt{\int_0^L w(t, x)^T w(t, x) dx} \\ \|w\|_{\mathbb{W}} &= \text{ess sup}_{t \geq 0} \sqrt{\int_0^L w(t, x)^T w(t, x) dx} \end{aligned} \quad (3)$$

while the truncated norm is given by

$$\|w\|_{\mathbb{W}, \tau} = \text{ess sup}_{0 \leq t \leq \tau} \sqrt{\int_0^L w(t, x)^T w(t, x) dx}$$

Definition 2. Given an operator $\mathcal{A} : \mathbb{W} \mapsto \mathbb{W}$ we denote its induced norm by $\|\mathcal{A}\|_i$.

For a time-varying signal $p(t) \in \mathbb{R}$, we define its \mathcal{L}_1 norm as $\|p\|_{\mathcal{L}_1} = \int_0^\infty |p(t)| dt$. It can be checked that $\|\mathcal{A}\|_i = \|\sigma_{\max, x}(\mathcal{A}(t))\|_{\mathcal{L}_1}$, where $\sigma_{\max, x}(\mathcal{A}(t))$ is a time-varying signal and the maximum singular value is taken over all values of x at each instant in time. It must be noted that the \mathcal{L}_1 norm is taken with respect to time.

Definition 3. Given $w(t, x) \in \mathbb{W}$, let $\mathbf{w}(t, x)$ denote a vector of w and its partial spatial derivatives with orders less than that of the highest order in the operator \mathcal{A} . This is a fairly straight-forward extension and allows for accommodating forcing functions that depend on the partial derivatives of w .

Assumption 1. We set all initial conditions to zero. This does not alter the fundamental nature of the result because it only introduces exponentially decaying terms.

Next, we state a variation-of-constants-like formula for infinite dimensional systems (Lemma 3.1.2, [3]).

Lemma 1. Consider a system $\dot{w} = \mathcal{A}w + f(t, x, \mathbf{w})$, $w(t) = w_0 \in D(\mathcal{A}) \subseteq \mathbb{W}$, where \mathcal{A} is the infinitesimal generator of a semigroup $\mathcal{T}(t)$ and $D(\mathcal{A})$ denotes the domain of \mathcal{A} . Suppose that $f(\cdot)$ is a smooth function of its arguments. Then, $w(t)$ is given by

$$w(t) = \mathcal{T}(t)w_0 + \int_0^t \mathcal{T}(t - \tau)f(\tau, x, \mathbf{w}(\tau)) d\tau$$

where $w_0 = w(0, \cdot)$, which is set to zero by Assumption 1.

Definition 4. Given a semi-group $\mathcal{T}(t)$, we define the operator $\mathcal{T}(t) \star : \mathbb{W} \mapsto \mathbb{W}$ so that $\forall q(t, x) \in \mathbb{W}$ and $\forall t > 0$,

$$\mathcal{T}(t) \star q(t, x) = \int_0^t \mathcal{T}(t - \tau)q(\tau, x) d\tau$$

We further define $\mathcal{T} \star \triangleq \lim_{t \rightarrow \infty} \mathcal{T}(t) \star$, and the induced norm

$$\|\mathcal{T} \star\|_i \triangleq \sup_{t \geq 0} \|\mathcal{T}(t) \star\|_i$$

In order to help establish point-wise boundedness in space (as against integral boundedness in the sense of \mathbb{Z}), we introduce Agmon's inequality (Lemma 2.4, [8]).

Lemma 2 (Agmon's inequality). Given $w(t, x)$ satisfying $\|w(t)\|_{\mathbb{Z}} < \infty$ and $\|w_x(t)\|_{\mathbb{Z}} < \infty$, we have

$$\max_{0 \leq x \leq L} |w(t, x)|^2 \leq |w(t, 0)|^2 + 2\|w(t)\|_{\mathbb{Z}}\|w_x(t)\|_{\mathbb{Z}}$$

Agmon's inequality allows us to bound the \mathcal{L}_∞ norm of signals in the spatial domain provided the spatial \mathbb{Z} norms of the signals and their first derivatives are bounded.

Definition 5. Given $p(t) \in \mathbb{R}^n$ with components $p_i(t)$ ($1 \leq i \leq n$), we define

$$\begin{aligned} \|p(t)\|_\infty &= \max_{1 \leq i \leq n} |p_i(t)| \\ \|p\|_{\mathcal{L}_\infty} &= \text{ess sup}_{t \geq 0} \|p(t)\|_\infty, \quad \|p\|_{\mathcal{L}_\infty, \tau} = \text{ess sup}_{0 \leq t \leq \tau} \|p(t)\|_\infty \end{aligned}$$

If $\|p\|_{\mathcal{L}_\infty} < \infty$, then we denote $p \in \mathcal{L}_\infty^n$.

Definition 6. The \mathcal{L}_1 norm of a linear operator $\mathcal{F} : \mathcal{L}_\infty^n \mapsto \mathcal{L}_\infty^m$ is defined as $\|\mathcal{F}\|_{\mathcal{L}_1} = \sup_{\|p\|_{\mathcal{L}_\infty}=1} \|\mathcal{F}p\|_{\mathcal{L}_\infty}$, $p \in \mathcal{L}_\infty^n$

III. PROBLEM FORMULATION

We consider a class of systems described by PDEs of the form

$$w_t = \mathcal{A}w + f(t, x, \mathbf{w}), \mathcal{B}w = u(t), \mathcal{N}w = 0, y(t) = \mathcal{C}w \quad (4)$$

where $w \triangleq w(t, x)$; $u(t)$, $y(t) \in \mathbb{R}$, and \mathcal{A} is the infinitesimal generator of a continuous semigroup $\mathcal{T}(t)$. The right-hand side, $f(t, x, \mathbf{w})$, is a nonlinear function of its arguments. The operators \mathcal{N} and \mathcal{B} capture, respectively, the homogeneous boundary conditions and the boundary control input. The control objective is to ensure that the toutput $y(t)$ tracks a reference signal $r(t) \in \mathbb{R}$.

Assumption 2. The semigroup $\mathcal{T}(t)$ (whose infinitesimal generator is \mathcal{A} in (4)) satisfies $\|\mathcal{T}(t)\|_i \leq Me^{-\omega t} \forall t \geq 0$, where $\omega > 0$ is a constant. Moreover, $\|\mathcal{T} \star\|_i$ is bounded.

Thus, the system dynamics can be viewed as the sum of a linear, exponentially stable, well-posed operator and an external nonlinear forcing term.

Assumption 3. For every $\rho > 0$, there exist positive constants $\nu_1(\rho)$ and $\nu_2(\rho)$ such that if $\|w\|_{\mathbb{W}, \tau} < \rho$ for some $\tau > 0$, then

$$\|f(t, x, \mathbf{w})\|_{\mathbb{W}, \tau} \leq \nu_1(\rho)\|w\|_{\mathbb{W}, \tau} + \nu_2(\rho),$$

In general, $\nu_1(\rho)$ and $\nu_2(\rho)$ are class \mathcal{K} functions of ρ .

The above assumption essentially implies that the spatial derivatives of $w(t, x)$ enter through bounded functions. As an illustration, in Example 1, the spatial derivative $\xi_x(t, x)$ enters through the trigonometric functions $\cos(\xi_x(t, x))$ and $\sin(\xi_x(t, x))$.

Assumption 4. The output operator \mathcal{C} in (4) is bounded; i.e., $\|y\|_{\mathcal{L}_\infty} = \|\mathcal{C}w(t, x)\|_{\mathcal{L}_\infty} \leq K\|w\|_{\mathbb{W}}$ for some constant K .

Example 2. Let $y(t) = \int_0^L w(t, x)dx$. Then, $|y(t)| = \left| \int_0^L w(t, x)dy \right| \leq \sqrt{L}\|w(t)\|_{\mathbb{Z}} \implies \|y\|_{\mathcal{L}_\infty} \leq \sqrt{L}\|w\|_{\mathbb{W}}$. Note that the inequality is a consequence of $w(t, x)$ lying in a Hilbert space. Assumption 4 is relaxed in Sec. IV-C. An example of an unbounded operator is the value of $w(t, x)$ at a boundary, e.g., $\mathcal{C}w(t, x) = w(t, 0)$.

IV. CONTROL DESIGN USING DPO

A. Design of the Perturbation Observers

We use the operator $\hat{\cdot}$ to denote observer states, and the subscripts p and h to denote states of the particular and the homogeneous halves, respectively. The dynamics of the two halves are given by

$$\hat{w}_{p,t} = \mathcal{A}\hat{w}_p + \hat{f}(t, x, \mathbf{w}), \mathcal{B}\hat{w}_p = \mathcal{N}\hat{w}_h = 0, \hat{y}_p = \mathcal{C}\hat{w}_p \quad (5)$$

$$\hat{w}_{h,t} = \mathcal{A}\hat{w}_h, \mathcal{B}\hat{w}_h = u(t), \mathcal{N}\hat{w}_h = 0, \hat{y}_h = \mathcal{C}\hat{w}_h \quad (6)$$

Recall that the subscript t denotes the partial derivative $\partial/\partial t$. Using the projection operator to design $\hat{f}(\cdot)$, such as in [12], we can show the following result.

Lemma 3. If $\|w\|_{\mathbb{W}} < \rho$, then there exist constants $\kappa_0 \equiv \kappa_0(\rho)$ and $\kappa_1 \equiv \kappa_1(\rho)$ such that $\|\hat{w}_p\|_{\mathbb{W}} \leq \kappa_0\|w\|_{\mathbb{W}} + \kappa_1$

Proof: The proof follows by applying Lemma 1 to (5) and computing the norm of \hat{w}_p . ■

We define the observation error $\tilde{w} = \hat{w}_p + \hat{w}_h - w$. Then, from (4), (5), and (6), we conclude that the dynamics of \tilde{w} are given by

$$\begin{aligned} \tilde{w}_t &= \mathcal{A}\tilde{w} + \hat{f}(t, x, \mathbf{w}) - f(t, x, \mathbf{w}), \\ \mathcal{B}\tilde{w} &= \mathcal{N}\tilde{w} = 0, \tilde{y}(t) = \mathcal{C}\tilde{w}(t, x) \end{aligned} \quad (7)$$

Lemma 4. It is possible to ensure that $\|\tilde{w}(t)\|_{\mathbb{Z}}$ is uniformly bounded $\forall t > 0$, and the bound can be made arbitrarily small. It follows as a corollary that $\tilde{y}(t)$ is uniformly bounded and can be made arbitrarily small.

Proof: The boundedness of $\|\tilde{w}\|_{\mathbb{Z}}$ is proved in [12] (Theorem 4), while that of $\tilde{y}(t)$ follows from Assumption 4. ■

B. DPO Control Synthesis and Closed-Loop Stability Analysis

We design the control signal $u(t)$ to ensure that the output of the homogeneous half, $\hat{y}_h(t)$ in (6), tracks a reference signal $r(t) - \hat{y}_p(t)$, where $r(t)$ is the reference signal for the original system (4), where \hat{y}_p is the output of the particular half (5). Lemma 4 would then ensure that the output $y(t)$ of the system (4) tracks the reference signal $r(t)$, as desired. We can write the input-output dynamics of the linear, exponentially stable homogeneous half in (6) in the Laplace domain [4]: $\hat{y}_h(s) = G_c(s)u(s)$, where the transfer function $G_c(s)$ depends on \mathcal{A} and the boundary conditions, as explained in [4]. We design $u(t)$ in the Laplace domain as follows:

$$u(s) = H(s)(r(s) - \hat{y}_p(s)) = H(s)(r(s) - \mathcal{C}\hat{w}_p(s)) \quad (8)$$

The ideal choice for $H(s)$ would then be $1/G_c(s)$ which is, in general, neither proper nor stable. Therefore, we choose $H(s)$ to satisfy $H(0)G_c(0) = 1$ and impose further conditions for closed-loop stability (see Theorem 1). Interestingly, a polynomial approximation of the state \hat{w}_h yields a low-pass filter $H(s)$ which ensures that $u(t)$ is sufficiently differentiable, and all derivatives are bounded [11], [12].

The next result asserts the boundedness of control inputs.

Lemma 5. If $\|w\|_{\mathbb{W}} < \rho$, then the control law in (8) ensures that there exist constants $\delta_{ir} \equiv \delta_{ir}(\rho, H(s))$, $\delta_{iw} \equiv \delta_{iw}(\rho, H(s))$, and $\delta_{iu} \equiv \delta_{iu}(\rho, H(s))$ such that $\|u^{(i)}\|_{\mathcal{L}_\infty} \leq \delta_{ir}\|r\|_{\mathcal{L}_\infty} + \delta_{iw}\|w\|_{\mathbb{W}} + \delta_{iu}$, where $u^{(i)}(t) = \frac{d^i u(t)}{dt^i}$ and $u^{(0)}(t) = u(t)$.

Proof: From (8), we get $\|u\|_{\mathcal{L}_\infty} \leq \|H(s)\|_{\mathcal{L}_1}(\|r\|_{\mathcal{L}_\infty} + \|\mathcal{C}\hat{w}_p\|_{\mathcal{L}_\infty})$. The proof follows from Assumption 4 and Lemma 3. ■

We will prove the bounded-input-bounded-output (BIBO) stability of the closed-loop (in the sense of \mathcal{L}_∞ boundedness of signals) using the small gain theorem. The first result asserts that the boundary control system in (4) can be recast into a PDE system with *homogeneous* boundary conditions (Theorem 3.3.3, [3]).

Lemma 6. The coordinate transform $v = w - \beta u$, where the operator β satisfies $\mathcal{B}\beta u = u$ and $\mathcal{N}\beta u = 0$, transforms the system (4) into the form

$$\dot{v} = \mathcal{A}v + \mathcal{A}\beta u - \beta \dot{u} + f(t, y, \mathbf{w}), \quad \mathcal{B}v = \mathcal{N}v = 0 \quad (9)$$

Consider the system in (9), and suppose $\|w(t)\|_{\mathbb{Z}} = \rho$ for some time $t > 0$ and furthermore, $\|w(\tau)\|_{\mathbb{Z}} < \rho \forall \tau < t$. Using Lemma 1, Assumption 3 and Lemma 5, we get

$$\|v\|_{\mathbb{W},t} \leq \|\mathcal{T} \star\|_i(\delta_0\|w\|_{\mathbb{W},t} + \delta_1\|r\|_{\mathcal{L}_\infty} + \delta_2)$$

where $\delta_0 = \nu_0(\rho) + \|\mathcal{A}\beta\|_i\delta_{0w} + \|\beta\|_i\delta_{1w}$, $\delta_1 = \|\mathcal{A}\beta\|_i\delta_{0r} + \|\beta\|_i\delta_{1r}$, and $\delta_2 = \nu_1(\rho) + \|\mathcal{A}\beta\|_i\delta_{0u} + \|\beta\|_i\delta_{1u}$. Since $w = v + \beta u$, using the triangle inequality and Lemma 5, we get

$$\begin{aligned} \|w\|_{\mathbb{W},t} &\leq \|\mathcal{T} \star\|_i(\delta_0\|w\|_{\mathbb{W},t} + \delta_1\|r\|_{\mathcal{L}_\infty} + \delta_2) \\ &\quad + \|\beta\|_i(\delta_{0w}\|w\|_{\mathbb{W},t} + \delta_{0r}\|r\|_{\mathcal{L}_\infty} + \delta_{0u}) \\ \implies \|w\|_{\mathbb{W},t} &\leq \frac{\Delta_1\|r\|_{\mathcal{L}_\infty} + \Delta_2}{1 - \Delta_0} \end{aligned} \quad (10)$$

$$\begin{aligned} \Delta_0 &= \|\mathcal{T} \star\|_i\delta_0 + \|\beta\|_i\delta_{0w}, \quad \Delta_1 = \|\mathcal{T} \star\|_i\delta_1 + \|\beta\|_i\delta_{0r}, \\ \Delta_2 &= \|\mathcal{T} \star\|_i\delta_2 + \|\beta\|_i\delta_{0u} \end{aligned} \quad (11)$$

We prove the following result.

Theorem 1. The closed-loop system (4), (5), (6), and (8) is BIBO stable in the sense of \mathcal{L}_∞ if there exists a stable, strictly proper $H(s)$ and a constant ρ such that

$$\frac{\Delta_1\|r\|_{\mathcal{L}_\infty} + \Delta_2}{1 - \Delta_0} \leq \rho - \epsilon \quad (12)$$

where Δ_i 's are defined in (11), and $\epsilon > 0$ is arbitrarily small

Proof: Suppose that $\|w\|_{\mathbb{W},t} = \|w(t)\|_{\mathbb{Z}} = \rho$ for some $t > 0$. Then, from (10) and (12), it follows that $\|w\|_{\mathbb{W},t} \leq \rho - \epsilon < \rho$, which contradicts the assumption that $\|w\|_{\mathbb{W},t} = \rho$, and shows that $\|w\|_{\mathbb{W}} < \rho \forall t$. This completes the proof. ■

C. Redressing Assumption 4 and Generalization

It is possible to relax Assumption 4 by deriving a stability condition of the form in Theorem 1 for a system consisting of the dynamics of \mathbf{w} rather than just w . Recall that \mathbf{w} is the vector of w and its partial spatial derivatives. The resulting stability condition is cumbersome and difficult to verify in a practical setting; its representation in a more tractable form is an open problem. It must be noted that the \mathbf{w} dynamics are constructed purely as an analytical tool to verify the stability of the closed loop system (4), (5), (6), and (8).

We start by showing a number of properties. Given the system (4), we can differentiate the state variable $w(t, x)$ with respect to x and recast it into the form

$$\begin{aligned} \dot{\mathbf{w}} &= \bar{\mathcal{A}}(\mathbf{w})\mathbf{w} + \bar{f}(t, x, \mathbf{w}) \\ \bar{\mathcal{B}}\mathbf{w} &= u(t), \quad \bar{\mathcal{N}}\mathbf{w} = 0, \quad y(t) = \bar{\mathcal{C}}\mathbf{w} \end{aligned} \quad (13)$$

Example 3. Consider the PDE system $\xi_t + \xi_{xx} = \sin(\xi_x) + x^2$, with the boundary control $\xi(t, 0) = u(t)$. The array $\xi = [\xi, \xi_x]$. From the above equation, we have that

$$\xi_{xt} + \xi_{xxx} = \cos(\xi_x)\xi_{xx} + 2x,$$

so that, using the notation from (13),

$$\begin{aligned} \bar{\mathcal{A}}(\xi) &= \begin{bmatrix} -\frac{\partial^2}{\partial x^2} & 0 \\ 0 & \cos(\xi_x)\frac{\partial}{\partial x} - \frac{\partial^2}{\partial x^2} \end{bmatrix} \\ \bar{\mathcal{B}}\xi &= \xi(t, 0) \\ \bar{f}(t, x, \xi) &= [\sin(\xi_x) + x^2, 2x]^\top \end{aligned}$$

Note that the operator $\bar{\mathcal{A}}(\xi)$ is the sum of the original operator \mathcal{A} along the diagonal and additional terms that arise due to partial derivatives of ξ on the right-hand side. Note that the representation is not unique, in that

$$\bar{\mathcal{A}}(\xi) = \begin{bmatrix} -\frac{\partial^2}{\partial x^2} & 0 \\ \cos(\xi_x)\frac{\partial^2}{\partial x^2} & -\frac{\partial^2}{\partial x^2} \end{bmatrix}$$

is also an admissible representation. It may be possible to use convex combinations of admissible representations in order to elicit better global convergence properties (since each representation is generally nonlinear) as in [5], but this possibility is not explored in the present paper.

We prove the boundness of $\mathcal{C}\hat{w}_p$, which is essential to ensure the boundedness of the control signal $u(t)$ in (8). This result is a direct generalization of Lemma 3.

Lemma 7. If there exist constants $\rho_1, \rho_2 > 0$ such that $\|\mathbf{w}(t)\|_{\mathbb{Z}} < \rho_1$ and $\|\mathbf{w}_x(t)\|_{\mathbb{Z}} < \rho_2$ for some $t \geq 0$, then there exist constants $\kappa_0 \equiv \kappa_0(\rho_1, \rho_2)$ and $\kappa_1 \equiv \kappa_1(\rho_1, \rho_2)$ such that

$$\max(\|\hat{w}_p(t)\|_{\mathbb{Z}}, \|\hat{w}_{p,x}(t)\|_{\mathbb{Z}}) < \kappa_0\|w(t)\|_{\mathbb{Z}} + \kappa_1 \quad (14)$$

so that

$$|\hat{y}_p(t)|^2 = |\mathcal{C}\hat{w}_p(t)|^2 \leq 2(\kappa_0\|w(t)\|_{\mathbb{Z}} + \kappa_1) \quad (15)$$

Proof: To prove (11), we note that the dynamics of $\hat{w}_{p,x}$ can be written as

$$\hat{w}_{p,x} = \mathcal{A}\hat{w}_{p,x} + g(t, x, \mathbf{w})$$

where

$$g(t, x, \mathbf{w}) = \frac{\partial f(t, x, \mathbf{w})}{\partial x} + \frac{\partial f(t, x, \mathbf{w})}{\partial \mathbf{w}}\mathbf{w}_x$$

Applying Lemma 1 and taking the norm of both sides yields (14), from which (15) follows as a direct consequence of applying Agmon's inequality (Lemma 2). ■

We state the main result and allude to the fact that its proof is identical to Theorem 1.

Theorem 2. Consider the system (13). Suppose that a stable representation $\bar{\mathcal{A}}(\mathbf{w})$ exists and furthermore, there exists an operator \mathcal{A}_0 which gives a lower bound on the decay rate of trajectories corresponding to $\bar{\mathcal{A}}(\mathbf{w})$. Then there exists a semi-group $T_0(t)$ corresponding to \mathcal{A}_0 satisfying the growth bound similar to Assumption 2. Furthermore, there exists a BIBO (in the sense of \mathcal{L}_∞) stabilizing controller given by (5), (6), and (8) provided the small gain condition of Theorem 1 is satisfied (with the operator $\mathcal{T}(t)$ replaced by $T_0(t)$).

Although we derived the above results for a class of systems of the form $\dot{w} = \mathcal{A}w + f(t, x, \mathbf{w})$ with \mathcal{A} stable, the method can be readily used for systems of the form $\dot{w} = \mathcal{A}_g w +$

$f(t, x, \mathbf{w})$, where \mathcal{A}_g need not be stable and could even be zero. The system be rewritten as

$$\dot{w} = \mathcal{A}w + h(t, x, \mathbf{w}), \quad h(t, x, \mathbf{w}) = f(t, x, \mathbf{w}) + \mathcal{A}_g w - \mathcal{A}w \quad (16)$$

and Theorem 2 can be employed directly. Conditions under which a *particular* \mathcal{A} (as compared to some stable \mathcal{A}) exists is an open problem.

V. INSIGHTS FROM FINITE DIMENSIONAL ODE SYSTEMS

In this section, we will start with a finite-dimensional linear time-invariant (LTI) system to identify conditions under which a DPO controller would lead to a stable closed-loop system. Thereafter, we will specialize Theorem 1 to finite dimensional nonlinear systems. The resulting controller and the small gain stability condition will be similar to those obtained in \mathcal{L}_1 adaptive control [7]. The conditions obtained in this section would be important while using DPO in a practical setting, where hardware implementation and verification and validation protocols would run in a finite dimensional setting.

A. Application to Linear Time-Invariant Systems

Consider the ODE system

$$\dot{w}(t) = \mathcal{A}w(t) + Bu(t), \quad y(t) = Cw(t) + Du(t) \quad (17)$$

where $w \in \mathbb{R}^n$, and $u, y \in \mathbb{R}$. The system is assumed to be observable and controllable. The control objective is to ensure that $y(t)$ tracks a reference signal $r(t)$.

The particular and the homogenous halves are given by

$$\begin{aligned} \dot{\hat{w}}_p(t) &= A_m \hat{w}_p(t) - BKw(t), \quad \hat{y}_p(t) = C\hat{w}_p(t) \\ \dot{\hat{w}}_h(t) &= A_m \hat{w}_h(t) + Bu(t), \quad \hat{y}_h(t) = C\hat{w}_h(t) + Du(t) \end{aligned} \quad (18)$$

where $A_m = A + BK$ is Hurwitz. Let $\tilde{w} = \hat{w}_p + \hat{w}_h - w$ denote the error between the observer in (18) and the system in (17). The dynamics of \tilde{w} are given by $\dot{\tilde{w}}(t) = A_m \tilde{w}(t)$ and $\tilde{y}(t) = C\tilde{w}(t)$. Clearly, $\tilde{w}(t) \rightarrow 0$ and $\tilde{y}(t) \rightarrow 0$ exponentially.

Let $G(s) = C(sI - A_m)^{-1}B$ and $G_c(s) = G(s) + D$. Then, from (18), it follows that $\hat{y}_h(s) = G_c(s)u(s)$ and $\hat{y}_p(s) = -G(s)Kw(s)$. A control signal analogous to (8) is given by $u(s) = H(s)(r(s) - \hat{y}_p(s))$, so that $\hat{y}_h(s) = G_c(s)H(s)(r(s) - \hat{y}_p(s))$. We want $\hat{y}_h(t)$ to track $r(t) - \hat{y}_p(t)$. The ideal choice for $H(s)$ would then be $1/G_c(s)$ which is, in general, neither proper nor stable. Therefore, we choose $H(s)$ so that $H(0)G_c(0) = 1$ to guarantee asymptotic tracking and impose further conditions on $H(s)$ to ensure a stable closed-loop system. The closed-loop dynamics are obtained by substituting for $u(t)$ in (17), whose Laplace transform is given by $sw(s) = Ax(s) + BH(s)(r(s) + G(s)Kw(s))$. Since $A = A_m - BK$, we get

$$w(s) = (sI - A_m + BK(1 - G(s)H(s)))^{-1}H(s)Br(s) \quad (19)$$

Theorem 3. *The closed-loop system (17) and (18) is exponentially stable if and only there exist $K \in \mathbb{R}^n$ and a stable transfer function $H(s)$ such that: (a) $A + BK$ is Hurwitz, and (b) all poles of $(I_n + (sI - A_m)^{-1}BK(1 - G(s)H(s)))^{-1}B$ lie in the open left half plane, where $G(s) = C(sI - A_m)^{-1}B$ and I_n is the identity matrix of size n .*

Proof: We require A_m to be Hurwitz so that the the observation error (\tilde{w}) dynamics are stable. Part (b) can be proved by writing the closed-loop system in the form (19). ■

B. Application to Finite Dimensional Nonlinear Systems

Next, we assume that the system is of the form

$$\dot{w} = A_m w + bu + f(w), \quad y = cw \quad (20)$$

where $w \in \mathbb{R}^n$, $f : \mathbb{R}^n \rightarrow \mathbb{R}^n$, and $u, y \in \mathbb{R}$. The nonlinearity $f(w)$ is generally not matched to $u(t)$, i.e., it is not always possible to write $f(w) = bg(w)$ for some nonlinear $g(w)$.

Remark 1. *The system could be nonlinear and of the form $\dot{w} = f_0(w) + bu$, in which case, in (17), $f(w) = f_0(w) - A_m w$. Clearly, A_m is also a design element, constrained by the stability and performance requirements.*

1) *Perturbation Observer Design:* Let \hat{w}_p and \hat{w}_h denote the states of the particular and the homogeneous half, and let $\hat{w} = \hat{w}_p + \hat{w}_h$. Let $\tilde{w} = \hat{w} - w$. The dynamics of the two halves are given by

$$\dot{\hat{w}}_p = A_m \hat{w}_p + \hat{f}(w), \quad \hat{y}_p = c\hat{w}_p \quad (21)$$

$$\dot{\hat{w}}_h = A_m \hat{w}_h + bu, \quad \hat{y}_h = c\hat{w}_h \quad (22)$$

where $\hat{f}(w)$ is the predicted value of $f(w)$. This can be done using a wide range of methods, such as the projection operator and we retain this notation for simplicity.

2) *Design of Control Signal:* As in (8), we choose a control signal $u(t)$ whose Laplace transform is given by

$$u(s) = H(s)(r(s) - \hat{y}_p(s)) \quad (23)$$

so that $\hat{y}_h(s) = c(sI - A_m)^{-1}bH(s)(r(s) - \hat{y}_p(s))$, and we prescribe $H(0) = -1/(cA_m b)$.

3) *Closed-Loop Stability:* In order to show stability of the closed-loop, we need to introduce some notation, following that introduced earlier for the general system represented in the operator form.

Assumption 5. *If for some $t > 0$, $\|w\|_{\mathcal{L}_{\infty},t} < \rho_b$, where $\rho_b \in \mathbb{R}^+$, then there exist constants $\delta_0 \triangleq \delta(\rho_b)$ and $\delta_1 \triangleq \delta_1(\rho_b)$, with $\delta_0, \delta_1 \in \mathbb{R}^+$ such that $\|f(w)\|_{\mathcal{L}_{\infty},t} \leq \delta_0\|w\|_{\mathcal{L}_{\infty},t} + \delta_1$ for all $t \in \mathbb{R}$.*

The next assumption concerns $\hat{f}(w)$ in (21). Using techniques such as the projection operator to design $\hat{f}(w)$, we ensure that $\|\hat{f}(w) - f(w)\|_{\infty}$ is globally uniformly bounded.

Assumption 6. *If for some $t > 0$, $\|w\|_{\mathcal{L}_{\infty},t} < \rho_b$, where $\rho_b \in \mathbb{R}^+$, then there exist constants $\kappa_0 \triangleq \kappa(\rho_b)$ and $\kappa_1 \triangleq \kappa_1(\rho_b)$, with $\kappa_0, \kappa_1 \in \mathbb{R}^+$ such that $\|\hat{f}(w) - f(w)\|_{\mathcal{L}_{\infty},t} \leq \kappa_0\|w\|_{\mathcal{L}_{\infty},t} + \kappa_1$.*

Finally, we state a small-gain design condition which is critical to the stability proof that follows.

Assumption 7. *There exists a low pass filter $H(s)$ and a scalar $\Gamma > 0$ such that*

$$1 - \|(sI - A_m)^{-1}bH(s)\|_{\mathcal{L}_1} \|(sI - A_m)^{-1}\|_{\mathcal{L}_1} \|c\|_{\infty} (\kappa_0 + \delta_0) - \|(sI - A_m)^{-1}\|_{\mathcal{L}_1} \delta_0 > \Gamma \quad (24)$$

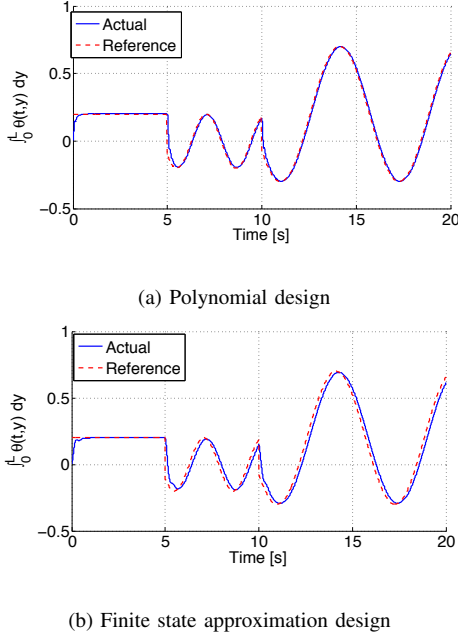


Fig. 2. DPO illustrated with two different control synthesis methods.

Define a constant $\rho = N/D$, where the numerator N is given by

$$N = \|(sI - A_m)^{-1}bH(s)\|_{\mathcal{L}_1}(\|r\|_{\mathcal{L}_\infty} + \|(sI - A_m)^{-1}\|_{\mathcal{L}_1}\|c\|_{\infty}(\delta_1 + \kappa_1)) + \|(sI - A_m)^{-1}\|_{\mathcal{L}_1}\delta_1 \quad (25)$$

and the denominator D by

$$D = 1 - \|(sI - A_m)^{-1}\|_{\mathcal{L}_1}\delta_0 - \|(sI - A_m)^{-1}bH(s)\|_{\mathcal{L}_1}(\|(sI - A_m)^{-1}\|_{\mathcal{L}_1}\|c\|_{\infty}(\delta_0 + \kappa_0)) \quad (26)$$

We state the main results, similar to Lemma 3 and Theorem 1. The proofs are omitted for brevity.

Lemma 8. *Consider the particular half of the observer in (21). If $\|w\|_{\mathcal{L}_\infty} < \rho = N/D$, with N and D defined in (25) and (26), then the observer state \hat{w}_p satisfies the bound $\|\hat{w}_p\|_{\mathcal{L}_\infty} \leq \|(sI - A_m)^{-1}\|_{\mathcal{L}_1}((\delta_0 + \kappa_0)\|w\|_{\mathcal{L}_\infty} + (\delta_1 + \kappa_1))$.*

Theorem 4. *The closed-loop system (20), (21), (22), and (23) is BIBO stable and the state w of the closed-loop system satisfies $\|w\|_{\mathcal{L}_\infty} < \rho$.*

VI. SIMULATIONS

Consider the forced wave equation

$$\begin{aligned} \theta_{tt}(t, x) - 0.1\theta_{txx}(t, x) - 2\theta_{yy}(t, x) &= 1000\theta(t, x) \\ \theta_x(t, L = 0.1) &= 0, \quad \theta(t, 0) = u(t), \quad C\theta(t, x) = \int_0^{0.1} \theta(t, x) dy \end{aligned} \quad (27)$$

Note that the dynamics in (28) are unstable. The DPO is designed as follows:

$$\begin{aligned} \hat{\theta}_{p,tt} - 0.1\hat{\theta}_{p,txx} - 2\hat{\theta}_{p,xx} &= \hat{F}(t, x) - p(0.1\hat{\theta}_t(p, t) + 2\hat{\theta}_p(t)) \\ \hat{\theta}_{h,tt} - 0.1\hat{\theta}_{h,txx} - 2\hat{\theta}_{h,xx} &= -p(0.1\hat{\theta}_t(h, t) + 2\hat{\theta}_h(t)) \\ \hat{\theta}_p(t, 0) &= \hat{\theta}_{p,x}(t, 0.1) = 0, \quad \hat{\theta}_h(t, 0) = u(t), \quad \hat{\theta}_{h,x}(t, 0.1) = 0, \end{aligned} \quad (28)$$

where p is a design parameter. The controller is designed using two methods, and the simulations for each design are shown in Fig. 2. The first controller is designed by approximating

the homogeneous half of the observer corresponding to (28) by a polynomial, as explained in [12]. The second controller, of the form (23), is derived for a finite state representation of (28) obtained using Galerkin's method. In both cases, as predicted, the closed-loop system is stable and the tracking error is almost negligible. The closed-loop system is stable when $p \in [450, 550]$ (approximately). This is a consequence of having chosen the right-hand side of (28) in that particular form. The polynomial expansion-based controller presented in this paper has also been demonstrated in experiments on the bending vibrations of a beam [11], [12]. The closed-loop stability criterion does not necessarily inform what a good choice for the RHS would be, and an optimum design of the RHS remains an open problem.

VII. CONCLUSION

In this paper, we presented a novel control method for finite as well infinite dimensional systems based on a two-stage perturbation observer. The control signal is designed for the homogeneous half of the observer, while ‘‘perturbation prediction’’ is accomplished by putting together both halves. The robustness of the controller was proved using the small gain theorem. In particular, we showed that the \mathcal{L}_∞ -norm of the system state (over time for finite dimensional systems, and over space as well as time for PDEs) as well as the control inputs is uniformly bounded. Simulations were performed to demonstrate the effectiveness of the controller.

ACKNOWLEDGEMENT

We gratefully acknowledge the inspiration and the encouragement that we received from Prof. Miroslav Krstic.

REFERENCES

- [1] A. Armaou and P. D. Christofides, ‘‘Wave suppression by nonlinear finite-dimensional control,’’ *Chem. Eng. Sci.*, vol. 55, pp. 2627 – 2640, 2000.
- [2] P. D. Christofides and P. Daoutidis, ‘‘Finite-dimensional control of parabolic PDE systems using approximate inertial manifolds,’’ in *36th IEEE Conf. Dec. Control*, 1997, pp. 1068–1073.
- [3] R. F. Curtain and H. J. Zwart, *An Introduction to Infinite-Dimensional Linear Systems Theory*, ser. Texts in Applied Mathematics (Vol. 21). Springer-Verlag, 1995.
- [4] R. Curtain and K. Morris, ‘‘Transfer functions of distributed parameter systems: A tutorial,’’ *Automatica*, vol. 45, pp. 1101 – 1116, 2009.
- [5] A. P. Dani, S.-J. Chung, and S. Hutchinson, ‘‘Observer design for stochastic nonlinear systems via contraction-based incremental stability,’’ *IEEE Trans. on Autom. Control*, 2013, conditionally accepted.
- [6] W. He, S. S. Ge, B. V. E. How, Y. S. Choo, and K. S. Hong, ‘‘Robust adaptive boundary control of a flexible marine riser with vessel dynamics,’’ *Automatica*, vol. 47, pp. 722 – 732, 2011.
- [7] N. Hovakimyan and C. Cao, *L1 Adaptive Control Theory: Guaranteed Robustness with Fast Adaptation*, ser. Advances in Design and Control. SIAM, 2010.
- [8] M. Krstic and A. Smyshlyaev, *Boundary Control of PDEs: A Course on Backstepping Designs*. Advances in Design and Control, SIAM, 2008.
- [9] —, *Adaptive Control of PDEs*. Princeton University Press, 2010.
- [10] A. A. Paranjape, S.-J. Chung, H. H. Hilton, and A. Chakravarthy, ‘‘Dynamics and performance of tailless micro aerial vehicle with flexible articulated wings,’’ *AIAA J.*, vol. 50, no. 5, pp. 1177 – 1188, 2012.
- [11] A. A. Paranjape, J. Guan, S.-J. Chung, and M. Krstic, ‘‘PDE boundary control for Euler-Bernoulli beam using a two stage perturbation observer,’’ in *IEEE Conf. Dec. Control, Maui, HI*, 2012, pp. 4442 – 4448.
- [12] —, ‘‘PDE boundary control for flexible articulated wings on a robotic aircraft,’’ *IEEE Trans. Robot.*, vol. 29, no. 3, pp. 625 – 640, 2013.
- [13] J.-M. Wang, B. Ren, and M. Krstic, ‘‘Stabilization and Gevrey regularity of a Schrödinger equation in boundary feedback with a heat equations,’’ *IEEE Trans. on Autom. Control*, vol. 57, no. 1, pp. 179 – 185, 2012.



ISU-MECH-00

Planar dielectric elastomer actuator capable of out-of-plane deformation without prestretch

William Lai¹, Ashraf Bastawros¹, Wei Hong¹ and Soon Jo Chung²

1. Department of Aerospace Engineering, Iowa State University
2. Department of Aerospace Engineering, University of Illinois,
Urbana Champaign

October, 2013

Manuscript for possible submission to Soft Matter

1. Introduction

For the last decades, scientists are highly interested in designing biomimicry devices performing as artificial muscles. Compliant and lightweight robotic arms and grippers for tight spaces as well as energy-efficient actuators for biomimetic locomotion have drawn much attention for study. To develop a practical biomimic actuator with good performance, choosing suitable materials is one of the most important and fundamental issues. Smart materials that can be triggered to deform through certain stimulations are what we desire. Besides, muscle-like features, including light, soft, and short responding time, are also expected.

In literatures, numerous of smart materials being proposed. From these materials, electroactive polymers (EAPs) with lightweight and nice compliancy are very suitable to serve as candidates for biomimic actuator applications. EAPs are polymers that are cable of inducing deformation under electrical stimulation. The human-muscle like features, such as lightweight, considerable large displacement, and acceptable response time provide EAPs high potential of artificial muscle applications.

A group of the EAP family, dielectric elastomers (DEs), has especially drawn our attention due to their high strain, comparably short response time, low cost, and high electromechanical coupling efficiency [1-5]. They are often used to fabricate actuators, so called dielectric elastomer actuators (DEAs). Basically, DEAs are made of incompressible soft dielectric elastomer membranes sandwiched between compliant electrode layers to form dynamic capacitors. When electric field is applied across the electrodes, the columbic force generates Maxwell stress [6] that attracts other electrodes together and squeezes the sandwiched incompressible dielectric elastomer layer. As a result, the in-plane expansion of DEA can be observed.

Many different designs of soft actuator have been developed with the usage of dielectric elastomers. Two major ideas were presented in the past: a) actuators with hard frame for supporting prestretch, and b) using prestretch as stored energy for the recovering of bi-stable structures. For an example of hard frame supporting DEA, a robotic-arm design that S. Dubowsky et al. published in 2006 [7] uses frames with deformable joints to support prestretch and, in the meantime, allowing dielectric elastomers to expand while they electric field is applied. This structure makes a semi-freestanding actuation that frame-included movement is presented instead of in-frame-only displacement. Several cells of actuators can be combined together for multi-degree-of-freedom motion. Similarly, by combing DEAs with mechanical structures, P. Lochmatter et al. [8] presented a shell bending actuator with a stack of segments. The shell-like structure has two parallel planar actuators and joint mechanical parts in between. Bending can be observed once one side of DEAs is stimulated and expanded. Also, series of cells can be connected together to induce larger bending motion.

On the other hand, one of the bi-stable structure actuator designs named dielectric elastomer minimum energy system (DEMES) were presented by G. Kofod [9]. With prestretched elastomers attached on deformable frames, actuators may stay in relaxation phase where elastomers are crumpled with no electric field applied. And when the actuators are activated, they may deform into the other stable phase where the energy from applied electric field overcomes the stored energy provided by prestretch and makes elastomer flat. Later, Petralia and Wood [10] further presented their work of a curving chain actuator by combining several paper-frame-based DEMES cells.

In literatures [11,12], prestretch is a method showing great improvement of in-plane actuation strain of dielectric elastomer actuators. Dielectric elastomer actuators with prestretch can achieve more than 300% of strain. In all of these designs, prestretch is taking parts in the fabrication that benefits actuators having large deformation. However, the additional supporting frames cause operational setbacks. For example, weight and space that the prestretch-support structures provide are much more than dielectric elastomer itself [13,14]. In addition, non-uniform prestretch and stress relaxation may affect subsequent actuation [15] and cause local strain division. From our previous experimental observation of planar DEAs [16], actuation strain will be influenced by non-uniform prestretch and may be controlled by the biaxial prestretch ratio. Larger prestretch tends to induce lower actuation strain, and, vice versa, lower prestretch tends induce higher actuation strain.

To minimize the inconveniences come with prestretch, we present another design of dielectric elastomer actuator fabrication with no requirement of prestretch and no additional equipment for supporting prestretch. In this study, freestanding design of DEAs that increases the energy mass ratio and the flexibility of actuators will be revealed. Our idea is using partial surface reinforcement on thin planar dielectric elastomer actuators to induce out-of-plane deformation. When electric field is applied, planar actuators tend to perform in-plane expansion due to the Maxwell stress while stiffeners added on the surface act as surface reinforcements and constrain expansion of designed direction. They induce out-of-plane deformation and guide the bending motions. By applying different configurations of stiffeners on different positions, multiple choices of three dimensional deformations with different directions and degrees of bending and twisting are expectable. Since the planar actuator is based on thin dielectric elastomer, a considerable out-of-plane deformation doesn't require large in-plane expansion that relies on the help of prestretch.

In Suo's work [17], they showed experimental results and analytical analysis of applying fiber reinforcement on the surface of dielectric elastomer actuator. When electric field is applied, the expansion of elastomer is constrained on the direction of fibers and the actuators perform unidirectional actuation. Using similar idea, stiffeners in our work with different are attached on

one surface of a planar actuator partially and constraining the expansion on the surface. This will cause the entire planar actuator deforms out-of-plane significantly.

In this paper, we will show the fabrication of planar actuators. Analytical analysis and FEM simulation will also be provided to investigate the role of stiffener which can be used to change the force-stroke characteristics of actuators.

2. Fabrication Procedure

The fabricated device has a square shape of 25×25mm. It contains elastomer layers (3M VHB F9460PC tapes) and electrode layers (carbon black powder, Super C65, TIMCAL Inc., USA). The elastomer layers include active area in the middle with 22×22mm and inactive border of 1.5mm around the edge for sealing and preventing circuit shorting (Figure 1a). A window mask is used to define the electrode area. Carbon black powder is uniformly brushed over the window mask. Narrow strips of Aluminum foils are attached to the edge of electrode layer to form external terminals of the actuator. Finally, another VHB tape is applied on the stack as a cover. The sequence is repeated for multiple stack modules. The aluminum terminal locations are alternated to separate positive and negative electrode when fabricating multi-layer structure. As an example, sketches of 1 (which is the minimum stack of basic DEA design), 2, and 3-cell structure are shown in Figure 2. After this, the stiffener, 3M Magic Scotch tapes, are cut into long-narrow shape with 3mm width and attached on the surface of the DEA laminates stack (Figure 1b). Different shapes and configurations of stiffeners are able to apply for more complicated deformation.

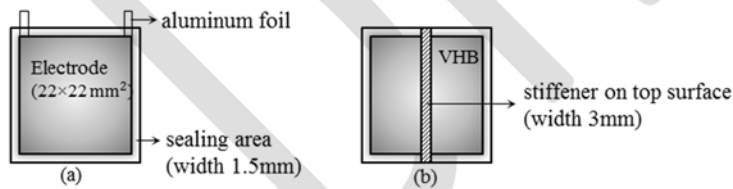


Figure 1. Sketches of DEA samples. (a) Top view of unit-cell DEA structure and its measurement with (b) single strip configuration stiffener in the middle on the top surface.

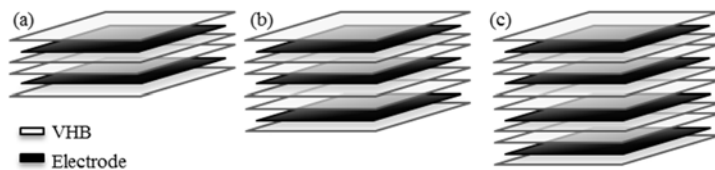


Figure 2. Sketches of DEA samples fabrication with side view of different stack configurations. (a) 1-cell (b) 2-cell (c) 3-cell.

3. Experiment

In the experiments, DEA samples were hung from the electrodes terminal and connected to the high voltage circuit terminal and applied maximum voltages range of 0 – 2.24kV by utilizing a DC-DC voltage converter (Q-80, EMCO Inc.). The converter has a high DC voltage linear amplifier range of 0 – 8kV output for 0 – 5V input. The actuator deformations were captured by high-resolution CCD camera (2448×2048 pixel, Grasshopper, Point Grey Inc.) with an in-situ image system setup for out-of-plane displacement and curvature analysis.

In this section, experimental results of 1, 2, and 3-cell actuators with 1-strip configuration of stiffener are shown below.

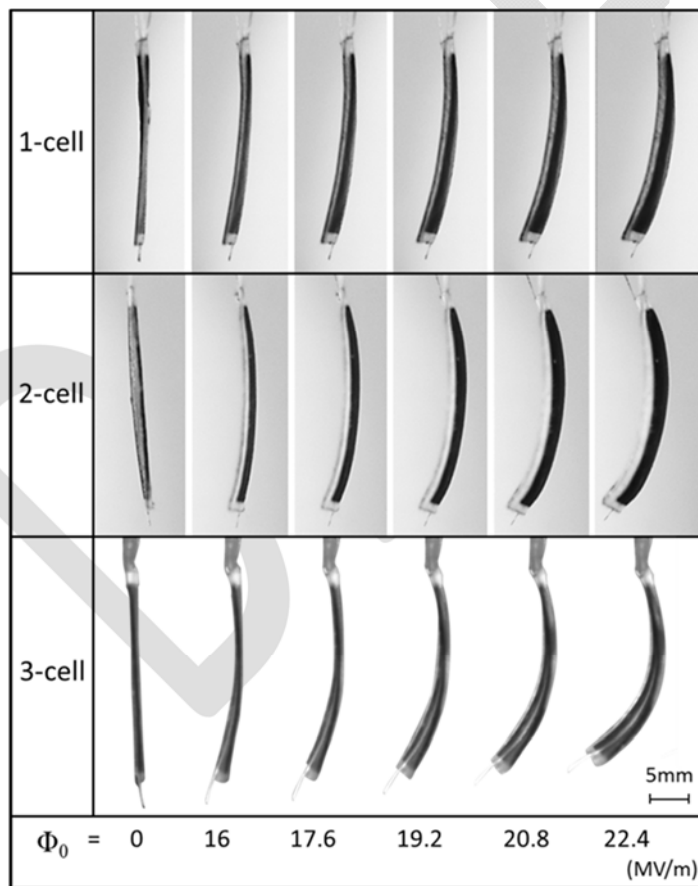


Figure 3 shows the bending deformations of the actuators with the increment of amount of stacking cell from the side view under applied nominal electric field of 0 - 22.4MV/m. When the input nominal electric field is increasing as well as when more cells are laminated, larger bending effects were observed consistently in three different actuators. Planar actuators are fabricated with DEA laminates which contains multi stack of dielectric elastomer actuators. By increasing the number of laminated cells, higher energy is provided that may be able to generate larger deformation.

Curvatures were calculated from the captured images in order to define the deformation of actuators. Partial circles were assumed for every bending motion to ease the measurement and calculation. The results are shown in Figure 6.

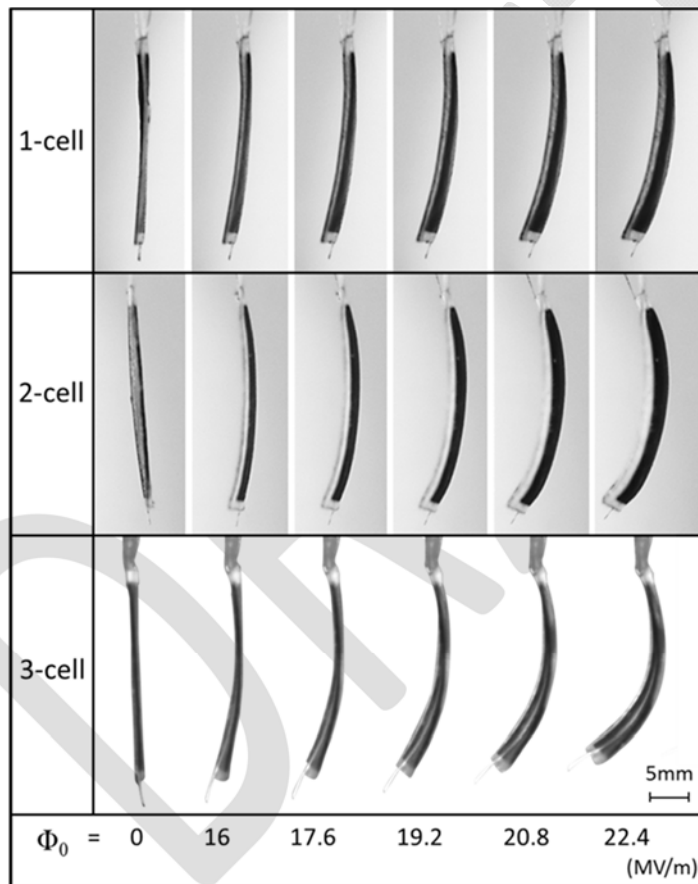


Figure 3. Experimental results of deformation sequence of 1, 2, 3-cell DEA with 1-strip configuration of stiffener attached under applied electric field of 0-22.4MV/m.

In addition, surface deformation analysis is also performed by using digital image correlation technique. The surfaces of planar actuators were patterned with alumina powders. Reference and deformed images were captured before and after actuation. Images were analyzed by using commercial software, Vic2D (Correlated Solutions, Inc.) to obtain and evaluate the in-plane finite strain components. The results of surface deformation analysis will be used to compare with finite element analysis in order to investigate the role of stiffeners.

4. Analytical analysis

To understand the behavior of this actuator design, we utilized the Timoshenko's analysis of bi-metal thermostats [18] and introducing the Maxwell stress instead of the thermal effect to arrive at the general deformation representation under applied electric field. The derivation of the analysis is illustrated as follows.

A free-body diagram of stiffener and EAP bi-layer structure can be simply drawn in Figure 4. When the actuator is activated, total strain of each layer is a summation of strain that caused by electrical, axial, and bending load. It can be written in equation (1) described with material modulus, E and geometry parameters of layer i .

$$\varepsilon_{total} = \varepsilon_{electrical} + \varepsilon_{axial} + \varepsilon_{bending} = \varepsilon_{electrical}|_i + \frac{1}{E_i} \frac{w_i P_i}{a_i w_i} + \frac{M_i}{E_i I_i} \frac{a_i}{2} \quad (1)$$

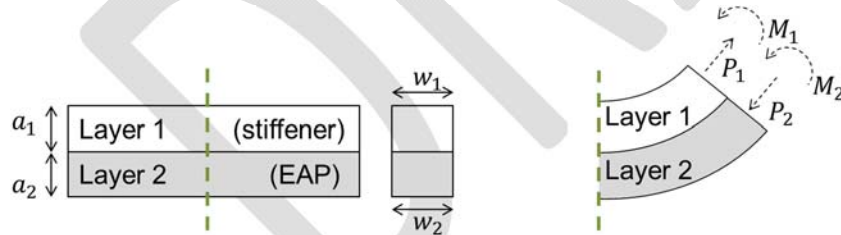


Figure 4. Free-body diagram of stiffener and EAP bi-layer structure represents planar actuator with surface reinforcement. In this figure, a is the thickness, w is the width, M is the bending moment, and P is the axial load.

First of all, to define electrical expansion of EAP, we apply Maxwell stress equations shown in equation (2) and Hooke's Law assuming in-plane deformation is small and within the elastic

deformation zone. Electrical strain is obtained and written as a function of applied nominal electric field in equation (3).

$$\sigma_{zz} = -\frac{1}{2}\epsilon\epsilon_0\Phi_0^2, \quad \sigma_{xx} = \sigma_{yy} = \frac{1}{2}\epsilon\epsilon_0\Phi_0^2 \quad (2)$$

$$\mathcal{E}_{electrical}(\Phi_0) = \mathcal{E}_{xx} = \frac{1}{E} \left[\frac{\epsilon\epsilon_0}{2}\Phi_0^2 - \nu \left(\frac{\epsilon\epsilon_0}{2}\Phi_0^2 - \frac{\epsilon\epsilon_0}{2}\Phi_0^2 \right) \right] = \frac{\epsilon\epsilon_0}{2E}\Phi_0^2 \quad (3)$$

From the definition bending moment in beam theory, $M = \frac{EI}{\rho}$, where ρ is the radius of the bended beam. Apply this into equation (1) and the bending term of strain can be derived and written as in equation (4).

$$\mathcal{E}_{bending} = \frac{1}{\rho} \frac{a_i}{2} \quad (4)$$

Since the axial load $w_1P_1 = w_2P_2 = P$. Besides, the total bending moment can be represented by axial load multiple by half of the total thickness as well as the summation of bending moments on each layer, $P \frac{a_1 + a_2}{2} = M_1 + M_2$. Therefore, axial term of strain can be written as in equation (5).

$$\mathcal{E}_{axial} = \frac{1}{E_i} \frac{1}{a_i w_i} \left(\frac{E_1 I_1}{\rho} + \frac{E_2 I_2}{\rho} \right) \frac{2}{a_1 + a_2} \quad (5)$$

In addition, because of the continuity, total strain at the interface of layer 1 and 2 should be the same. Therefore, the strain condition after actuation can be described by equation (6).

$$\begin{aligned} \mathcal{E}_{electrical}|_1 + \frac{1}{E_1} \frac{1}{a_1 w_1} \left(\frac{E_1 I_1}{\rho} + \frac{E_2 I_2}{\rho} \right) \frac{2}{a_1 + a_2} + \frac{1}{\rho} \frac{a_1}{2} \\ = \mathcal{E}_{electrical}|_2 + \frac{1}{E_2} \frac{1}{a_2 w_2} \left(\frac{E_1 I_1}{\rho} + \frac{E_2 I_2}{\rho} \right) \frac{2}{a_1 + a_2} + \frac{1}{\rho} \frac{a_2}{2} \end{aligned} \quad (6)$$

Let $h = a_1 + a_2$, actuation curvature κ , which is equal to inverse of radius ρ , of this system can be written as a function of material modulus and geometry parameters in equation (7).

$$\kappa = \frac{1}{\rho} = \frac{\frac{\epsilon \epsilon_0}{2E_1} \Phi_0^2}{\frac{2}{h}(E_1 I_1 + E_2 I_2) \left(\frac{1}{E_1 a_1 w_1} + \frac{1}{E_2 a_2 w_2} \right) + \frac{h}{2}} \quad (7)$$

5. Computational simulation

Finite element method is utilized for the computational simulations. User Material subroutine is applied with commercial finite element software ABAQUS. Incompressible Neo-Hookean model is used to represent the elastomer. From literature [19], we know that, elastic energy and electrostatic energy of dielectric elastomer actuator can be written as a function of stretch λ and applied nominal electric field Φ_0 as equation (8) and (9).

$$W_{elastic} = \frac{1}{2} \mu (\lambda_1^2 + \lambda_2^2 + \lambda_1^{-2} \lambda_2^{-2} - 3) \quad (8)$$

$$W_{electrostatic} = \frac{1}{2} \epsilon \epsilon_0 \Phi_0^2 (\lambda_1^{-2} \lambda_2^{-2}) \quad (9)$$

Therefore, the total free energy can be written in equation (10)

$$W(\lambda_1, \lambda_2, \Phi_0) = \frac{1}{2} \mu (\lambda_1^2 + \lambda_2^2 + \lambda_1^{-2} \lambda_2^{-2} - 3) + \frac{1}{2} \epsilon \epsilon_0 \Phi_0^2 (\lambda_1^{-2} \lambda_2^{-2}) \quad (10)$$

Here, nominal electric field is defined as input voltages used in experiments divided by original thickness between electrode layers of unit cell DEA (0.1mm).

As a result, the two required material properties in our finite element simulation are shear modulus and dielectric constant. The dielectric constant of VHB 9460PC tapes is used for 3.21 [20] and the shear modulus is found to be 0.03 MPa from a uniaxial tensile tests we performed shown in Figure 5. Assuming our interest deformation is small and in the elastic behavior region, Young's modulus is calculated to be 0.1 MPa from the strain-stress curve. Shear modulus is calculated and obtained to be 0.03 MPa by applying Hooke's Law where 0.5 for Poisson's ratio is employed assuming incompressible material.

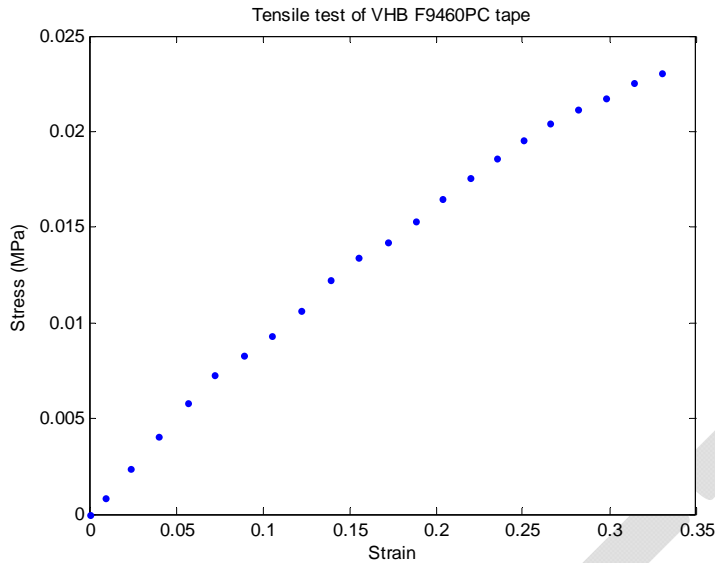


Figure 5. Stain-stress curve of VHB F9460PC tapes from uniaxial tensile test.

In the computational simulation, 3D geometric half model for cantilever laminate was used for overall structure. Thickness of electrode layers is neglected. For multiple-cell actuator cases, all active layers were combined into one single layer. A Hybrid 20-node quadratic brick element employed for each individual layer linked with surface-based tie constraint. One edge of the sample was anchored and other edges were left free-to-move. Curvatures are used to represent actuator deformation in simulation. They were assumed as partial circles and calculated by using the center in-plane and out-of-plane displacement. Figure 6 shows the comparison of computational and experimental results.

From finite element analysis, the profile of in-plane strain field is obtained to compare with experimental observation from surface displacement analysis. Results from both analyses (Figure 7) show a band of region that much higher strain occurs. The high strain region represent lateral strain perpendicular to the stiffener direction concentrates near the boundary of stiffeners. The concentrated strain is caused by stiffener constraints to the elastomer expansion. This shows the nonlinearity of in-plan deformation of this type of actuator which will affect on our analytical analysis. More detail will be discussed in the next section.

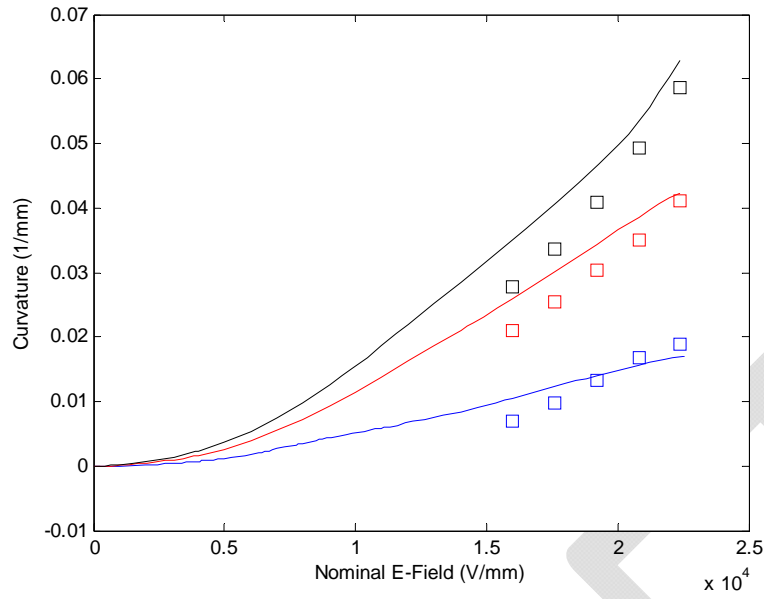


Figure 6. Curvature comparison of experimental and computational results of 1, 2, 3-cell actuators with 1-strip configuration. Solid lines represent FEM results and square marks represent experimental results.

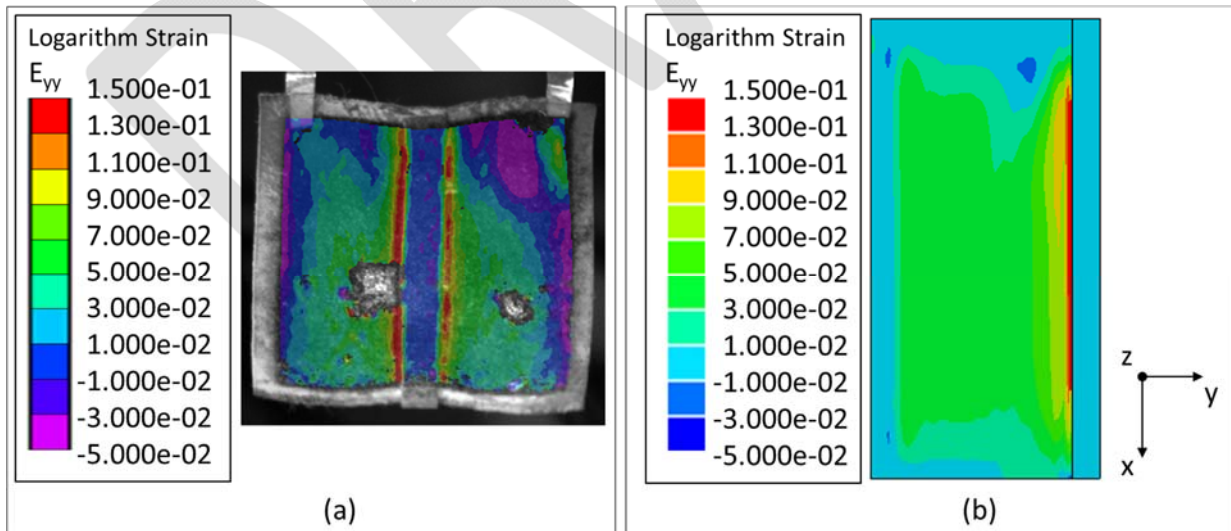


Figure 7. Surface displacement analysis (a) and finite element (b) results of concentrated strain around stiffener under applied nominal electric field of 20800 V/m.

6. Discussion

For this special design, two cover layers are attached and their effects to the electrical strain have to be considered. Therefore, a parameter β is required in the developed analytical solution to represent how the additional symmetric cover layers influence the in-plane expansion. β is defined as the thickness of active layers divided by the total thickness of actuators. For example, for case of 1, 2, and 3-cell actuators, β is 1/2, 2/3, and 3/4 respectively.

Comparing our analytical solution with experimental data, a fitting parameter in the analytical solution is found in order to represent all of the nonlinearities including inhomogeneous deformation and nonlinear electromechanical coupling effect. In this case, the fitting parameter is determined to be 0.55. Finally, the analytical solution can be written in equation (11). Actuation curvaures are represented as a function of input nominal electric field.

$$\kappa(\Phi_0) = \frac{1}{\rho} = \frac{0.55\beta \frac{\epsilon\epsilon_0}{2E_1} \Phi_0^2}{\frac{2}{h}(E_1I_1 + E_2I_2) \left(\frac{1}{E_1a_1w_1} + \frac{1}{E_2a_2w_2} \right) + \frac{h}{2}} \quad (11)$$

Using this developed analytical solution, the deformation sequences under serial applied electric field from experiments are compared and plotted in Figure 8.

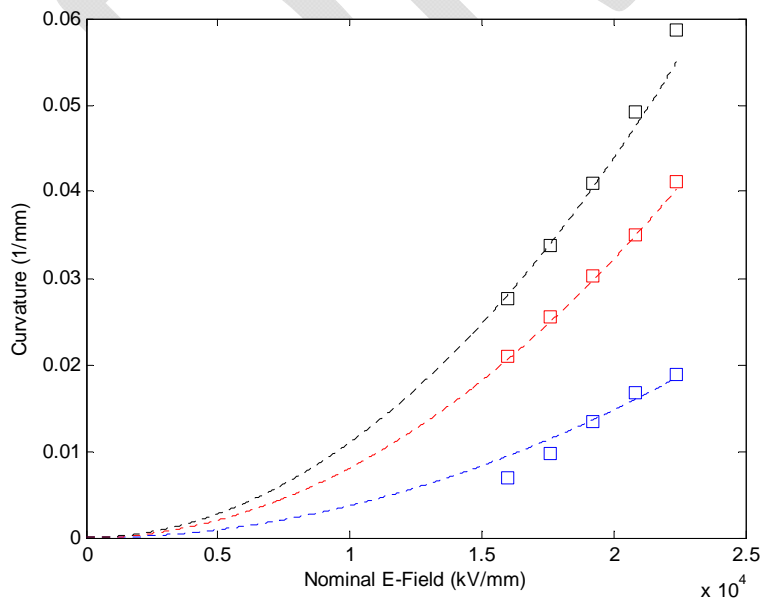


Figure 8. Curvatures from deformation sequences versus applied electric field where the dotted lines are analytical solutions and square marks are experimental results. The color blue, red, and black represent 1, 2, and 3 cell actuators respectively.

Force-stroke characteristic of can be obtained from finite element analysis. In the computational simulation, we first constrain the out-of-plane displacement of the far-end edge opposite to the anchored edge and then applied electric field on the actuators to certain level. After the electric field reaches certain level, the edge constraint is removed and replace with uniform out-of-plane displacement applying on tide-up edge. Reaction forces on every node along the edge are recorded and summed up in every interested displacement step. The results of the force-stroke characteristic of a 3-cell actuator stiffener surface reinforcement under different applied nominal electric fields are shown in Figure 9.

In Figure 9, the solid lines show the force-stroke characteristics of a 3-cell-1-stiffener actuator are controlled by applied electric field. With increasing applied electric field to higher level, larger reaction force is observed at zero displacement and larger displacement is observed at zero reaction force. However, for a free-to-move actuator, nodes at edge are not tied up. This leads to deviation of reaction force calculated from the summation of each node and the experimental data converted from actuation curvatures which are represented in solid circles in the plot.

Figure 9. Force-stroke characteristics of a 3-cell-1-stiffener actuator under applied electric field of 17600 (green), 19200 (red), and 20800 V/mm (blue).

7. Conclusion

In this paper, we shared an idea of freestanding planar actuators based on dielectric elastomers capable of out-of-plane deformation by using partial stiffener reinforcement on the surfaces. With our concept, no additional devices to support prestretch are required. Deformation of the actuator can be designed is by using different configurations of surface stiffener reinforcements. Experiments provided the actuators performances. In addition, surface displacement analyses were employed in order to assist understanding how stiffeners induce deformation to planar actuators. An effective band around stiffener constraints was discovered which leads to inhomogeneous deformation in this case. The analytical analysis was provided for future control strategies. Finite element framework was also developed which could be used to investigate the role of stiffeners and force-stroke characteristics of actuators. It could also be employed to study more complex 3D motion based on this actuator design in our future works.

References

- [1] Y. Bar-Cohen, *Electroactive Polymer (EAP) Actuators as Artificial Muscle: : Reality, Potential, and Challenges*nd edition, Bellingham, WA: SPIE, 2004.
- [2] J.D.W. Madden, N.A. Vandesteeg, P.A. Anquetil, P.G.A. Madden, A. Takshi, R.Z. Pytel, S.R. Lafontaine, P.A. Wieringa, and I.W. Hunter, "Artificial muscle technology: physical principles and naval prospects," *IEEE J. Ocean. Eng.*, vol. 29, no. 3, pp. 706-728, (2004).
- [3] K. J. Kim, and S. Tadokoro, *Electroactive Polymers for Robotic Applications: Artificial Muscles and Sensors*, London, UK: Springer, (2007).
- [4] S. Ashley, "Artificial muscles," *Scientific American*, p. 52–59, October (2003).
- [5] R. Pelrine, R. Kornbluh, J. Joseph, R. Heydt, "High-field deformation of elastomeric dielectrics for actuators," *Materials Science & Engineering C*, vol. 11, no. 2, p. 89–100, (2000).
- [6] W. C. Roentgen, "About the Changes in Shape and Volume of Dielectrics Caused by Electricity," *Annual Physics and Chemistry Series*, Vols. 11, Section III, (1880).
- [7] A. Wingert, Matthew D. Lichter, and Steven Dubowsky, Fellow IEEE. "On the Design of Large Degree-of-Freedom Digital Mechatronic Devices Based on Bistable Dielectric Elastomer Actuators," *IEEE/ASME transactions on mechatronics*, Aug. 2006: vol. 11, no. 4.
- [8] P. Lochmatter, G. Kovacs, P. Ermanni. "Design and Characterization of shell-like actuators based on soft dielectric electriactive polymers," *Smart Materials and Structures*, 2007: Vol. 16, 1415-1422.
- [9] G. Kofod, M. Paajanen, S. Bauer, "Self-organized minimum-energy structures for dielectric elastomer actuators," *Appl Phys A* 85, 141-143, (2006).
- [10] M. T. Petralia and R. J. Wood, "Fabrication and analysis of dielectric-elastomer minimum-energy structures for highly-deformable soft robotic systems," *Intelligent Robots and Systems (IROS)*, 2010 IEEE/RSJ International Conference on , pp. 2357 - 2363 , (2010).
- [11] R. Kornbluh, R. Pelrine, and Q. Pei, "Dielectric elastomer produces strain of 380%," *EAP Newsletter*, 2(2), p. 10–11, (2002).
- [12] X. Zhao, Z. Suo, "Theory of dielectric elastomers capable of giant deformation of actuation," *Physical Review Letters*, 104, 178302, 2010.
- [13] Kornbluh R, Perine R, Pei Q, Heydt R, Stanford S, Oh S and Eckerle J. "Electroelastomer: application of dielectric elastomer transducers for actuation, generation and smart structures." *Proc. SPIE Int. Soc. Opt. Eng.* 4698, 2002: 254–70.
- [14] Q. Pei, M. Rosentha, S. Stanford, H. Prahlaad, and R. Pelrine "Multiple-degrees-of-freedom electroelastomer roll actuators." *Smart Mater. Struct.*, 2004: 13 N86–92.
- [15] P. Sommer-Larsen, G. Kofod, M.H. Shridhar, M. Benslimane, and P. Gravesen, "Performance of dielectric elastomer actuators and materials," *Proc. SPIE Int. Soc. Opt. Eng.* 4695 158–66, 2002.
- [16] W. Lai, "Characteristics of Dielectric Elastomers and Fabrication of Dielectric Elastomer Actuators for Artificial Muscle Applications", M.S. thesis," Dept. Aer. Eng., Iowa State University, Ames, IA, USA, 2011.

- [17] T. Lu, J. Huang, C. Jordi, G. Kovacs, R. Huang, D. R. Clarke, and Z. Suo, " Dielectric elastomer actuators under equal-biaxial forces, uniaxial forces, and uniaxial constraint of stiff fibers," *Soft Matter*, 2012, 8, 6167-6173
- [18] S. Timoshenko, "Analysis of Bi-Metal Thermostats," *Journal of the Optical Society of America*, vol. 11, pp. 233–255, 1925.
- [19] X. Zhao, W. Hong and Z. Suo, Electromechanical coexistent states and hysteresis in dielectric elastomers, *Phys. Rev. B*, 76,134113 (2007).
- [20] M. Aschwanden, R. Friedlos, and A. Stemmer, "Polymeric, Electrically Tunable Optical Elements based on Artificial Muscles," *Lasers and Electro-Optics Society (LEOS), The 20th Annual Meeting of the IEEE*, 2007.



ISU-MECH-00

Control of force-stroke characteristics of planar dielectric elastomer actuator

William Lai¹, Ashraf Bastawros¹, Wei Hong¹ and Soon Jo Chung²

1. Department of Aerospace Engineering, Iowa State University
2. Department of Aerospace Engineering, University of Illinois, Urbana Champaign

October, 2013

Manuscript for possible submission to Soft Matter

Introduction

Dielectric elastomers (DEs) are a type of electroactive polymers that has been studied for many years in the booming field of biomimicry devices development. The high strain, comparably short response time, low cost, and high electromechanical coupling efficiency [1] make them a strong candidate of material selection as artificial muscles. They are often used to fabricate actuators, so called dielectric elastomer actuators (DEAs). DEAs are made of soft dielectric elastomer membranes sandwiched by compliant electrode layers to form dynamic capacitors. The columbic force generates Maxwell stress [2] when electric field is applied across the thickness direction. Maxwell stress attracts both electrode layers together and compress the middle incompressible elastomer which will introduce the in-plane expansion of DEAs.

The idea of fabricate planar actuators based on dielectric elastomer has been discussed in electroactive polymer society for years [3]. Due to the mechanism of dielectric elastomer actuators, motion of in-plane expansion is very direct and easy to achieve. However, in order to broaden the application possibilities and categories, it is important to study structures that can induce 3-dimensional motion. Several different designs were presented in the literatures.

Since it has been shown that prestretch is a method capable of greatly improving in-plane actuation strain of dielectric elastomer actuators [4], a branch of planar dielectric elastomer actuators design is based on prestretched membrane. P Lochmatter and G Kovacs demonstrated an idea of shell-like actuators [5, 6] using two parallel prestretched dielectric elastomer actuators connected by hinge structures. When the actuator on one side of the shell is activated, shell is capable of bending. The core structure of hinge can also be constructed in different ways, such as an array of spheres. This may help the shell-like actuator present biaxial deformations for more complicated motion. In their later studies [7], the actuator can be further improved by several adjustments, for example, multi layers dielectric elastomers and reinforced carbon rods which support the prestretch. Thanks to the prestretch, these bending devices showed results of large out-of-plane deformation and, more impressively, outstanding blocking force from the bending motions. Besides, because of the prestretch, higher input electric field can be applied and, as a result, actuators demonstrate even better bending characteristics. However, the additional supports also cause unwanted setbacks that conflicts the goal of developing light weight and flexible actuators when employing electroactive polymers at the first place. For example, support structures for prestretch occupy much more weight and space than elastomer itself [8] and limited the degree-of-freedom of deformations by the supporting and connecting structures. This branch of design is featuring high value performances of deformation with a trade-off of losing flexibility and energy-to-mass/space ratio by using additional rigid prestretch-support frames.

Another approach to induce out-of-plane deformation from planar actuators is named dielectric elastomer minimum energy system (DEMES). The idea was first presented by G Kofod et al. [9]

which demonstrated a clever strategy reversibly utilizing prestretch. Dielectric elastomers are prestretched and attached on supporting structures which are inextensible but pliant. Usually thin membranes of plastic slides or papers are employed. Without additional energy input, the elastic energy used to prestretch DE films will transfer to the outer frame and causes the entire system to buckle. Once electric field is applied to the system, the expansion of elastomer will flatten the system and reverse the buckling. The system motions are defined by the frame structure. Different configurations of frames may induce different shapes of buckling. Due to the usage of prestretch, deformation and output blocking force of the system is comparably large []. G Kofod et al. [] showed an application of gripping actuator in their study demonstrated the significant force that this system may provide. Besides, the pliant frames give the system higher flexibility comparing to rigid frames and extend broader application. Despite the beauty features of DEMES, a disadvantage appears in deformation shape prediction with difficulty and inaccuracy. M T Petralia and R J Wood presented a structure for highly-deformable soft robotic system based on this strategy. In the pictures from their study, we can observe noticeable differences of deformation even with the same support-frame shape.

Other than the above designs, another approach is the unimorph DEAs. In the early study of dielectric elastomer actuators [], a simple idea to provide unimorph bending effect by attaching extendable DE with stiff substrate was proposed. In 2011, O A Araromi et al. [] [] introduced a comprehensive study cover from an unique spray-deposited fabrication to actuators characterization. In this their design, multiple layers of DE film were spray deposited on a substrate membrane with compliant electrode in between each layer and no employment of prestretch. The stiffer substrate constrained one side of the planar actuator expansion and induced overall bending. This bending device showed considerable deflection but less blocking force. Nevertheless, without the requirement of prestretch supporting frames, the actuator is lighter and more flexible and still performing noticeable deformation.

To not only keep the existed advantages of unimorph DEAs such as light weight and large deflection but also further improve the flexibility of actuator motions, we introduced a strategy to fabricate planar dielectric elastomer actuators capable of out-of-plane deformation with no requirement of prestretch []. Instead of applying fully covered stiffer substrate to urge bending, partially reinforcement of stiffener segments were used in our design. Small segments of stiffener reinforcement are able to provide even more complicated 3-dimensional deformation to a planar actuator and at the meantime, featuring light weight and high energy-to-mass ratio. In this study, we will provide deeper understanding of the role of stiffeners and their interactions with dielectric elastomers. By varying stiffener configurations, we are able to change the characteristics of actuators, such as deflection and reaction force, while keeping bending stiffness the same. This enlarges the complexity of surface motion to design planar actuators.

Fabrication and Experiment

To study the role of stiffener, we planned to fix the geometry parameter of bending stiffness and vary periodicity of stiffeners. Two cases were compared: (a) single stiffener and (b) split stiffener while maintaining the total width. Following the detail of fabrication procedure in our previous work [], two 3-cell planar actuators were fabricated. A 3-cell planar actuator is composed by stacking three unit cells of actuator. Each unit cell includes two layers of VHB 9460PC tape (50 μ m thick each) in the middle and sandwiched by compliant electrode layers where carbon black particles (Super C65, TIMCAL Inc., USA) were employed. Two additional VHB tapes were used to cover up the stacked actuator for protection that makes a total thickness of 0.4mm for a 3-cell planar actuator (thickness of electrode layers were neglected). One of the planar actuators was attached with one 3mm-wide stiffener (3M Magic scotch tapes) on the surface and the other actuator was attached with three 1mm-wide stiffeners equally separated as shown in Figure 1b and 1c. Both actuators were connected to the high voltage circuit with applied voltages range of 0 – 2.24kV by employing a DC-DC voltage converter (Q-80, EMCO Inc.). High-resolution CCD camera (2448 \times 2048 pixel, Grasshopper, Point Grey Inc.) with an in-situ image system setup was utilized to capture the side view of actuator deformations. The deformation sequence of 3-cell DEA with stiffener configuration of 1 and 3 segments under applied nominal electric field, Φ_0 , of 0-22.4kV/mm is shown in Figure 2. Besides, actuation curvatures were measured from the captured images and shown in square marks in Figure 3.

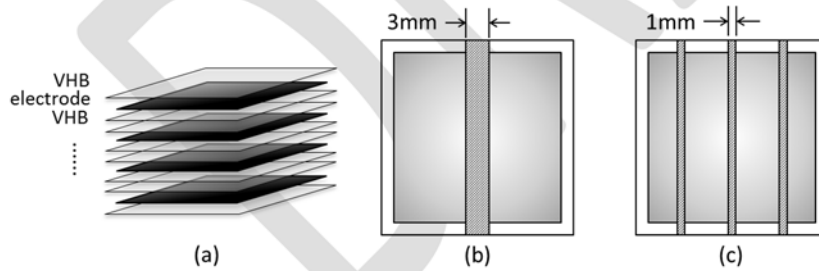


Figure 1. Schematic diagram of (a) side view of 3-cell planar actuator and two DEA samples with (b) single stiffener and (c) triple split stiffeners attached.

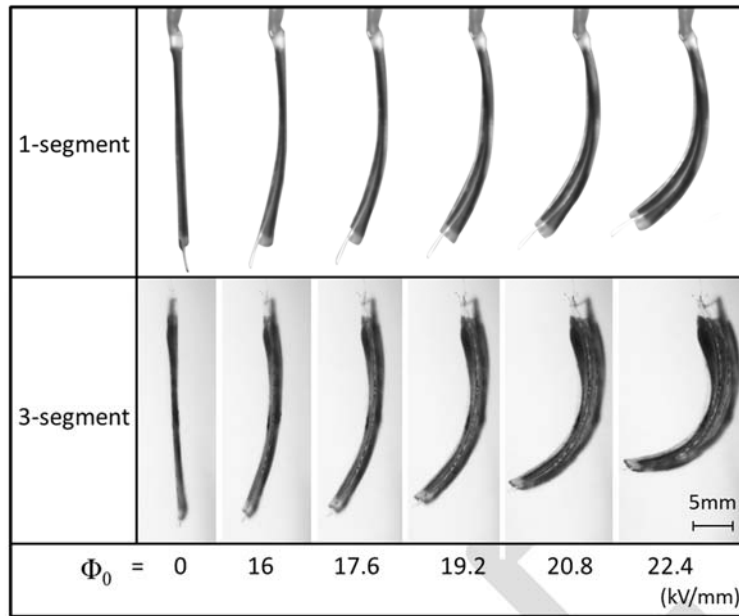


Figure 2. Experimental results of deformation sequence of 3-cell DEA with stiffener configuration of 1 and 3 segments attached under applied electric field of 0-22.4MV/m.

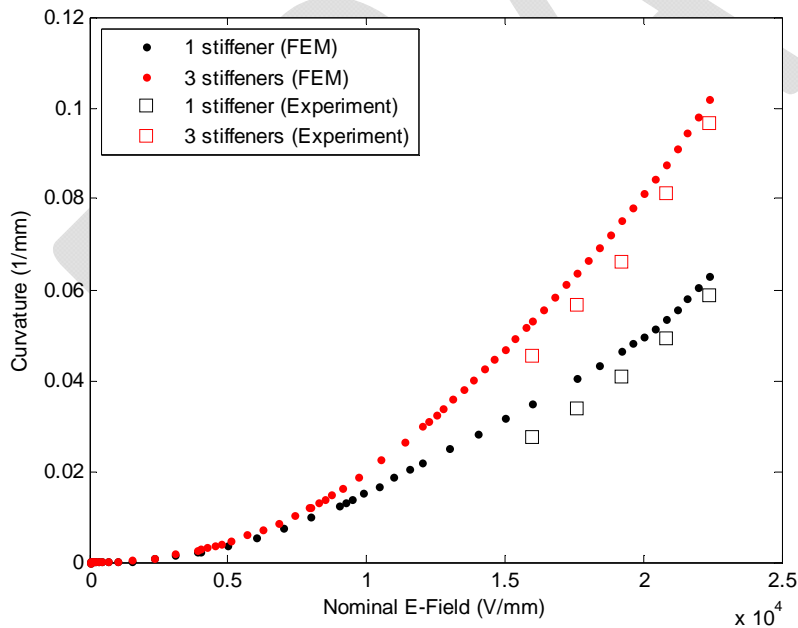


Figure 3. Actuation curvatures under applied electric field of 0-22.4kV/mm of 1 (black) and 3 (red) segments of stiffeners attached on a 3-cell DEA. Square marks and dotted lines represent results from experiments and finite element analysis respectively.

Computational simulation

Utilizing the framework we developed that simulates the coupling electromechanical behavior of dielectric elastomer actuators [], we performed in computational works of both single and splitting stiffeners cases. In the simulation, overall structure was based on half model of 3D geometric cantilever laminate. All active layers were combined into one single layer and, in the meantime, thickness of electrode layers was neglected. A Hybrid 20-node quadratic brick element was employed for each individual layer linked with surface-based tie constraint. One edge of the sample was anchored and other edges were left free-to-move. Curvatures were used to represent actuation motion. Curvatures were assumed as partial circles and calculated based on the in-plane and out-of-plane displacements of the central point at the end free edge. The deformation results of both single and three stiffeners cases of actuator are shown in Figure 3 with respect of serial input nominal electric field up to 22.4 kV/mm. The side view of deformation sequence in simulation is shown in Figure 4. Strain field of the actuators after electric force stimulated can also be obtained and shown in Figure 5.

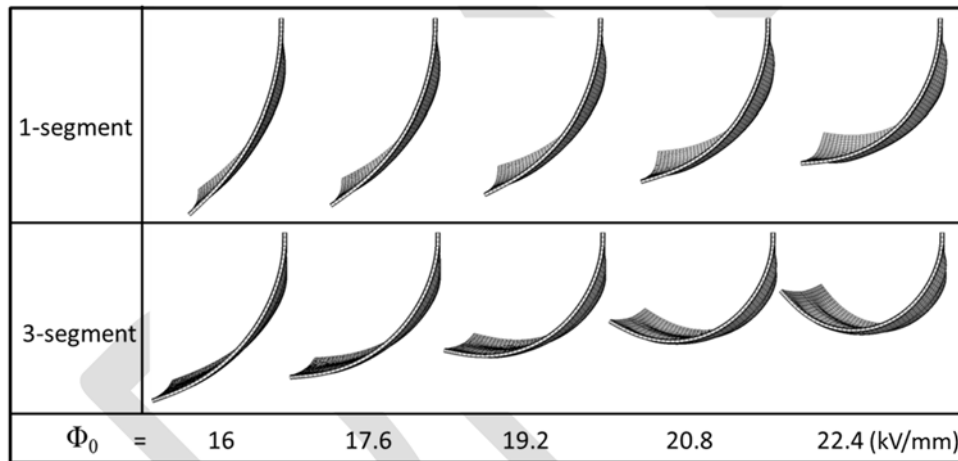


Figure 4. Deformation sequence in finite element simulation of 3-cell planar actuator with 1 and 3 segments of stiffeners under nominal electric field of 0-22.4 kV/mm.

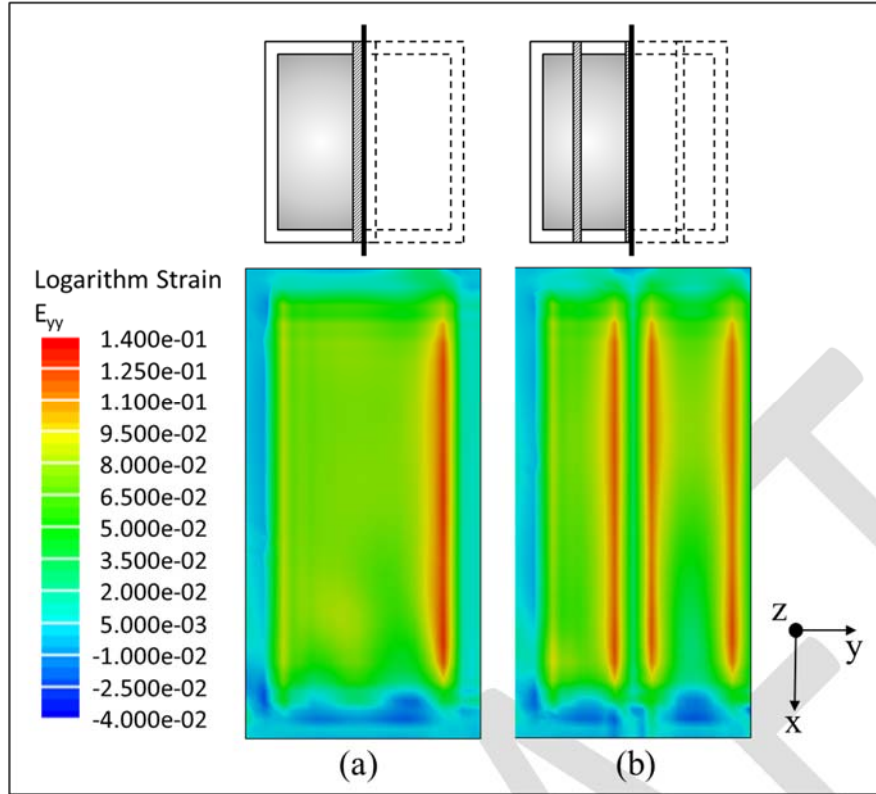


Figure 5. Strain field of 3-cell planar actuator with 1 segment (a) and 3 segments (b) of stiffener under nominal electric field of 22.4 kV/mm.

Discussion

From the experiments, we observed that the actuation curvatures are controlled by the configuration of attached stiffeners. In the two cases we experimentally performed, the total bending stiffness was controlled to be the same by maintaining the total width of stiffeners. However, different characteristics were revealed in two actuators. With increasing precocity of stiffeners, larger curvatures can be achieved. To investigate this phenomenon, we go through finite element simulation from several aspects. First of all, if we look at the general deformation shapes shown in Figure 6, bending is not uniformly. Buckling occurred between the stiffener edges and the end-edge of actuator. For a bending device, this kind of buckling is not what we appreciate. It wastes energy on unwanted direction (y-axis) deformation. As a matter of fact, increasing precocity of stiffener is able to limit the unwanted deformation. And doing by this, actuation closer to homogeneous bending will be observed. And because of deformation occurs on the bending direction (x-axis) instead, larger bending curvature can be achieved.

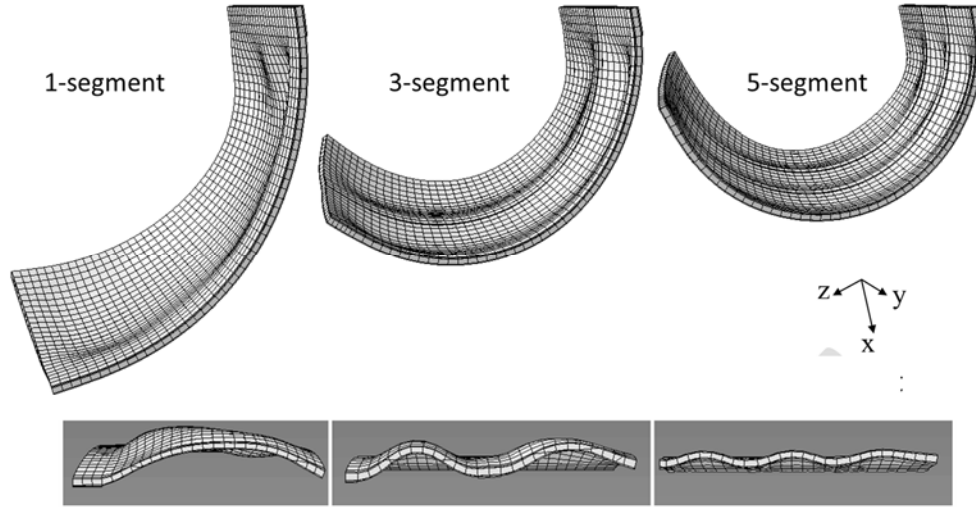


Figure 6. Side view and cross-sectional view of half sample of 3-cell actuator attached with 1, 3, and 5 segments of stiffeners in finite element simulation under applied nominal electric field of 22400 V/mm.

Secondly, strain field from finite element simulation shown in Figure 5 noted strain concentration around the stiffener/elastomer junctions. That is to say, in-plane expansion is not homogenous and has localization related to the location of stiffeners. Each stiffener contributes the extra region in addition to its own width. Therefore, multiple stiffeners are able to contribute more localization and constrain larger region of in plane deformation. This gives us higher value of effective width that is actually inducing bending leads to larger actuation curvatures.

Reviewing analytical analysis in our previous work [] based on the theory of bi-material thermostats, axial strain is one of the main driving factor that urge bending and was assumed to be uniform. Equation we used to represent actuation curvatures κ as a function of input nominal electric field Φ_0 was written as equation (1) where $\epsilon\epsilon_0$ is dielectric constant of the elastomer multiplies vacuum permittivity; E , I , and a are Young's modulus, moment of inertia, and the layer thickness; subscripts 1 and 2 represent layer stiffener and layer dielectric elastomer respectively. h is the total thickness and β is a geometry factor that varies with the amount of laminated cells due to the actuator design where in this 3-cell case, $\beta = \frac{3}{4}$.

$$\kappa(\Phi_0) = \frac{1}{\rho} = \frac{0.55\beta \frac{\epsilon\epsilon_0}{2E_1} \Phi_0^2}{\frac{2}{h}(E_1I_1 + E_2I_2) \left(\frac{1}{E_1a_1w_1} + \frac{1}{E_2a_2w_2} \right) + \frac{h}{2}} \quad (1)$$

However, stiffeners in our design are not fully covering the entire surface and, as a result, only approving an effective region of constraint. A schematic diagram in Figure 7 illustrates the idea of partial axial deformation caused by single stiffener within an effective width. The effective width should be used to modify our analytical analysis. Furthermore, the additional fitting parameter, 0.55, we is found to be caused by this modification. The modified analytical solution is shown in equation (2) where effective width w_{eff} varies with different cases of stiffener configuration.

$$\kappa(\Phi_0) = \frac{1}{\rho} = \frac{\beta \frac{\epsilon \epsilon_0}{2E_1} \Phi_0^2}{\frac{2}{h}(E_1 I_1 + E_2 I_2) \left(\frac{1}{E_1 a_1 w_1} + \frac{1}{E_2 a_2 w_{eff}} \right) + \frac{h}{2}} \quad (2)$$

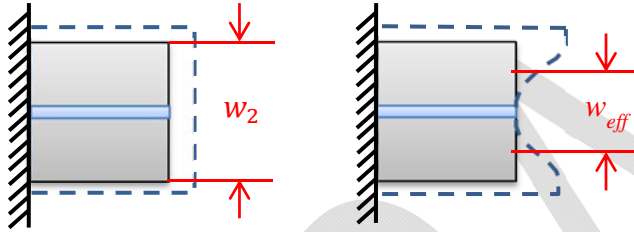


Figure 7. Schematic diagram of narrow strip stiffener constrains only part of the axial expansion of EAP. (a) In ideal case of analytical solution, uniform in-plane expansion of EAP is expected. Total EAP width, w_2 are affected by stiffener. (b) In real case, only partially constraint is caused by narrow stiffener reinforcement and w_{eff} is required to replace w_2 .

Fitting analytical solution with experiential results, effective widths of single and three stiffeners were figured to be 11mm and 21mm respectively. The effective width can be found through finite element simulation or, for this case, $w_{eff} = w_{stiffener} + w_{sealing\ region} + (2n)w_{localization}$, where $w_{stiffener}$ is the total width of stiffeners, $w_{sealing\ region}$ is the sealing region from the actuator design which is 3mm total, n is the number of stiffeners, and $w_{localization}$ is the local constraint width caused by each stiffener, in this case equal to 2.5mm. Results are shown in Figure 8.

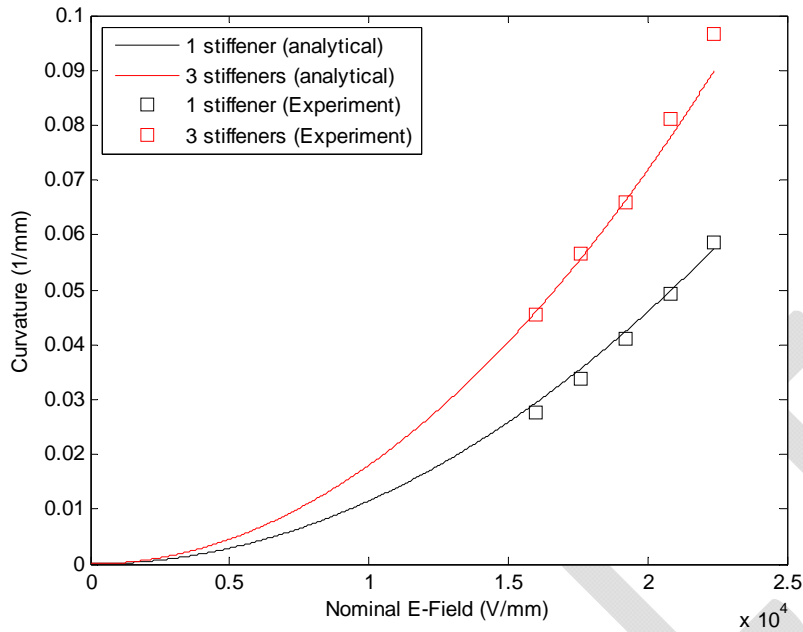


Figure 8. Fitting actuation curvatures from analytical analysis with experimental results. Actuation curvatures shows deformation under applied nominal electric field of 0-22.4kV/mm of 1 (black) and 3 (red) segments of stiffeners. Square marks and solid lines represent experiments and finite element analysis respectively.

Theoretically, effective width can be increased unlimitedly; however, after certain amount of stiffeners, the localization effective region caused by each stiffener may become overlapped. The total effective width is going to be saturated with limited actuation presentation. We simulated the effect of increasing the numbers of split stiffeners from one to five in finite element model as shown in Figure 9Figure 5. The increases of actuation curvatures become smaller each time we split the stiffener into narrower segments. It saturated at four segments under maximum applied electric field of 22400 V/mm.

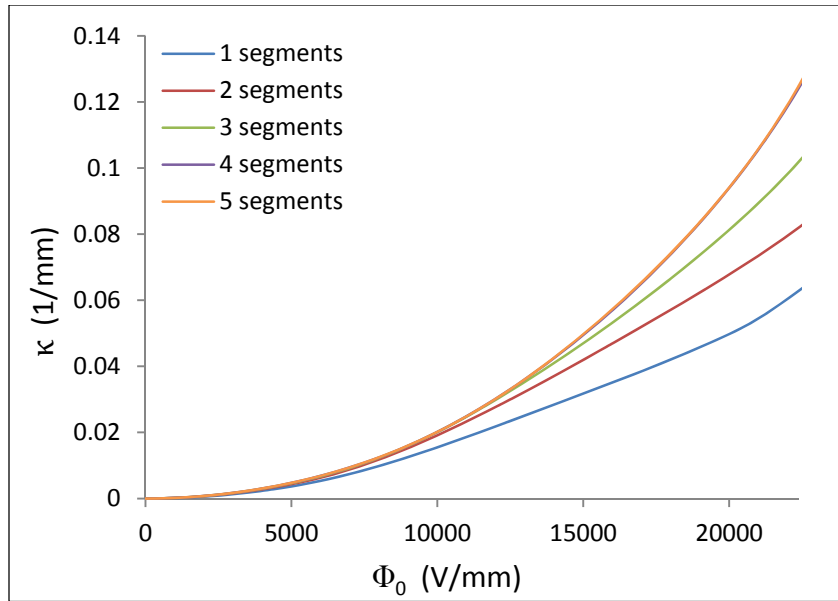


Figure 9. Finite element results of actuation curvature versus applied nominal electric field of 3-cell planar actuator with different numbers of split stiffeners from one to five.

In addition, total elastic energy was obtained from finite element analysis (Figure 10). The results show that the energy can be considered as no change with different numbers of stiffener we use. The energy doesn't increase with higher actuation curvatures. This tells us only the efficacy of energy is changing. Actuation strain is more properly used in the bending direction in multiple-stiffener case and leading to higher bending curvatures.

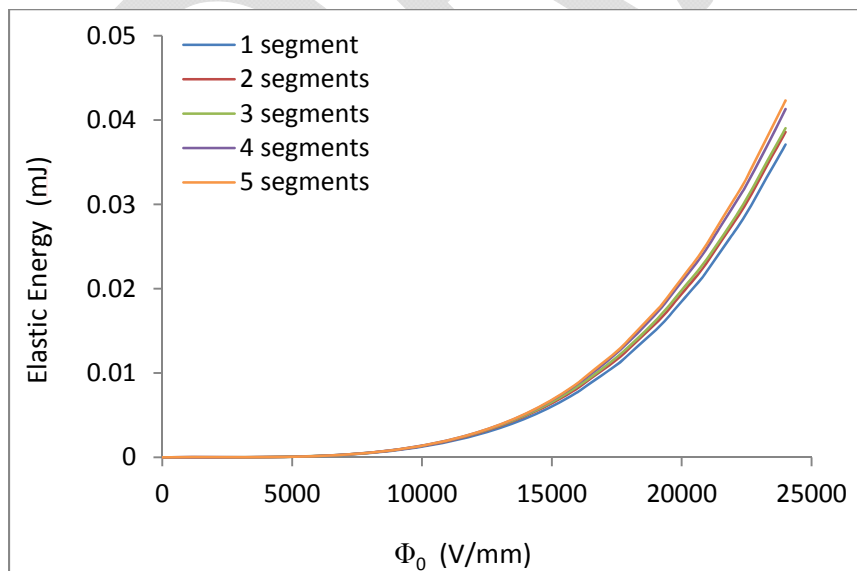


Figure 10. Finite element results of total elastic energy versus applied nominal electric field of 3-cell planar actuator with different numbers of split stiffeners from one to five.

Finally, force-stroke characteristics can also be obtained from finite element simulation. Take applying electric field of 20800 V/mm as an example which shown in Figure 11, the increases of stiffener periodicity can be used to adjust different force-stroke characteristics. More stiffeners yield higher blocking force as well as larger deflection of this bending device.

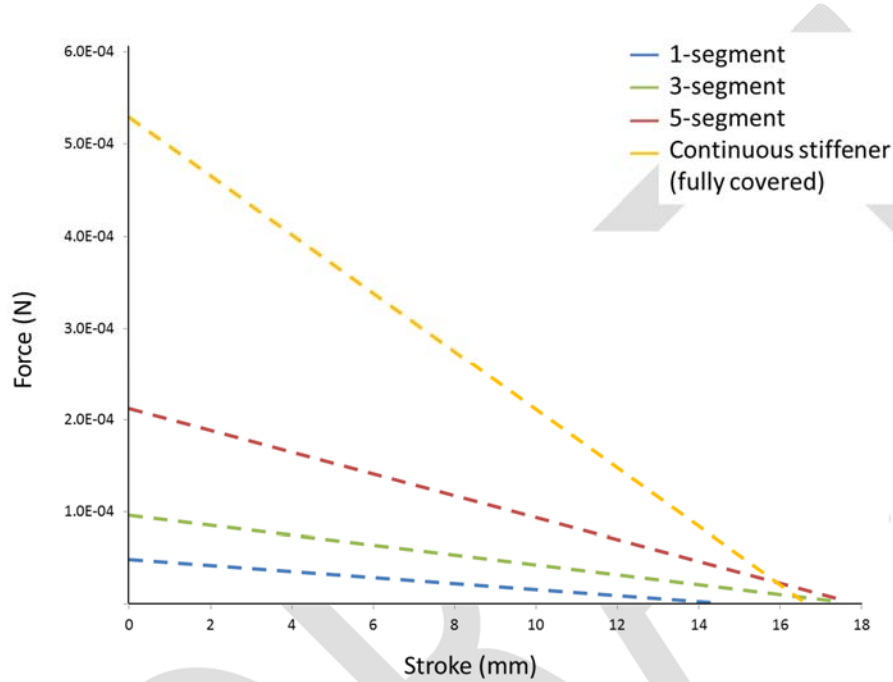


Figure 11. Force-stroke characteristics of 3-cell actuator attached with 1, 3, and 5 segments of stiffeners in Finite element simulation under applied electric field of 20800 V/mm comparing with the case of fully covered continuous stiffener.

Conclusion

In this paper, we investigate the role of stiffener in our planar actuator design. Stiffeners bring the ability out-of-plane deformation to planar dielectric elastomer actuators. Each small segment constrains a localized in plane expansion of elastomer and causes axial stain that leads the actuator to bend. Experimental and finite element simulation results are provided to investigate how changing stiffener configuration while keeping the bending stiffness may influence actuation curvatures. Moreover, force-stroke characteristics can be adjusted by varying stiffener periodicity as well. Modified analytical analysis is also provided to describe the effect of stiffener reinforcement.